
Analysis on the Lepton Flavor Violating Decay $\tau \rightarrow \mu \pi^0$ in Belle II

Analyse des Lepton Flavor verletzenden Zerfalls
 $\tau \rightarrow \mu \pi^0$ in Belle II

Masterarbeit aus der Physik

vorgelegt von

Márton Németh-Csóka

November 27, 2021

Fakultät für Physik

Ludwig-Maximilians-Universität München



Betreuer: Prof. Dr. Christian Kiesling

Abstract

During its runtime from 1999 to 2010 the Belle experiment was able to confirm the Kobayashi-Maskawa theory about the occurrence of \mathcal{CP} violation and by this played a decisive role in firmly establishing the Standard Model (SM). However, there is also convincing evidence for physics beyond the SM. The asymmetric electron-positron collider KEKB was running at the energies around the mass of the $\Upsilon(4S)$ -resonance and was together with the BaBar experiment's PEP-II accelerator at SLAC leading in defining the boundaries for non-SM theories. Many of their upper limits are still without competition from other experiments.

Belle's upgraded successor Belle II aims for a higher precision and an up to 30 times higher instantaneous luminosity of $\mathcal{L} = 6 \cdot 10^{35} \text{ cm}^{-2} \text{ s}^{-1}$ and took its first data in 2019. The goal of Belle II is to collect 50 times more data than Belle, a total integrated luminosity of $L_{\text{int}} = 50 \text{ ab}^{-1}$. The massive increase in luminosity together with new and improved parts and upgrades of the detector create an excellent environment to conduct precision measurements and reopen the path for searches beyond the SM.

This work focuses is on the lepton flavor violating decay $\tau \rightarrow \mu\pi^0$ with the goal to explore the prospects of finding New Physics in this particular channel. Belle and BaBar found the upper limit for the branching ratio of this decay to be $\Gamma(\tau \rightarrow \mu\pi^0)/\Gamma_{\text{tot}} < 2.7 \cdot 10^{-8}$ while having an available luminosity of $L_{\text{int}} = 901 \text{ fb}^{-1}$.

In the analysis, the decay simulated by a Monte Carlo software including detectors and full reconstruction to get an understanding of the overall kinematics. The signal is reconstructed directly by combining possible pairs of μ and π^0 , where the π^0 is reconstructed from two photons. Based solely on kinematics the detector is able to reconstruct 64% of the simulated signal. When studying the background, the largest background is that of the pair production of muons, together with light quarks and τ that decay according to the predictions of the SM. After applying kinematic cuts and requiring a moderate confidence threshold for the identification of the muon, only 5.3% of the signal is left, but the background is fully suppressed in a sample equaling 100 fb^{-1} . Belle claimed a signal sensitivity of 4.2% with a background prediction of 0.64 events, BaBar claimed 4.8% and predicted 1.33 events, the former with a recorded luminosity nine times larger, and the latter four times larger than this sample. This suggests, that Belle II with its anticipated 50 ab^{-1} luminosity will be able to completely dominate the other two experiments. To further confirm this, the next step would be to conduct studies with larger MC datasets, before moving on to actual data, which may comprise more than $L_{\text{int}} = 500 \text{ fb}^{-1}$ by the end of 2022.

Table of Contents

1	Introduction	7
2	Physics Overview	9
2.1	The Standard Model of Particle Physics	9
2.1.1	Conservation Laws and Quantum Numbers in the Standard Model	10
2.1.2	Lepton Flavor Violation in Neutrino Oscillations	13
2.1.3	τ leptons in the SM	14
2.2	Lepton Flavor Violation via New Physics	15
3	The Belle II Experiment	17
3.1	From Belle to Belle II	17
3.2	SuperKEKB	18
3.3	Belle II Detector	20
3.3.1	Vertex Detector	20
3.3.2	Central Drift Chamber	20
3.3.3	Cherenkov Detectors	24
3.3.4	Electromagnetic Calorimeter	24
3.3.5	K_L^0 and μ Detector	25
3.4	Beam-Induced Background	26
3.5	Trigger Systems	26
4	MC Analysis of $\tau \rightarrow \mu \pi^0$	29
4.1	Analysis Setup	29
4.1.1	$\tau \rightarrow \mu \pi^0$ at Belle and BaBar	29
4.1.2	Monte Carlo Simulation	29
4.1.3	Analysis Software	30
4.2	Analysis Approach	33
4.3	Reconstruction efficiency	33

TABLE OF CONTENTS

4.4	Preselection	36
4.5	Signal and Background Samples	40
4.5.1	Signal Kinematics	40
4.5.2	Background Kinematics	44
4.6	2D Cut on ΔE and $ \vec{p}_{\text{muon}}^{\tau\text{RF}} $	47
4.7	Cut on Muon ID	49
4.8	Cut on Visible Energy	50
4.9	Cut on Polar Angle of Missing Momentum	52
4.10	Cut on Opening Angle between μ and π^0 in CMS	54
4.11	Cut on Tighter Signal Region	55
4.12	Summary and Upper Limit Prediction	57
5	Conclusion and Outlook	59
	Appendix	61
A	Analysis Plots	63
B	Calculation of the Upper Limit	89

1 Introduction

“You never know where a breakthrough might occur, so please pursue various possibilities for potential research.” This was Makoto Kobayashi’s message to young researchers in an interview he gave not long after being awarded the Nobel Prize in Physics in 2008 for explaining \mathcal{CP} violation within the Standard Model (SM) [1]. Today, with the clear necessity for New Physics (NP) popping up in various areas of particle physics, this message is more important than ever.

With the discovery of the Higgs boson in 2012 [2], the last missing piece of the SM was confirmed. But there were still phenomena remaining, that could not be explained by it: our universe’s matter-antimatter asymmetry, origins of gravity, the fact that there are exactly three generations of quarks and leptons and many more are questions to which the SM cannot give a sufficient answer. These increase the interest in finding NP by various means in different areas. Currently the muon is a favored candidate for finding hints for NP, as they recently discovered discrepancies in its anomalous magnetic moment at Fermilab [3]. But also neutrinos, of which too little is yet known due to their small interaction cross sections, are providing further hints for NP. Large-scaled experiments like the IceCube experiment in Antarctica or the Super-Kamiokande experiment in Japan were designed to unravel more on these mysterious particles. At CERN new particles and phenomena are hoped to be found by increasing the center of mass (CM) energy even further from 14 TeV (LHC) to 100 TeV in a proposed next-generation collider.

The path Belle II took, was not to increase the energy, but to drastically increase the luminosity of the collider compared to its predecessor Belle. With increased luminosity, precision studies and searches for NP are strongly enhanced.

In this thesis, we also search for NP by looking into the Lepton Flavor Violation (LFV) decay $\tau \rightarrow \mu \pi^0$, which is strictly forbidden by the SM. As a first approach to this decay at Belle II, we analyse the signal and possible backgrounds in a Monte Carlo (MC) study.

After theoretical introduction to the SM, τ -leptons and LFV in chapter 2, an overview about the Belle II detector and its accelerator SuperKEKB is given in

chapter 3.

The first part of the analysis in chapter 4 is on understanding the simulated performance of our detector and knowing its limitations. Then, we study the performance of the preselection and its effect on the reconstructed signal candidates. The main part of the analysis is the presentation of possible cuts by exploiting our decay's specific kinematics and targeting specific types of background. The goal of the cuts is to reduce the background to a minimum, while still preserving enough sensitivity for the NP signal.

Finally, we compare our result with the Belle and BaBar experiments, which both have previously studied this decay channel and we conclude, how Belle II's chances are to compete according to this study, while giving a first upper limit prediction based on our results.

2 Physics Overview

2.1 The Standard Model of Particle Physics

The Standard Model of particle physics is describing the fundamental particles and forces observed in our universe. All matter is found to be made out of SM elementary particles (see fig. 2.1) or their antiparticle equivalents. These particles interact with each other via four fundamental forces. These are the electromagnetic force, the weak force, the strong force and the gravitational force. Gravity is not

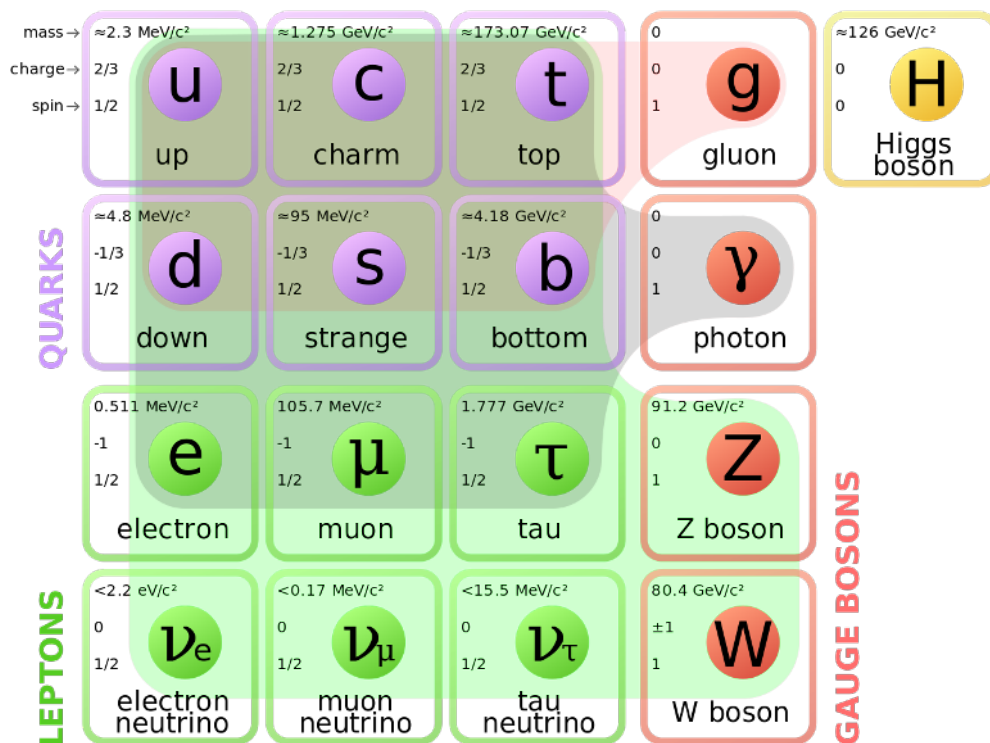


Figure 2.1: All particles of the Standard Model [4]

part of the Standard Model, as currently no theory is able to combine the SM and general relativity, the most accurate description of gravity. Also, until today, no experiments have been able to find evidence for a force carrier particle of gravity, whereas for all other forces they are well known. The magnitude of gravity is by many orders of magnitude smaller than the magnitude of other forces and can usually be neglected in high-energy particle physics.

Elementary particles can be classified into two categories according to the value of their spin: Fermions (half-integer spin) and bosons (integer spin). Fermions can again be categorized into quarks and leptons. Quarks occur only in a bound state together with other quarks, for example in a three-quark baryon state like the proton or neutron. They can also occur in a two-quark meson state consisting of one quark and one antiquark. This is due to the so-called confinement of the color-charge, which all quarks and gluons carry. Gluons, the force carrier of the strong force, only couple to color-charged particles. All other particles, like leptons, the photon and the weak bosons, are unaffected by the strong force. The electromagnetic force on the other hand couples to the electromagnetic charge of a particle via photons as force carriers. The weak force couples to the weak isospin, where all left-handed up-type quarks and charged leptons have a value of $+\frac{1}{2}$, while all left-handed down-type quarks and neutrinos have the value $-\frac{1}{2}$. Right-handed antiparticles have a opposite value respectively, while right-handed particles and left-handed antiparticles have a weak isospin of zero. The force carriers, which are called W^\pm and Z^0 bosons, are not massless like photons and gluons, which causes the weak interaction to be short-ranged. Quarks and leptons exist in three generations, also called flavors, visible as the three columns on the left side in fig. 2.1. The weak force is the only force that can cause a transition between these. Lastly, the Higgs boson has a spin equal zero and is linked to the mass of matter and thus its interaction strength is proportional to the mass of the particle coupling to it.

2.1.1 Conservation Laws and Quantum Numbers in the Standard Model

The particles in the SM are classified by their quantum numbers. These are beside straight-forward properties like electromagnetic charge or mass also more abstract ones like isospin or flavor. Interactions in the SM have to follow certain conservation rules depending of what kind of force is considered. Tab. 2.1 shows an overview of these restrictions.

Baryon number \mathcal{B} and lepton number \mathcal{L} are defined as the difference in number

Quantum Number	Symbol	Conserved in Interaction		
		EM	weak	strong
Baryon Number	\mathcal{B}	✓	✓	✓
Lepton Number	\mathcal{L}	✓	✓	✓
Electromagnetic charge	Q	✓	✓	✓
Weak Isospin	\mathcal{T}_3	✓	✓	✓
Momentum-Parity	\mathcal{P}	✓	✗	✓
Charge-Parity	\mathcal{C}	✓	✗	✓
Energy	E	✓	✓	✓
Momentum	P	✓	✓	✓
Orbital Angular Momentum	L	✗	✗	✗
Spin	S	✗	✗	✗
Tot. Angular Momentum	J	✓	✓	✓
Tot. Angular Mom. 3rd Comp.	J_3	✓	✓	✓
Strong Isospin	I	✗	✗	✓
Strong Isospin 3rd Component	I_3	✓	✗	✓
Quark Flavors	$\mathcal{B}_{S,C,B',T}$	✓	✗	✓
Lepton Flavors	$\mathcal{L}_{e,\mu,\tau}$	✓	✓	✓

Table 2.1: Overview of which quantum numbers are conserved in the final state of the respective interaction according to classical SM-theory ($m_\nu = 0$). [5]

of quarks/leptons minus antiquarks/antileptons present in a process. Together with the electromagnetic charge Q and weak isospin \mathcal{T}_3 they are always conserved. Other quantum numbers can describe the behaviour of particles under symmetry transformations. Spatial-parity \mathcal{P} and charge-parity \mathcal{C} tell us, how particles behave when all their spatial coordinates are inversed or when all particles are replaced by their respective antiparticles. The weak interaction is the only force that violates these two symmetries and is responsible for breaking even the combination of both, the so-called \mathcal{CP} -symmetry. While energy E and momentum P are conserved in all interactions, orbital angular momentum L and spin S in general are not. Their combination, the total angular momentum J however is always conserved and so is its third component J_3 . The strong isospin I has a value of $\frac{1}{2}$ for the two lightest quarks with its third component being $+\frac{1}{2}$ for the up-quark and $-\frac{1}{2}$ for the down-quark. For all other particles it equals zero. Its total value is only preserved in strong interactions, but the third component I_3 additionally also in electromagnetic interaction. Similar to the third component of the isospin, the quantum numbers strangeness S , charmness C , bottomness B' , topness T can be assigned to the other quark types respectively. These numbers are also conserved in strong and

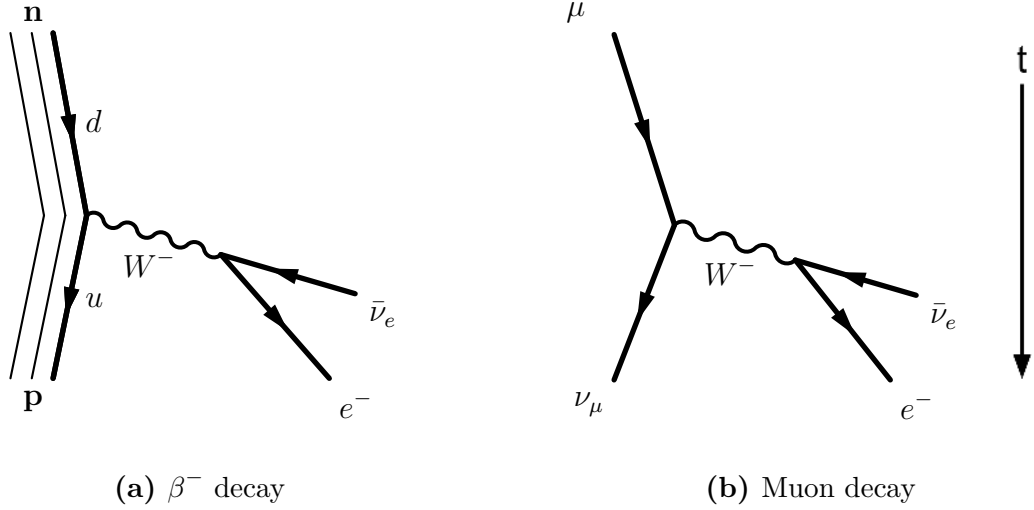


Figure 2.2: Examples for conservation of lepton flavor in the SM

EM interactions, but not in weak interactions. Lepton flavor $\mathcal{L}_{e,\mu,\tau}$ is assigned to leptons according to the generation or column they are in, charged leptons and neutrinos form three flavor pairs in total. Leptons are assigned the lepton flavor number $\mathcal{L}_{e,\mu,\tau}(\ell) = 1$, and anti-leptons $\mathcal{L}_{e,\mu,\tau}(\bar{\ell}) = -1$ according to their flavor respectively. In classic SM-theory, lepton flavor number is always conserved, which means, that before and after interaction, the sum of these numbers each has to remain the same. One examples can be seen in fig. 2.2a, where a neutron decays into a proton, an electron and an electron anti-neutrino. In the initial state, no leptons are present, $\mathcal{L}_{e,\mu,\tau} = 0$. In the final state this is also the case, since the flavor of the electron and anti-electron-neutrino cancel each other out again. In the other example, fig. 2.2b, a muon decays leptonically. Thus the final state also needs to fulfill $\mathcal{L}_\mu = 1$ while $\mathcal{L}_{e,\tau} = 0$. This is why in this decay there are two neutrinos present after the decay in addition to the electron.

The Standard Model can describe almost all of observed physics with accurate precision, however the better it is understood, the more its limits also become evident. Besides gravity not being included at all in this theory, the SM also cannot give explanations for the large difference in amount of matter and antimatter in our observable universe. Recently, scientists at Fermilab have found strong discrepancies between SM prediction and measurement in studying the g-2 parameter in muon experiments [3]. This all leads many physicists to believe, that there has to be also physics beyond the Standard Model, so-called New Physics. One other hint for NP is also the violation of lepton flavor, which, despite being forbidden in the SM, occurs in the case of so-called neutrino flavor oscillations.

2.1.2 Lepton Flavor Violation in Neutrino Oscillations

The first time that hints for Lepton Flavor Violation (LFV) were discovered, when the flux of neutrinos coming from the sun was measured and amounted to up to two thirds lower than expected. In later experiment this could be further solidified, until finally the Sudbury Neutrino Observatory (SNO) in Canada provided evidence for flavor change in 2001 [6]. The process of nuclear fusion in the sun produces only electron neutrinos and the first solar neutrino experiments were only sensitive on this flavor. The experiment at SNO however was sensitive to all neutrino types. Having this discriminatory power, it was possible to confirm, that the total flux of neutrinos equals the expected value, but only roughly a third of them remained as electron-type neutrinos.

This change in flavor is only possible if neutrinos have a mass unequal zero, since for an oscillation like this to occur different mass states have to be present [7]. Today, the upper limit for the sum over the masses of all three types, is found to be smaller than 0.120 eV. Extracting oscillation parameters from data collected from the many neutrino experiments, one can predict the probabilities for finding each neutrino flavor. When simplifying the case to just two neutrino flavors α and β present in the oscillation, the probability of a neutrino changing its flavor to the other can be expressed as

$$P_{\alpha \rightarrow \beta, \alpha \neq \beta} = \sin^2(2\theta) \sin^2 \left(1.27 \frac{\Delta m^2 L [\text{eV}^2][\text{km}]}{E [\text{GeV}]} \right). \quad (2.1)$$

The mixing angle θ is a parameter derived from experiments, Δm^2 is the squared difference $|m_\alpha^2 - m_\beta^2|$ between the two neutrino mass eigenstates in eV^2 . L stands for the distance traveled in km, and E for the neutrino's energy in GeV. Due to all neutrinos having a very small mass, the mass difference Δm^2 is minimal being in orders of 10^{-4} eV^2 , which means oscillations usually require long travel distances to be measurable.

An exact explanation for why neutrinos oscillate in this way is hard to give, since due to its tiny mass, precision measurements pose a major challenge. The SM can be extended to also take into account a non-zero mass for neutrinos and with it making LFV oscillations possible [8]. Having neutrinos not conserving lepton flavor, it poses the question, whether also for charged leptons LFV can occur. According to the SM charged leptons are highly unlikely to show similar behaviour to the neutrinos [9]. The only way charged leptons could cause lepton flavor violation is via NP. τ leptons are a popular candidate to search for NP, since due to its high mass its decays are more sensitive for possible phenomena beyond the SM.

$$\begin{array}{rcl}
\tau \rightarrow \ell \nu_\ell \nu_\tau \text{ (35\%)} & \rightarrow & 35\% \\
& & 50\% \} \text{ 1-Prong} \\
& \nearrow & \\
\tau \rightarrow qq' \nu_\tau \text{ (65\%)} & \rightarrow & 15\% \} \geq 3\text{-Prong}
\end{array}$$

Figure 2.3: Decay modes of τ depending on the number of charged particles (Prongs) in the final state.

2.1.3 τ leptons in the SM

The τ lepton is the heaviest lepton with a mass of $(1776.86 \pm 0.12) \text{ MeV}/c^2$ and a charge of $\pm 1 e$. Its average lifetime is $(2.903 \pm 0.005) \cdot 10^{-13} \text{ s}$ and according to the SM it can decay via leptonic and semi-leptonic modes [10]. It most commonly decays into a lepton and two neutrinos as well as into one or more pions and a neutrino as can be seen in fig. 2.2. Decay modes of the τ lepton can be categorized depending on the amount of charged tracks that are produced in the final state, the so-called "Prongs". Most of the τ lepton's final states are 1-Prongs. The fully leptonic decays all count as 1-Prongs and also most of the semi-leptonic decay modes have only one charged particle in its final state, which adds up to around 85% of all decays being 1-Prongs and only 15% to be 3-Prongs or higher (see fig. 2.3).

	Decay Channel	Branching Fraction
Leptonic Decay Modes	$\tau \rightarrow e \nu_e \nu_\tau$	$(17.82 \pm 0.04) \%$
	$\tau \rightarrow \mu \nu_\mu \nu_\tau$	$(17.39 \pm 0.04) \%$
Hadronic Decay Modes	$\tau \rightarrow \pi \pi^0 \nu_\tau$	$(25.49 \pm 0.09) \%$
	$\tau \rightarrow \pi \nu_\tau$	$(10.82 \pm 0.05) \%$
	$\tau \rightarrow 3\pi \nu_\tau$	$(9.31 \pm 0.05) \%$
	$\tau \rightarrow \pi 2\pi^0 \nu_\tau$	$(9.26 \pm 0.10) \%$
	$\tau \rightarrow 3\pi \pi^0 \nu_\tau$	$(4.62 \pm 0.05) \%$
	$\tau \rightarrow K^*(892) \nu_\tau$	$(1.20 \pm 0.07) \%$
	$\tau \rightarrow \pi 3\pi^0 \nu_\tau$	$(1.04 \pm 0.07) \%$
	$\tau \rightarrow \bar{K}^0 \pi \nu_\tau$	$(0.840 \pm 0.014) \%$

Table 2.2: Most common τ decay modes

2.2 Lepton Flavor Violation via New Physics

Theorists have designed many possible NP-models, that make LFV decays of SM particles possible. One example of a LFV decay is $\tau \rightarrow \mu \pi^0$, on which this thesis focuses on. Many models predict a high sensitivity for this channel, meaning that if the model is correct and enough data is available, this decay should be observable [11]. Some of these models are:

- **Theories with extended Higgs-sector:** One or more additional Higgs particles h' or H' are assumed. These can couple to different flavors at once, thus allowing also LFV [12].
- **Theories with extra Z' :** Grand unified theories, Supersymmetry (SUSY) and other models predict additional Z' bosons that allow changes in lepton flavor [12, 13].
- **Leptoquarks and charginos in SUSY models:** Supersymmetric particles like leptoquarks (LQ) can violate lepton and baryon number by directly changing quarks into leptons and vice versa or charginos change flavor in loop processes [14, 15].

The NP processes that would allow the decay $\tau \rightarrow \mu \pi^0$ can either occur on a tree-level as seen in fig. 2.4, or via a loop as in fig. 2.5. Many NP models exist and can create this decay on a tree-level. In fig. 2.4a the particle, that causes the LFV could be either a new type of Z boson Z' , an additional Higgs boson h' , or a supersymmetric higgsino \tilde{H} . These new particles couple simultaneously to leptons of different flavors and thus are able to transform a τ into a μ . They can decay into a quark-antiquark pair, which then together can form a neutral meson for example a π^0 . In case of the diagram in fig. 2.4b, an incoming τ could be transformed into a quark and a leptoquark. This leptoquark can decay into a muon and an antiquark. The two quarks then can form for example a π^0 . Fig. 2.5 shows possible decays containing loops in a SUSY model [14]. In the loop, a new particle $\tilde{\chi}^\pm$ called chargino together with a sneutrino $\tilde{\nu}$, the supersymmetric partner of the neutrino, is created out of a charged SM lepton, and can then combine again into a charged SM lepton of a different flavor.

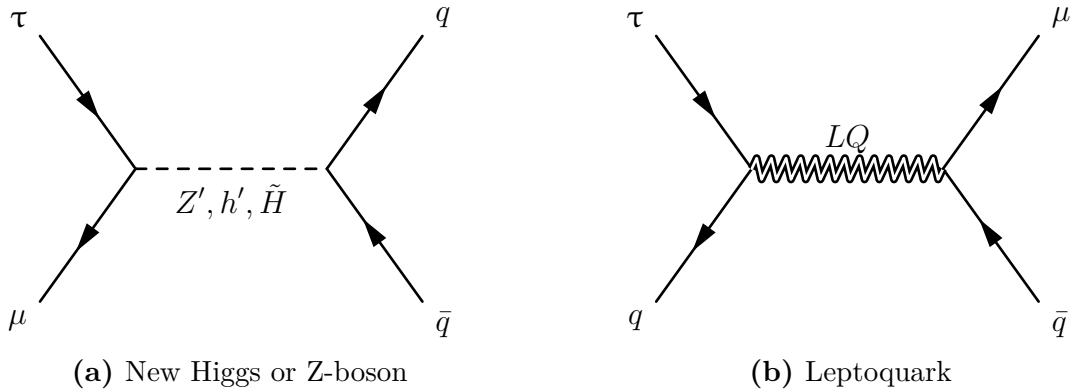


Figure 2.4: Diagrams of NP-tree-level decays, that show a tau decaying into a muon and a $q\bar{q}$ pair that can form a neutral meson, e.g. a π^0 . On the left the flavor change is caused by a new H' or a Z' boson, on the right by a leptoquark.

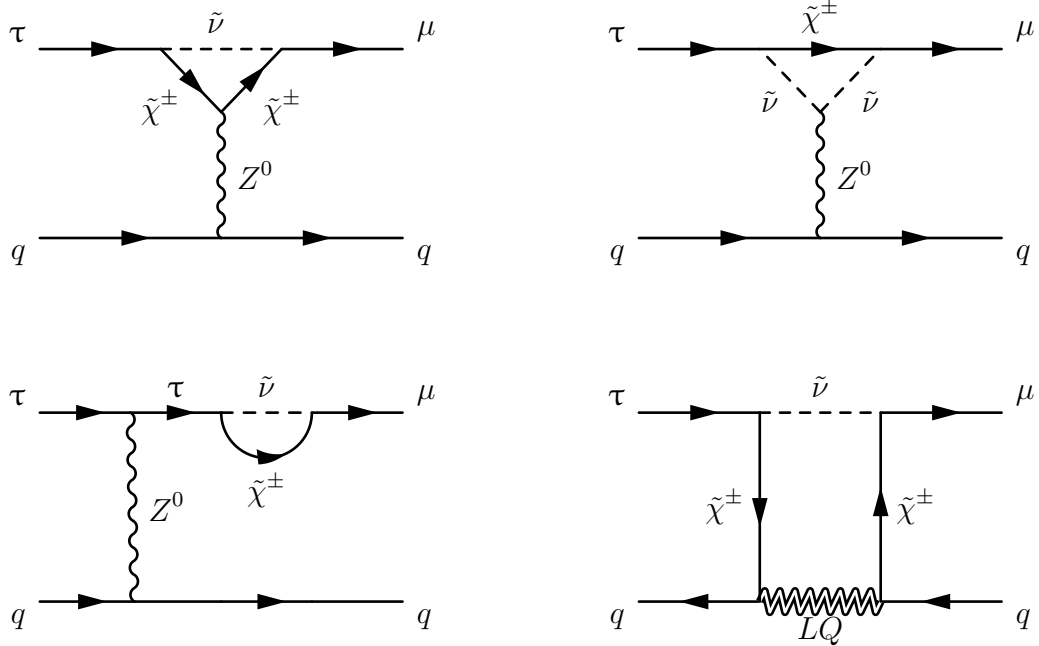


Figure 2.5: Examples of possible LFV loop diagrams in SUSY models using charginos $\tilde{\chi}^\pm$, sneutrinos $\tilde{\nu}$ and leptoquarks.

3 The Belle II Experiment

3.1 From Belle to Belle II

The Belle experiment at KEK and the BaBar experiment at the Stanford Linear Accelerator Center (SLAC) are known as the leading e^+e^- collider experiments of the early 2000s. These experiments had major parts in further establishing the SM and created many results, that today are still uncontested by any other experiment [16]. Belle stopped taking data in 2010, when already plans were made to relaunch an improved version of the experiment. While its location remains in Tsukuba, Japan, the accelerator KEKB is upgraded to SuperKEKB and the detector is rebuilt with today's state-of-art technology under the name Belle II. The new setup is aiming for an up to 30 times higher instantaneous luminosity of $\mathcal{L} = 6 \cdot 10^{35} \text{ cm}^{-2} \text{ s}^{-1}$ and was able to take its first data in 2019. The instantaneous luminosity \mathcal{L} in a collider experiment can be expressed through

$$\frac{dN_P}{dt} = \sigma_P \cdot \mathcal{L}. \quad (3.1)$$

whereas $\frac{dN_P}{dt}$ stands for the collision rate of a process P with a cross section σ_P in the detector. Belle II aims for a drastic increase in the amount of recorded events in order to be sensitive to rare events and be able to conduct precision measurements. The number of recorded events N_P of a process can be acquired by integrating the instantaneous luminosity over time:

$$N_P = \sigma_P \int dt \mathcal{L} = \sigma_P \cdot L_{\text{int}}. \quad (3.2)$$

This integral is also often referred as the integrated luminosity L_{int} and corresponds to the number of data taken in an experiment. Belle and BaBar recorded about 1.5 ab^{-1} of e^+e^- data available, whereas the goal of Belle II is to collect a total of about 50 ab^{-1} . This corresponds roughly to 47 billion $\tau^+\tau^-$ pairs. Fig. 3.1 shows the experiment's overall schedule for peak and integrated luminosity.

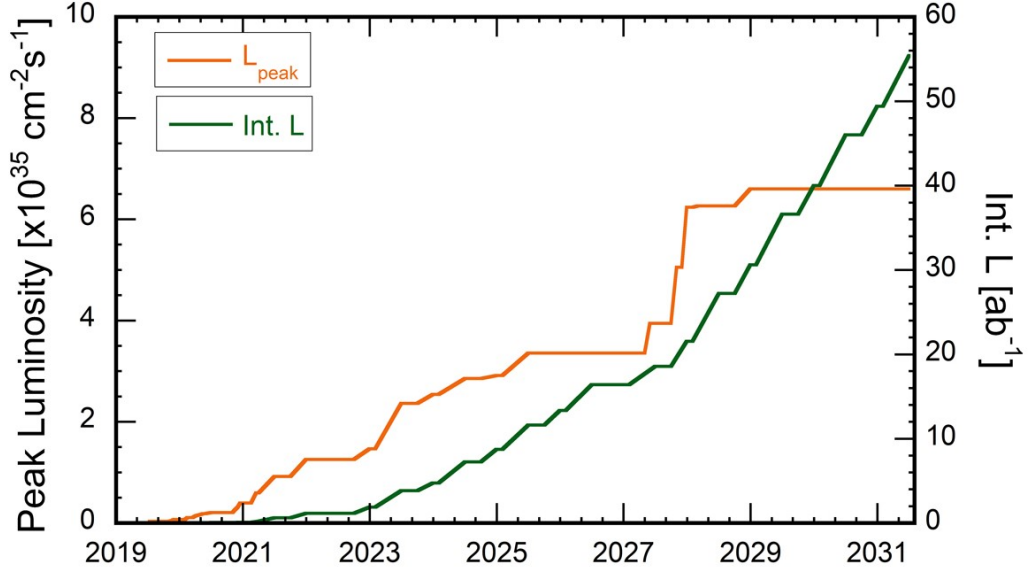


Figure 3.1: Schedule for the luminosity reached by SuperKEKB. The orange curve visualizes peak luminosity and the green curve the total integrated luminosity [17].

3.2 SuperKEKB

The SuperKEKB collider accelerates e^+e^- pairs on a ring track with a circumference of 3 km to center of mass energies at and around the $\Upsilon(4S)$ resonance at $\sqrt{s} = 10.58 \text{ GeV}$. This state is chosen because it is slightly above the energy threshold required to produce a pair of B-Mesons, which have a mass of $5.28 \text{ GeV}/c^2$ and thus experiments like these are also called "B-factories". For many B-physics analysis a boosted center-of-mass system is essential, which is why the collider creates asymmetric beam energies. The positron is accelerated to 4 GeV and the electron to 7 GeV. After creation and acceleration these particles are injected into storage rings in opposite directions and finally collide at the interaction point (IP) as can be seen in fig. 3.2. Electrons and positrons are produced and collided in bunches, which do not collide head-on, but at a small angle to each other. The collision system is strongly inspired by the setup of its predecessor KEKB, however in order to achieve the high instantaneous luminosity goal, overall major upgrades have been made [18]. One of the most significant one is the implementation of the so-called nano-beam scheme, where the beam size at the collision point is squeezed by superconducting quadrupoles and reduced by a factor of 20 from about $1 \mu\text{m}$

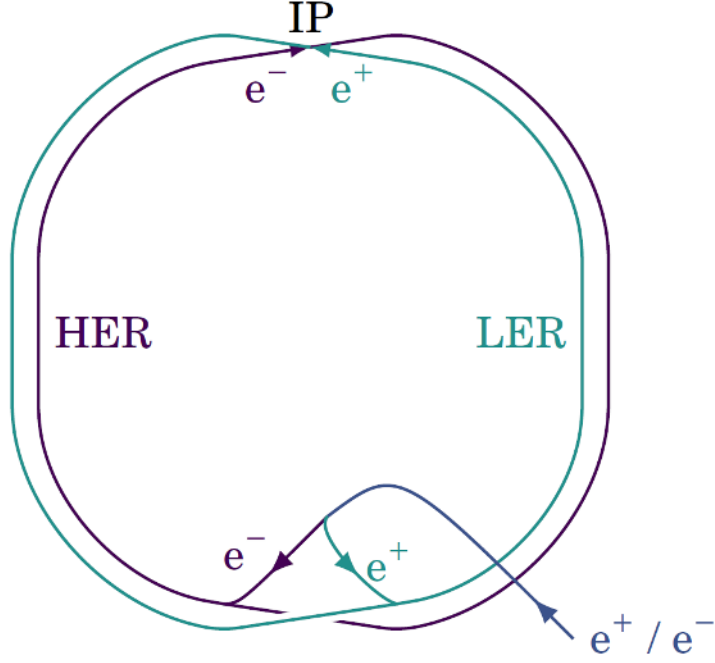


Figure 3.2: Schematics of the SuperKEKB storage ring structure, with the low energy ring (LER), the high energy ring (HER) and the injection tunnel leading to the linear accelerator. The electrons and positrons collide at the interaction point (IP) [20].

to 50 nm [19]. This increases the possible luminosity of the experiment directly. Taking a simplified approach to the luminosity in a collider experiment it can be expressed as

$$\mathcal{L} \propto \frac{N_{e^+} N_{e^-}}{\sigma_x \sigma_y} f_C. \quad (3.3)$$

Here, N_{e^+} and N_{e^-} account for the total number of positrons and electrons in one colliding bunch respectively. σ_x and σ_y denote the root mean squares of the transverse beam size at the collision point and f_C the frequency with which bunches collide. In addition to the reduced transverse beam size, SuperKEKB plans to roughly double the beam current, which in theory would also directly double luminosity. However, the consequently higher event rate causes background effects to increase, which poses an additional challenge for the detector setup. Detectors have to be faster and more durable in order to handle the large amount of signal simultaneously, but still maintain high precision.

3.3 Belle II Detector

With the planned increase of instantaneous luminosity, also the background rates are expected to rise by a factor of 10 to 20 [18]. Mitigating the effects caused by this were a critical point for designing the parts of the detector. Additionally, the trigger scheme, data acquisition and computing had to be revamped or replaced. Located in the center of the Belle II detector setup is the IP, where the two beams collide inside a 2 cm diameter beryllium tube. The various sub-detectors, out of which Belle II is built of, are wrapped around this point in an onion-like fashion in order to cover as much solid angle as possible. Fig. 3.3 shows a 3D view of the hermetic detector and its coordinate system. The direction of the beam pipes define the z -axis with the interaction point set as $z = 0$, while the other two axes x and y form the transverse plane. In spherical coordinates, the azimuth angle ϕ goes around the z -axis and the polar angle θ moves in the xz -plane starting parallel to the z -axis. The detector region symmetric around the z -axis is also called barrel region, while the region in beam direction is called endcap region. Since the particles coming out of the IP are heavily boosted, most particles created in interactions move through the forward endcap region of the detector, which consequently requires more precise and durable detector elements than the barrel region. The arrangement of the sub-detectors is shown in fig. 3.4 and is briefly described in the following sections.

3.3.1 Vertex Detector

The innermost sub-detector of Belle II is the Vertex Detector (VXD), its function is to measure the trajectory of charged particles created in the interaction point with high precision. Matching its signal with information from other sub-detectors the VXD can determine decay vertices of particles with an accuracy of up to 50 μm . It consists of two different types of detectors. The two inner layers consist of Depleted P-channel Field Effect Transistor (DEPFET) type Pixel Vertex Detectors (PXD) positioned directly around the beryllium pipe, followed by four layers of double-sided silicon strip detectors, the Silicon Vertex Detector (SVD), of which the outermost ones are partially inclined to cover a bigger solid angle as seen in fig. 3.5 [18].

3.3.2 Central Drift Chamber

The Central Drift Chamber (CDC) is Belle II's main tracking device and measures the momenta of charged particles and the energy loss, which plays a key role in

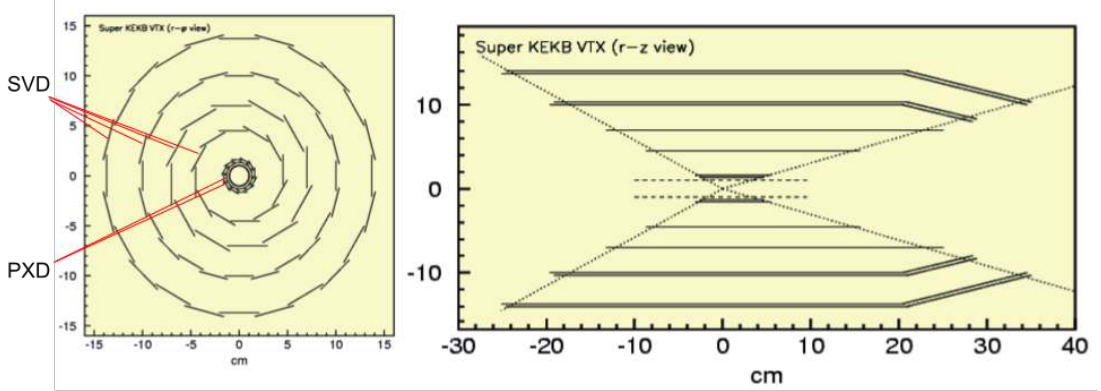


Figure 3.5: Schematic view of the Belle II vertex detector with a Be beam pipe, two pixelated layers and four layers of silicon strip sensors [19].

particle identification. It is a large sub-detector with its chamber surrounding the VXD. The chamber is filled with a gas mixture of 50-50 helium and ethane and consists of 50 cylindrical layers. Each layer contains between three and six axial or small-angle stereo layers, and three cathode strip layers. It is structured in an array-shape of 14336 sense wires and 42240 field wires, with a high voltage applied between sense and field wires. Incoming charged particles ionize the gas mixture as they pass through the chamber. These free electrons drift towards the sense wires and ionize gas molecules on their way. This creates a charged avalanche and when it reaches the sense wire, a measurable current is produced, which is then registered as a hit. Through combining the information on hits in the axial and stereo layers, a 3D-track can be reconstructed. All sub-detectors apart from the outermost one are suspended inside a magnetic field of 1.5 T created by a superconducting solenoid magnet. This causes charged tracks to bend due to the Lorentz force, which allows the CDC to reconstruct the particle's charge and momentum based on the curvature. The sub-detector covers a polar angle θ between 17° and 150° and the azimuth angle ϕ fully. In fig. 3.7 one can see an 2D-view of a two-track event in the CDC with the hits in the axial and stereo layers forming a reconstruction of the charged particle's track [18].

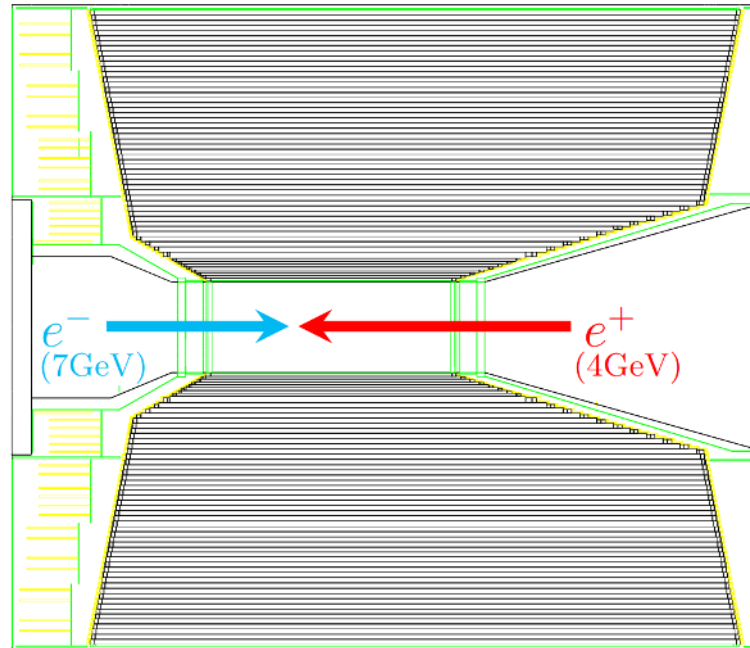


Figure 3.6: Longitudinal view of the CDC. Borders of the 50 cylindrical layers wrapped symmetrically around the beam are depicted in black [23].

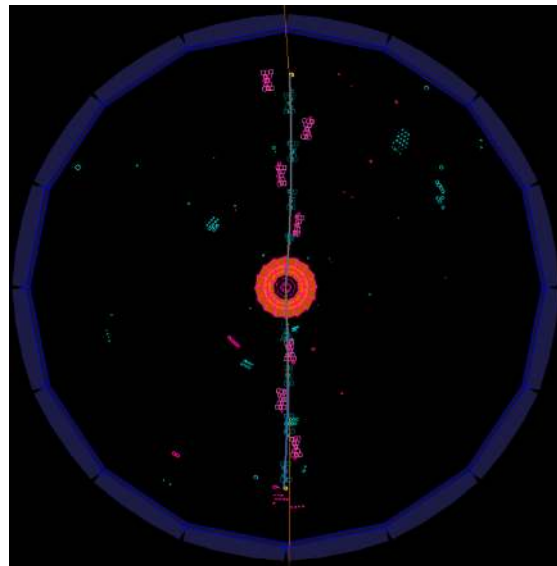


Figure 3.7: View in beam direction of a two-track event recorded in the Central Drift Chamber (CDC).

3.3.3 Cherenkov Detectors

In addition to determining a particle's momentum, one still needs information about its mass or velocity in order to identify it. The two types of cherenkov detectors at Belle II also serve this purpose. The Aerogel Ring-Imaging CHerenkov (ARICH) is located in the forward endcap region, where due to the boosted center of mass energy the highest amount of particles fly through. It covers the polar angle of 17° to 35° . The Time of Propagation (TOP) detector slightly overlaps with this area and covers the remaining barrel region of 32° to 120° .

Cherenkov light is produced, when a particle with velocity v moves in a medium with refractive index n and is faster than light would be in the same medium. The angle θ_C , under which this light is emitted depends on the velocity of the particle according to the relation

$$\cos \theta_C = \frac{c}{n \cdot v},$$

where c stands for the speed of light. In the ARICH detector θ_C is measured by sending the particle through an aerogel radiator, that creates a light-cone which hits the photon detector located behind the aerogel radiator in shape of a ring. With the ring's size the angle θ_C can be calculated and thus the particle's velocity as can be seen in fig. 3.8. In the Time of Propagation (TOP) Detector, cherenkov photons are emitted inside a quartz radiator, when a charged particle flies through. These photons are reflected inside the radiator until arriving at the photon sensor located at the end. Combining information from the charged particle's track, and the position, where the photons are detected at after reflection, the cherenkov angle can be determined and with it the particle's velocity [18].

3.3.4 Electromagnetic Calorimeter

The Electromagnetic Calorimeter (ECL) is used to detect gamma rays as well as to identify electrons, i.e. separate electrons from charged hadrons, in particular charged pions. It is a highly-segmented array of thallium-doped caesium iodide CsI(Tl) crystals. All three detector regions, barrel as well as the forward and backward endcaps, are instrumented with a total of 8736 crystals, covering about 90% of the solid angle in the centre-of-mass system [19]. It is sensitive to a polar angle of $12.4^\circ < \theta < 155.1^\circ$, except for two about $\sim 1^\circ$ wide gaps between the barrel and endcaps. Incoming electrons create bremsstrahlung photons, which can pair-produce e^+e^- pairs, which then cause again bremsstrahlung photons creating a cascade of particles. The process repeats, until the energy of the particles falls under a certain threshold, where the low energy positrons and electrons create

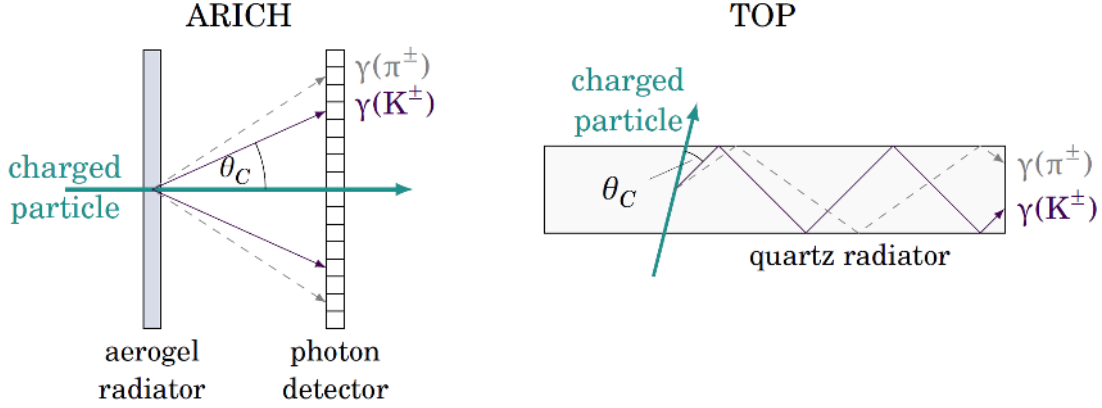


Figure 3.8: Working principle of the two Cherenkov detectors. In the ARICH, the Cherenkov angle θ_C is determined from the radius of the rings on the photon detector. In the TOP, the Cherenkov angle θ_C is related to the time of propagation of the Cherenkov photon [20].

scintillation light, that is measured at the end of each crystal. The measured energy is proportional to the initial particle's deposited energy. When the electromagnetic cascade matches with the track of a charged particle, the particle is identified as electron or positron, otherwise as neutral particle. Photons and other neutral particles can be differentiated by the size of the cascade.

3.3.5 K_L^0 and μ Detector

The outermost sub-detector is the K_L^0 and μ Detector (KLM) Detector, whose purpose is to identify long living neutral kaons and muons. It consists of an alternating sandwich of 4.7 cm thick iron plates and active detector. The iron plates serve as the magnetic flux return for the solenoid, which is located between the ECL and this sub-detector. They also provide 3.9 interaction lengths of more of material, beyond the 0.8 interaction lengths of the calorimeter, in which K_L^0 mesons shower hadronically. Muons do not create any showers, but are visible as curved tracks in the active part of this detector. The two innermost active layers consist of scintillator strips, that create signal photons which are sent through wavelength-shifting fibers to silicon photo multiplier (SiPM) readouts. They have a short dead-time and thus are suited for the high signal and background rates hitting the inner layers. The other active layers consist of glass-electrode resistive plate chambers (RPCs), which have a higher dead-time than SiPMs, but are overall more durable [19].

3.4 Beam-Induced Background

With the high energy and luminosity present at Belle II, background effects caused by the electron-positron beam are increased. The five main effects for this are [24]:

- **Touschek Scattering:** The charged particles inside a bunch Coulomb scatter with each other changing their energy. Because these particles then do not match the nominal energy of the bunch anymore, they eventually hit the inner wall of the beam-pipe and can cause showers, that hit the detector.
- **Beam-gas Scattering:** The beam interacts with residual gas molecules inside the beam-pipe via Coloumb or Bremsstrahlung scattering. This causes change in the particle's momentum or energy, which can lead them to also hit the inner wall of the beam-pipe and cause showers.
- **Synchrotron Radiation:** Moving on a circular path the charged particles in the beam experience acceleration constantly, which causes them to emit radiation. The energy range of the emitted photons can range from a few keV up to tens of keV.
- **Radiative Bhabha Process:** Through Bhabha scattering in the beam high-energy photons can be radiated, which interact with the iron of various magnets around the the beampipe and create neutrons. These neutrons are a main background in the KLM, whereas the remaining photons contribute as a main part of the background in the CDC.
- **Two-photon Process:** very low momentum electron-positron pairs produced via the two-photon process $ee \rightarrow eeee$. These particles spiral in the magnetic field and can cause multiple hits in the inner detectors of Belle II.

Although SuperKEKB has a wide range of measures implemented to keep the signal clear and to protect the detector from damages caused by this background, a non-neglegible portion reaches the detector elements and causes fake hits.

3.5 Trigger Systems

In order to deal with the high amount of signal created in the detector, a selection has to be made, of which events are being worth saving and stem from the interaction and which not. The amount of data, that can be processed at a time is limited through the Data Acquisition (DAQ) system's maximum read-in rate of 30 kHz.

Belle II has a two-level trigger scheme. The first level, also called the L1-trigger, is hardware-based and combines information from multiple detectors in a Global Decision Logic (GDL), which then decides to keep the event or not. From detection until decision the L1 requires a time of less than $5\ \mu\text{s}$. After this the data is sent to the software-based high-level trigger, which then further filters event-by-event in parallel processes. The fully reconstructed events are categorized by event-type ($B\bar{B}$, low multiplicity, etc.) and saved for further analysis. Due to Belle II's significantly higher luminosity a lot of improvements had to be made to handle the high amount of data, especially on the hardware level.

One example of this is the CDC Neuro Single Track Trigger (STT) [20], which greatly improves triggering on low-multiplicity events, to which also $\tau^+\tau^-$ events belong. The new technology enables to trigger reliably also on events with only one track, in which the other charged particle is emitted in a too shallow polar angle to be registered as a full track by the CDC. With the regular trigger, the outermost layers of the sub-detector need to be reached in order to be counted as a track and thus the polar acceptance range is effectively limited to $31^\circ < \theta < 126^\circ$. Also an event is only triggered on, if at least two full charged tracks are registered by the CDC. The STT however is trained with a neural network to identify incomplete tracks and can trigger on events with only one full track required. This reduces the limitation in the acceptance range and increases the triggering efficiency, especially for events with only two charged particles in the final state. τ analysis, that were focusing on these types of final states often suffered from low efficiency, but by introducing the STT these 1-1 topologies, which are the dominant decay channels of τ particles as shown in fig. 2.3, can be reliably reconstructed.

4 MC Analysis of $\tau \rightarrow \mu \pi^0$

4.1 Analysis Setup

4.1.1 $\tau \rightarrow \mu \pi^0$ at Belle and BaBar

The Belle and BaBar experiment have conducted searches for τ LFV decays in a multitude of channels, $\tau \rightarrow \mu \pi^0$ included. Since both experiments were taking data at electron-positron colliders similar to Belle II, looking at the methods used by these collaborations is helpful for this analysis. An overview of upper limits found by each experiment is shown in fig. 4.1. The graphic also includes a prediction of what Belle II could achieve by a simple estimation of taking the result of Belle and scaling it up from 1 ab^{-1} of data to the expected 50 ab^{-1} of Belle II. In a first instance the goal of this analysis is to make it competitive to the other two experiments if equal luminosities are assumed. Both experiments used cut-based approaches for their analyses, where events that do not fit certain criteria are filtered out, so that in the end the Background (BG) is as low as possible while the amount of discarded signal events is minimised. All cuts used in the analyses as well as the overall results at BaBar and Belle are shown in tab. 4.1 and 4.2. These cuts are the result of a process of systematic trial-and-error that builds on good understanding of the signal, the BG of this decay channel and also of the detector itself. Some of these cuts can be reapplied for the analysis at Belle II, but have to be carefully checked before. The following sections show the final results of this step-wise process of building up and improving selection criteria.

4.1.2 Monte Carlo Simulation

In modern particle physics, before working with actual data, we first do a blind analysis and only look at Monte Carlo (MC) simulation of the data to understand the physics of this process and to avoid a bias based on the eventual systematics. The MC study of the decay $\tau \rightarrow \mu \pi^0$ in Belle II is the main goal of this thesis.

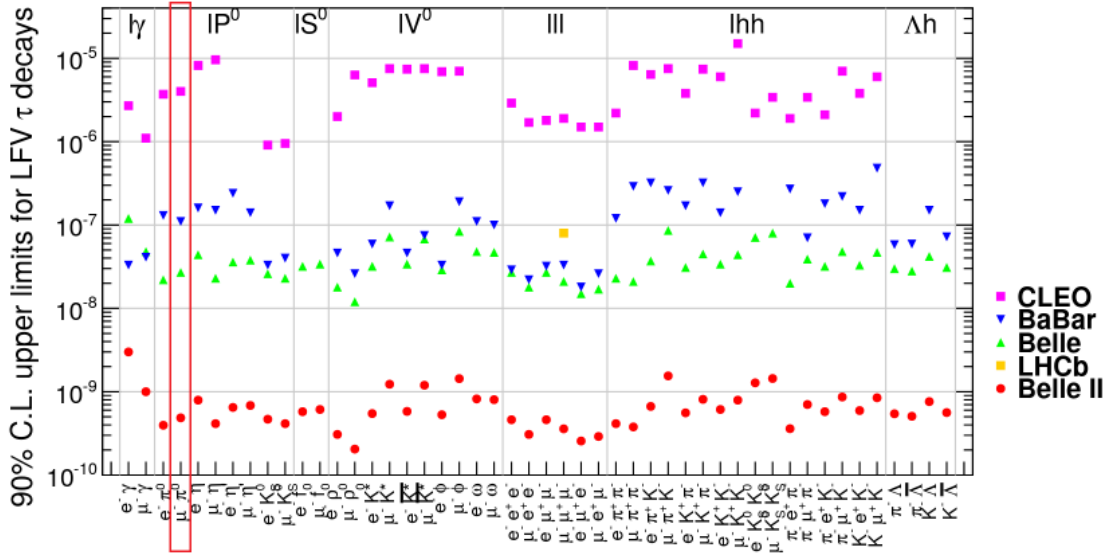


Figure 4.1: Current 90% C.L. upper limits for the branching fraction of τ LFV decays in the CLEO, BaBar and Belle experiments [19].

The MC-data is created by the Belle II data production group using the KKMC event generator [27] and contains a simulation of all physics of an event, detector effects and anticipated backgrounds due to collider operation. Reconstruction efficiencies and uncertainties are also taken into account, thus this MC simulation can be assumed to be a close imitation of real data [28]. Further, MC simulation allows simulation of signal events, e.g. creating a signal sample of one million $e^+e^- \rightarrow \tau^+\tau^-$ events, where one of the τ decays according to $\tau \rightarrow \mu \pi^0$ and the other τ decays in a generic way, i.e. following the branching ratios and phase space distributions of the SM. Here also each event includes simulated beam-background and interactions with the detector. These τ signal-samples are created using the TAUOLA software [29] by Belle II's official MC campaign.

4.1.3 Analysis Software

The core software used at Belle II is the Belle II Analysis Software Tool (basf2) [30], which is also the main tool for conducting analysis. It is a framework based on calculation-efficient C++ modules, that can be steered by python scripts. All recording and simulating steps are implemented in basf2, namely event generation, simulation, digitization, online trigger, reconstruction and analysis. For this analysis, the last two steps are the most relevant. Data, or in this case background and signal samples containing the processed detector information are used as input for

reconstruction. In this step particles are combined to reconstruct other particles and also preselections are possible, e.g. excluding very low energy photons caused by the interactions of particles with the detector. A collection of relevant variables is selected to use for the analysis. For each possible reconstruction combination i.e. each signal candidate, that also fits the preselection criteria, a collection of the chosen variables is saved and then used for further selection and analysis.

BaBar	
Cuts general	<ul style="list-style-type: none"> · 2 or 4 charged tracks, total charge = 0 · Photon conversion tracks rejected · $-0.76 < \text{polar angle of missing momentum} < 0.92$
Cuts signal side	<ul style="list-style-type: none"> · 1 or 3 tracks and 2 photons · $50 \text{ MeV} < E_\gamma < 100 \text{ MeV}$ in signal hemisphere · $0.115 \text{ GeV}/c^2 < m(\pi^0 \rightarrow \gamma\gamma) < 0.150 \text{ GeV}/c^2$ · $1.5 \text{ GeV}/c < p_{\pi^0}$ · track with $p > 0.5 \text{ GeV}/c$ and a identified as a muon by BaBar-Particle Identification (PID)
Cuts tag side	<ul style="list-style-type: none"> · total CM momentum on tag side $< 4.75 \text{ GeV}/c$ · total CM energy $\sum E_\gamma^{CM} < 0.2 \text{ GeV}/c^2$ · $m_{tag} < 0.4 \text{ GeV}/c^2$
2D-cut parameters	<ul style="list-style-type: none"> · $\Delta E, m_{EC}$ (beam-energy constrained τ-mass), $\pm 2\sigma$ around peak · $1.5 \text{ GeV}/c^2 < m_{EC} < 2.0 \text{ GeV}/c^2$, $-0.8 \text{ GeV}/c^2 < \Delta E < 0.4 \text{ GeV}/c^2$
Dominant BG	$\tau \rightarrow \rho\gamma$, $\tau \rightarrow e\nu\bar{\nu}\gamma$, ee , $\mu\mu$, $q\bar{q}$
Luminosity	339 fb^{-1}
Signal efficiency	$4.75 \pm 0.37 \%$
Expected BG	1.33 ± 0.15 (2σ -box)
Resolution	$\sigma(m_{EC}) = 9.0 \text{ GeV}/c^2$, $\sigma(\Delta E) = 46.4 \text{ MeV}$
Upper limit	$1.1 \cdot 10^{-7}$ (90% C.L.)

Table 4.1: Cuts and performance at BaBar at 339 fb^{-1} [25].

Belle	
Cuts general	<ul style="list-style-type: none"> · all tracks in $-0.866 < \cos \theta < 0.956$ · charged tracks $p_t > 0.1 \text{ GeV}/c$ · photon energies $E_\gamma > 0.1 \text{ GeV}$ · zero net charge of candidate tau-pairs · charged lepton momentum $0.115 \text{ GeV}/c < p_{l^\pm} < 0.152 \text{ GeV}/c$ · Visible energy: $5.29 \text{ GeV} < E_{vis}^{CM} < 10.0 \text{ GeV}$
Cuts signal side	<ul style="list-style-type: none"> · muon-PID > 0.9 with $p > 0.7 \text{ GeV}/c$ · reject radiative photons from electrons with $\cos \theta_{e\gamma} > 0.99$ · π^0-candidates $1.5 \text{ GeV}/c^2 < M_{\gamma\gamma} < 4.5 \text{ GeV}/c^2$ · $p_{\pi^0} > 0.1 \text{ GeV}/c$ · π^0-candidate photons: $E_{\gamma 1} > 0.9 \text{ GeV}$ and $E_{\gamma 2} > 0.2 \text{ GeV}$ · extra photon candidates $n_\gamma^{SIG} \leq 1$ · angle between μ and π^0: $0.5 < \cos \theta_{\mu-\pi^0}^{CM} < 0.80$
Cuts tag side	<ul style="list-style-type: none"> · missing momentum $\vec{p}_{miss} > 0.4 \text{ GeV}/c$ · angle to thrust and \vec{p}_{miss}: $\cos \theta_{miss-thrust}^{CM} < -0.55$ · extra photon candidates $n_\gamma^{TAG} \leq 2$ · correlation missing energy and tag momentum: $p_{tag}^{CM} > 1.1 \cdot \log(\cos \theta_{miss-thrust}^{CM} + 0.92) + 5.5$ and $p_{tag}^{CM} < 5 \cos \theta_{miss-thrust}^{CM} + 7.8$ · leptonic decay: $p_{miss} > -10m_{miss}^2 + 4$ and $p_{miss} > 1.1m_{miss}^2 - 0.3$ · hadronic decay: $p_{miss} > -5m_{miss}^2 - 0.25$ and $p_{miss} > 2.1m_{miss}^2 - 0.3$
2D-cut param.	· $\Delta E, M_{inv}$ (reconstructed invariant mass of τ), 2σ around peak
Dominant BG	$\tau \rightarrow \pi^\pm \pi^0 \nu_\tau$
Luminosity	· 401 fb^{-1}
Signal efficiency	· 4.53%
Expected BG	· 0.58 ± 0.34
Resolution	<ul style="list-style-type: none"> · $\sigma^{\text{high}}(M_{inv}) = 14.9 \text{ MeV}/c^2$, $\sigma^{\text{low}}(M_{inv}) = 19.1 \text{ MeV}/c^2$ · $\sigma^{\text{high}}(\Delta E_{inv}) = 33.8 \text{ MeV}/c^2$, $\sigma^{\text{low}}(\Delta E_{inv}) = 63.0 \text{ MeV}/c^2$
Upper limit	$1.2 \cdot 10^{-7}$ (90% C.L.)

Table 4.2: Cuts and performance of the at Belle at 401 fb^{-1} [26].

4.2 Analysis Approach

In this analysis SI-units are replaced by the natural units of particle physics, which set

$$\hbar = c = 1$$

and thus energy, momentum and mass are all expressed in the same unit of GeV.

Due to the short lifetime of the τ , it decays before traveling less than 1 mm inside the beam pipe, so only its decay products can be measured. When trying to reconstruct a decay of τ -pair events, the final states can never be fully reconstructed, since according to the SM each τ decays into at least one neutrino, which is always invisible to the detector. In this analysis however, the signal τ , which we are looking for, decays without a neutrino, and thus can be fully reconstructed. This is done by combining two photons into a π^0 and then combining this with a charged track, that later is constricted to be a μ , into a τ . The π^0 decays with branching ratio of 98.8% into two photons, so this reconstruction covers almost the full branching fraction. The small remaining fraction of 1.2% of the final states contain an electron positron pair and will not be reconstructed in our analysis.

The particles we detect in the event, but not use to reconstruct our signal τ , are all collected in a variable called Rest of Event (ROE). By this, the other τ is not explicitly reconstructed, but one can still access indirectly information about it through the ROE-variable. In most other τ analysis at Belle II this other τ , also called tag- τ , is reconstructed by requiring it to decay into certain final states. This approach however can be used to accept all final states of the tag- τ and does not automatically loose any events in this step by limiting the decay possibilities. Still, in a first instance, the events analysed here will be reduced to the ones with only two charged tracks, i.e. where the tag- τ decays as a 1-Prong. This simplifies the analysis, but in a later stage also the other Prongs can be considered to increase statistics.

Like Belle and BaBar, we perform a cut-based analysis approach with the main goal to reduce background to a minimum, while still maintaining an acceptable sensitivity for our decay channel.

4.3 Reconstruction efficiency

Before applying any selection criteria or any cuts, we first test, how well the detector reconstructs this decay according to the MC simulation. For this, we test a sample

of 300 000 signal events and reconstruct them like previously described. To be able to discriminate detector effects from physics effects, interactions of particles with the environment can be also turned off, to see the distributions of variables on a MC-generator level.

Since there are no cuts or filters in place yet, by reconstructing the signal τ a lot of false combinations occur, since for each combinatorial possibility one τ candidate is put together, regardless of it being physically realistic. To filter for the combinations, that belong to an actual simulated decay, basf2 has a variable called *isSignal*, that matches reconstruction with MC truth information. Requiring this variable to be true, only signal remains and the reconstructed variables can be well compared with the generator level, also called MC-4Vector, information. In fig. 4.2 the distributions of the momentum, transverse momentum, polar angle and azimuth angle of the μ are displayed. We observe, that the detector was able to find almost two-thirds of the generated events. We also see, that in the MC-4Vector data a few events are missing from the original 300 000. In these events the π^0 does not decay into two photons and thus, despite being signal, they are not counted in our reconstruction of $\tau \rightarrow \mu(\pi^0 \rightarrow \gamma\gamma)$. Taking a closer look at the polar angle θ distribution of the μ in the same figure, there is a sharp edge at around 17° and 150° . A similar edge can be seen in the polar angle distribution of the photons in fig. 4.3. This edge can be explained by the limited polar acceptance of the CDC (sect. 3.3.2) with which it coincides. Further this explains the high number of missing reconstructed μ with low transverse momentum p_t , since low transverse momentum implies a shallow polar angle. Additionally, a small dent is visible in the distribution of θ of the photon at around 30° and 130° . This is the border between the barrel and the endcap regions, which is not covered by the ECL due to mechanical reasons. In

Overall, only 64% of the signal is reconstructed by the detector, however when excluding all events outside of the CDC acceptance range, 231 820 4Vector-MC remain of which 182 702 are recorded by the detector. Including losses from the dents from the ECL's blind region, this is an effective reconstruction efficiency of 79%. This value will be higher in the future, since in this MC simulation the STT is not yet included, which would be able to further decrease the loss in signal by overcoming current two-track requirement of the current trigger system.

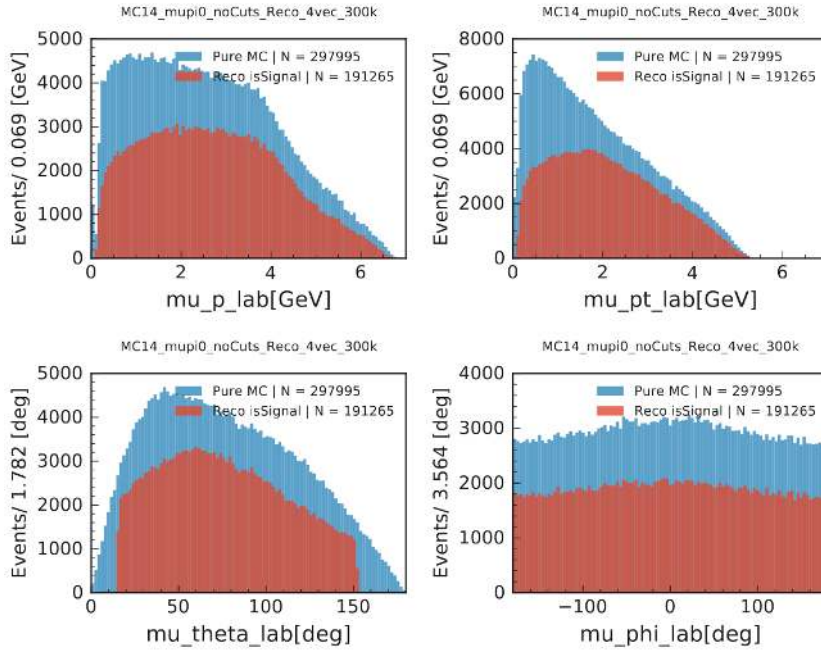


Figure 4.2: Comparison of generator level MC distributions (blue) to the by the detector correctly reconstructed muons (red).

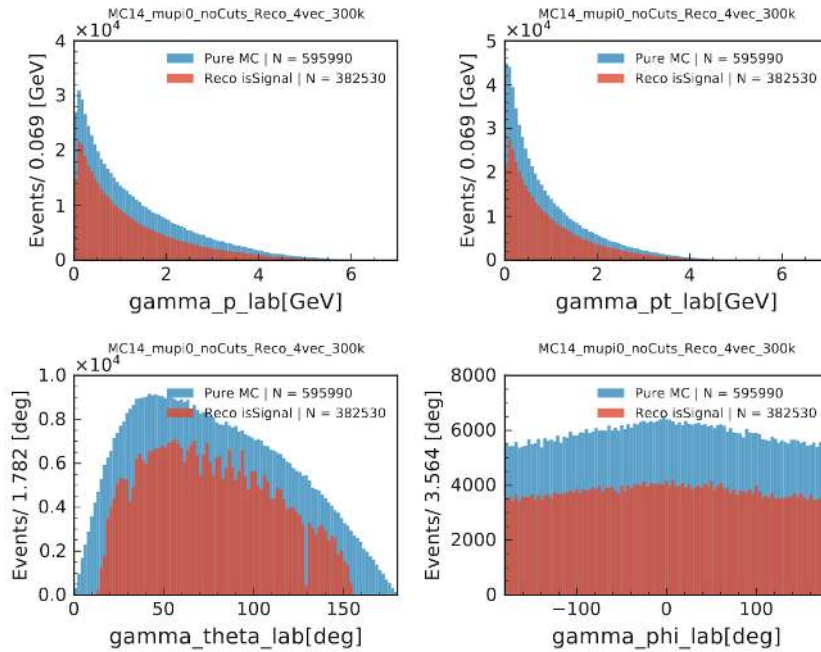


Figure 4.3: Comparison of generator level MC distributions (blue) to the by the detector correctly reconstructed photons (red)

4.4 Preselection

Loose Cuts for π^0 photons: <ul style="list-style-type: none"> • $E_\gamma > 0.1 \text{ GeV}$ • $17^\circ < \theta < 150^\circ$ • Cluster Hits $n_{\text{hits}} > 1.5$ 	Cut on π^0 reconstructed mass : <ul style="list-style-type: none"> • 0.115 GeV $< m(\pi^0 \rightarrow \gamma\gamma)$ $< 0.152 \text{ GeV}$
Track Cuts: <ul style="list-style-type: none"> • $-1.0 \text{ cm} < dz < 1.0 \text{ cm}$ • $dr < 1.0 \text{ cm}$ • $n(\text{charged-tracks}) = 2$ 	Hemisphere-Cuts: <ul style="list-style-type: none"> • μ and π^0 from same thrust-hemisphere • reconstructed signal τ and ROE from opposite thrust-hemisphere

Table 4.3: Preselection Cuts

A preselection is essential to reduce the overall amount of data during processing. When there are no restrictions in place during the reconstruction, τ candidates are constructed by combining all possible particles, that fit our reconstruction criteria of $\tau \rightarrow \mu(\pi^0 \rightarrow \gamma\gamma)$. We have to consider that, for example, when reconstructing the π^0 out of two photons, the amount of combinatoric possibilities grows quadratically with the number of photons. Thus, detected particles or event types, that are not relevant for the analysis or clearly do not stem from the initial collision, but from other sources, have to be filtered out beforehand, otherwise the data processing capacities can reach their limit rapidly.

The first part of preselection focuses on reducing the number of photons. Photons are required to have an energy of at least 0.1 GeV and a trajectory within the acceptance of the CDC. Also, since we expect two photons in the event, there should be a least two cluster hits inside the ECL. But in order to still keep events, where two clusters hit the ECL close to each other and therefore the value for number of hits n_{hits} falls slightly below two, we lower the requirement to $n_{\text{hits}} > 1.5$ instead of requiring $n_{\text{hits}} \geq 2.0$. To further reduce the number of background photons, we require the invariant mass of the reconstructed π^0 to be between 0.115 GeV and 0.152 GeV. Statistically 90% of all reconstructed π^0 lie within this

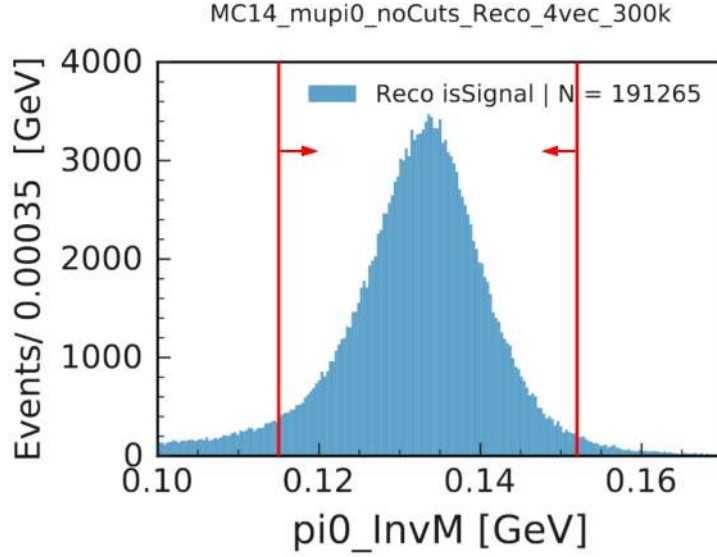


Figure 4.4: Reconstructed invariant mass of the π^0 . The red lines indicate the cut interval, in which 90% of the reconstructed π^0 lie.

interval and is depicted in fig. 4.4. The slight asymmetry in the reconstruction is caused by energy losses due to initial state radiation.

Next, we ensure that the tracks stem from the IP and are not caused by beam radiation or detector interactions. For this, we require the origin of the track to be not further away than 1 cm from the IP in all directions. Also at this point we want both τ leptons to decay as 1-Prongs, i.e. we require all events to have exactly two tracks.

For the final preselection we use the event observable called thrust and its direction, the thrust axis. The thrust T describes the degree, how back-to-back the momenta of particles are distributed in one event. It is defined through to the formula

$$T = \max_{\vec{n}} \frac{\sum_j |\vec{p}_j \cdot \vec{n}|}{\sum_j |\vec{p}_j|}. \quad (4.1)$$

Here \vec{p}_j stands for the momentum of each particle in the center of mass system (CMS) frame, \vec{n} is a normalized vector with $|\vec{n}| = 1$. The \vec{n} , which maximizes T is called thrust-axis \vec{n}_T . As the thrust is an indicator for the event shape, its distribution differs from event type to event type. Fig. 4.5 shows this difference, where the particles with high momenta due to energy conservation coming out of the IP, such as muon or electron pair events, have a thrust close to one. Events with high-mass particles, such as a pair of B-mesons, usually have a smaller thrust, as

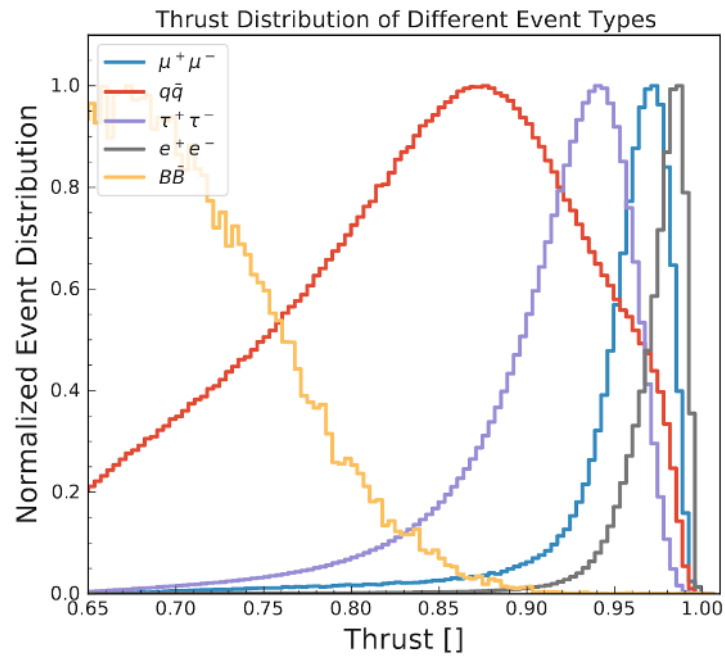


Figure 4.5: Distribution of the thrust observable for different event types. While events with a low momentum after collision, such as $B\bar{B}$ have a lower thrust value, strongly boosted event types have a value close to one.

most of the available energy is bound in form mass and the momentum of these particles is small. This makes the event in the CMS frame more spherical and less back-to-back. We know, that in an taupair event only a third of the available CM energy is bound in the mass, so the two τ leptons need to have a fairly high momentum each. Therefore it can be considered back-to-back, which is also why the thrust in these events is also closer to one. This means the particles they decay into are strongly boosted in opposite directions, which makes the momenta of most final state particles point in a similar direction as the τ they stem from. We can use the thrust-axis to define two hemispheres according to which we can divide each event respectively. Then, we require the charged track μ and the reconstructed π^0 to be from the same hemisphere. Additionally, we require the reconstructed signal τ and the ROE, which is composed out of mostly the other τ , to be from opposite thrust-hemispheres. An overview of the preselection cuts can be seen in tab. 4.3. To measure the performance and loss in signal caused by each preselection, each step and their combination was tested on a signal sample with 300 000 simulated events. The loss in correctly reconstructed candidates is shown on the left side of fig. 4.6. The right side of the figure shows the number of all candidates reconstructed on a logarithmic scale, of which the ones, that are actually signal, are colored in red. On one hand we see, that after all preselection cuts, only around a third of the generated signal is left. On the other hand the tremendous amount of false candidates is shrunken down to a manageable size. With this, we can move on to analysing the actual signal sample and the background events.

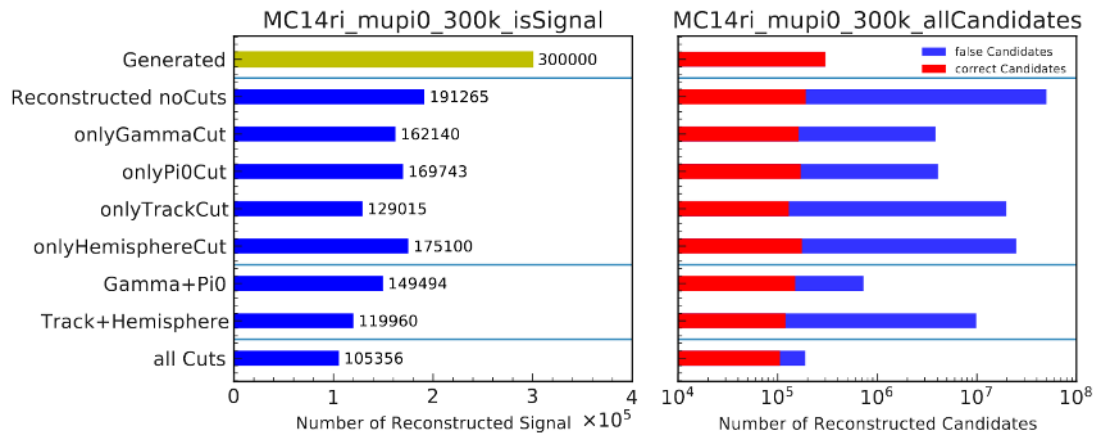


Figure 4.6: Number of correctly reconstructed signal events depending on what cuts are made and compared with amount of false candidates on the left and right plot respectively.

4.5 Signal and Background Samples

The signal and background samples used in this analysis are from the fourteenth Belle II MC-campaign *MC14_{ri}_a*, which simulates run-independent (ri) e^+e^- collisions with nominal background conditions (BGx1). The CM energy equals the $\Upsilon(4S)$ resonance, the basf2 software version used for creating the data is release 05-02-00.

4.5.1 Signal Kinematics

The goal of a cut-based analysis is to find variables, that can be used to separate our signal from other decays. To achieve this, a good knowledge about the kinematics of the signal is essential. An overview of relevant variables plotted is depicted in fig. 4.7, 4.8, 4.9 and also in the Appendix A.

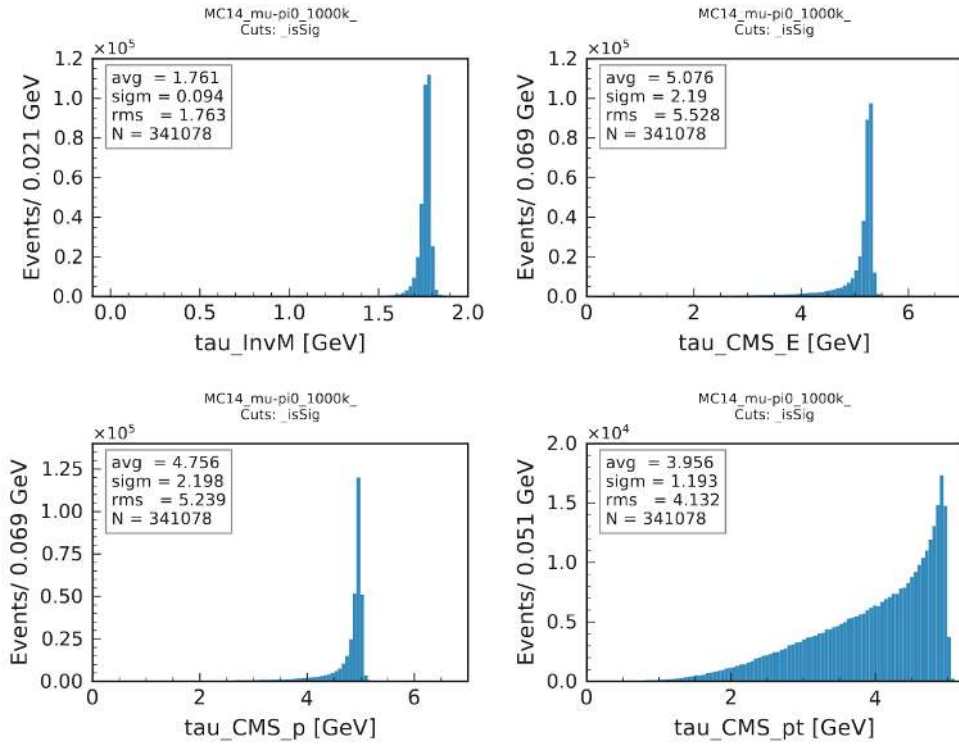


Figure 4.7: Invariant mass, energy, momentum and transverse momentum in the CMS of the reconstructed signal τ in the signal sample.

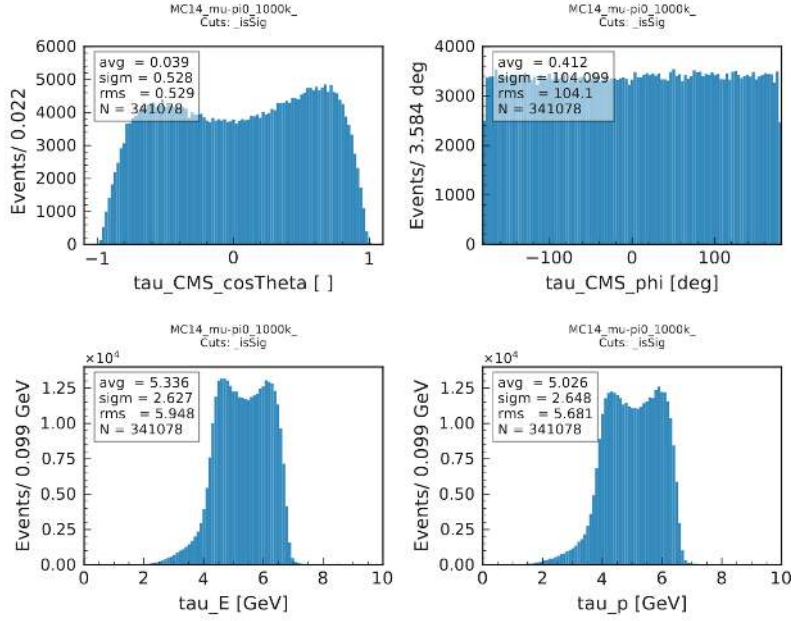


Figure 4.8: Polar and azimuth angle distribution in the CMS, aswell as the energy and momentum in the laboratory frame of the reconstructed signal τ in the signal sample.

The first two kinematic properties we investigate is the full reconstruction and the two-body decay of the signal τ . These two properties are not directly linked to each other and thus are a suitable starting approach. Cutting on these variables simultaneously means requiring our signal τ to decay into two particles, of which neither is a neutrino or decays further into one. When created in the IP, each of the two particles should carry the same energy as one of the incoming e^+ or e^- beam, when looking at them in the CMS. So when we claim, that our signal τ is fully reconstructed by $\tau \rightarrow \mu \pi^0$, its energy $E^{\text{CMS}}(\tau)$ should be close or equal the energy of the incoming beam $E_{\text{beam}}^{\text{CMS}}$ in the CMS. The missing difference we call ΔE and is therefore expressed as

$$\Delta E = E^{\text{CMS}}(\tau) - E_{\text{beam}}^{\text{CMS}}. \quad (4.2)$$

Next, we know that, when a resting particle decays through a two-body decay, the two final state particles need to have opposite momentum due to momentum conservation. This means, when looking at the decay daughters of our signal in the restframe of the reconstructed τ , the momenta need to peak around a certain value, which is constrained through the masses of the involved particles. As we can see

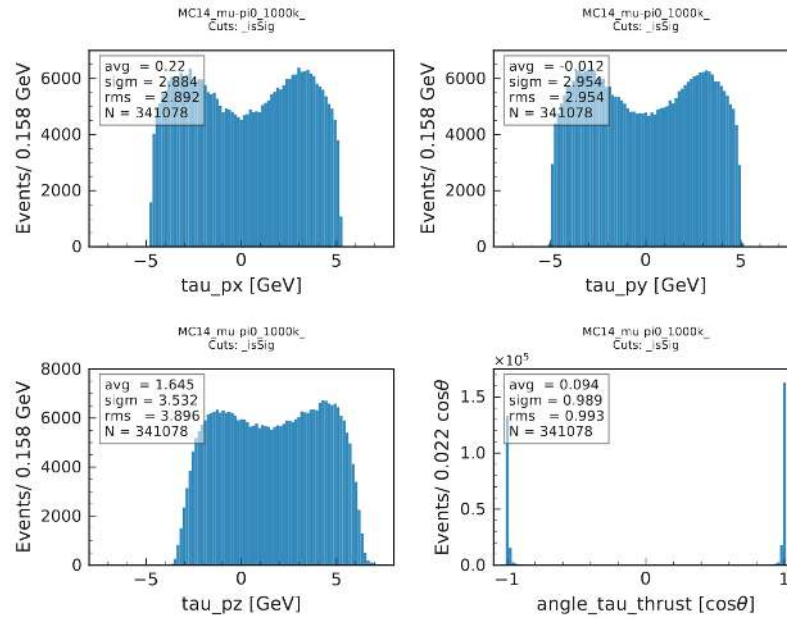


Figure 4.9: Distribution of the three momentum components in the laboratory frame of the reconstructed signal τ in the signal sample. The lower right plot shows the cosine of the angle between the τ and the thrust axis.

on the right side of fig. 4.10, the muon momentum $|\vec{p}_{\text{muon}}^{\text{RF}}|$ peaks close to 0.9 GeV. On the left side of the same figure we see ΔE peaking close to zero. Plotting these two variables against each other in a 2D-plot, we see that the signal in fig. 4.11 is strongly concentrated in the area marked by the red rectangle, which we define as the signal region.

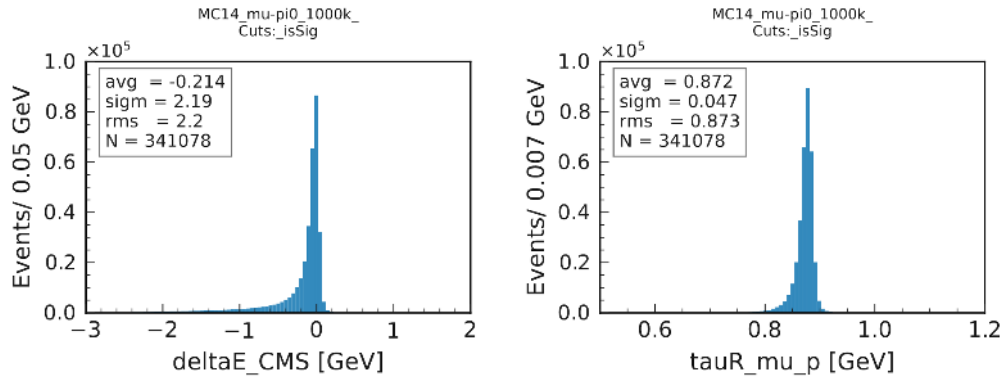


Figure 4.10: Distribution ΔE and muon momentum in the τ restframe in the signal sample.

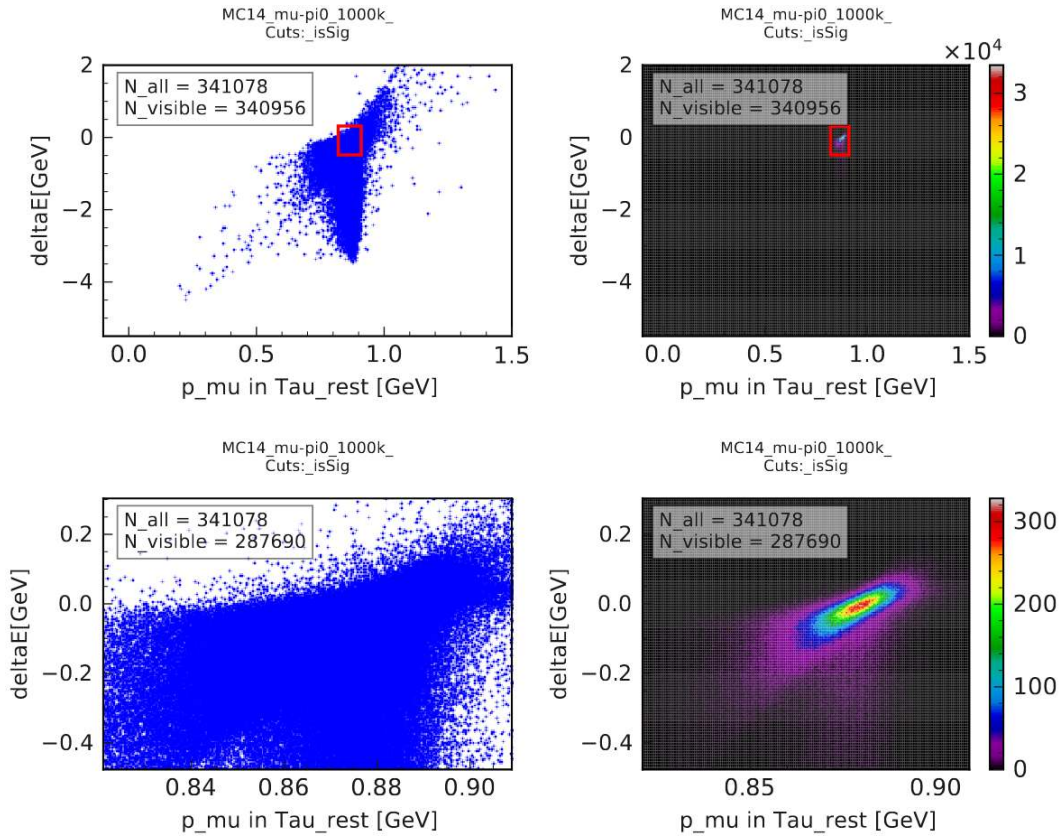


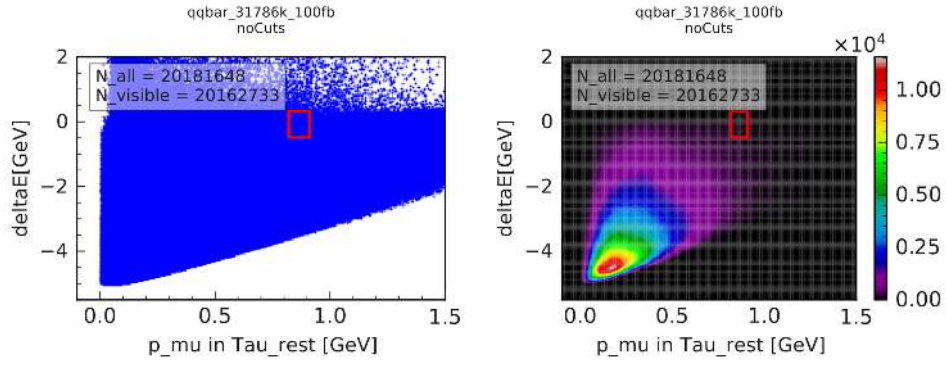
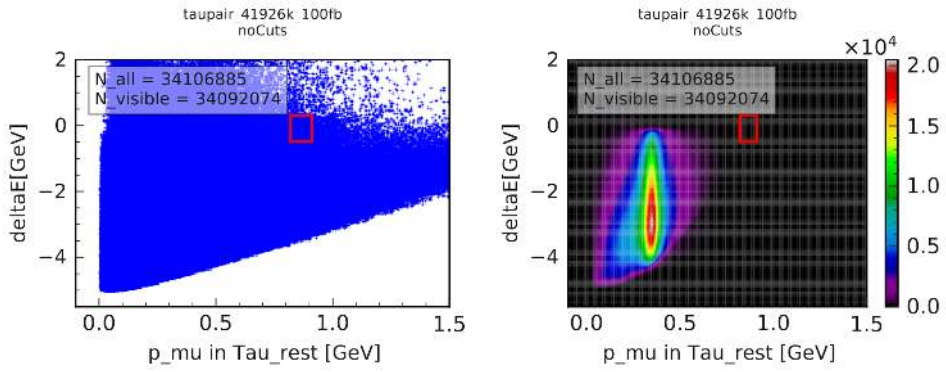
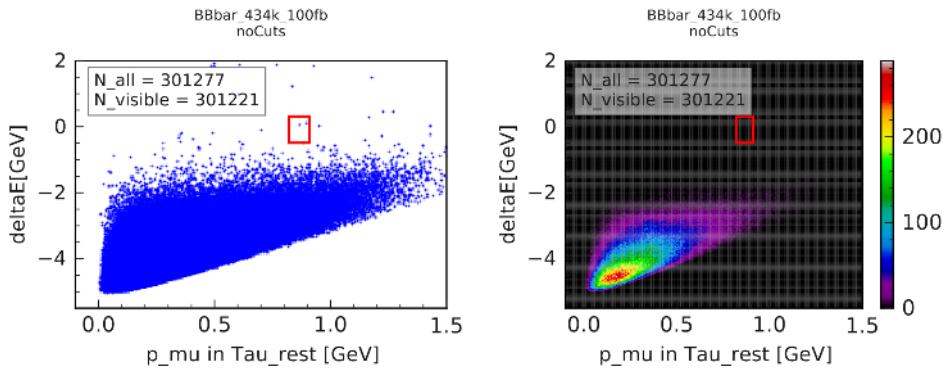
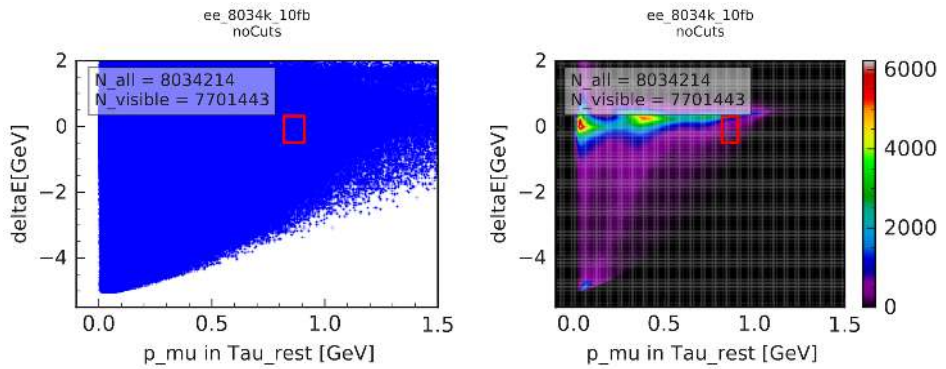
Figure 4.11: 2D distributions of ΔE versus muon momentum in the τ restframe. The red rectangle in the two upper graphics mark the zoom-in area depicted by the two lower graphics.

4.5.2 Background Kinematics

With a signal region defined, we can take a first look at the contribution of each BG event type in this particular area. When working with real data, one only sees the sum of all background and signal. When working with MC data however, the background contributions can be inspected separately. With this, cuts can be chosen to target certain backgrounds specifically. An overview of analysed background events and their respective cross section in the detector can be seen in Tab. 4.4. The sample sizes are simulated according to certain total luminosities. For the samples of processes with high cross sections a smaller luminosity of 10 fb^{-1} is chosen in order to keep file sizes manageable. For most processes we have samples equivalent to 100 fb^{-1} , which is sufficient to study the impact of applied cuts. For the background types, that are difficult to discriminate from signal, a larger sample is necessary in order to exclude effects caused by low statistics. Therefore later a larger sample is used for 'mumu'-events. Due to limited MC data, the analysis for all other samples in this thesis is restricted to 100 fb^{-1} . Fig. 4.12 shows the 2D distribution of the different BG samples after preselection. We see a big variance in the distributions of where the events of the BG are accumulated.

Process	Cross Section [nb]	Sample Name	L_{int} [fb^{-1}] analysed
$e^+e^- \rightarrow q\bar{q}$ ($q = u d s c$)	3.72	'qqbar'	100
$e^+e^- \rightarrow \tau^+\tau^-$	0.919	'taupair'	100
$e^+e^- \rightarrow B\bar{B}$	1.05	'BBbar'	100
$e^+e^- \rightarrow e^+e^-\gamma$	294	'ee'	10
$e^+e^- \rightarrow \mu^+\mu^-\gamma$	1.15	'mumu'	500
$e^+e^- \rightarrow e^+e^-\mu^+\mu^-$	18.9	'eemumu'	100
$e^+e^- \rightarrow e^+e^-e^+e^-$	39.7	'eeee'	10

Table 4.4: MC14 samples with corresponding cross section and luminosity.

(a) $q\bar{q}$ sample(b) Generic $\tau^+\tau^-$ sample(c) $B\bar{B}$ sample(d) $e^+e^-\gamma$ sample

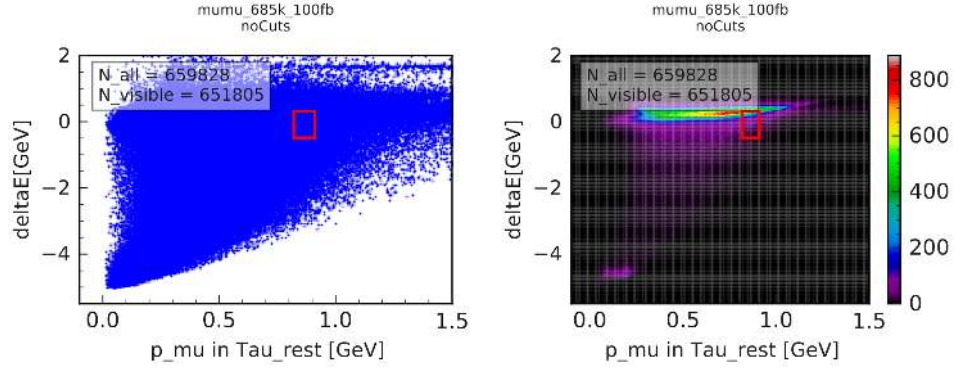
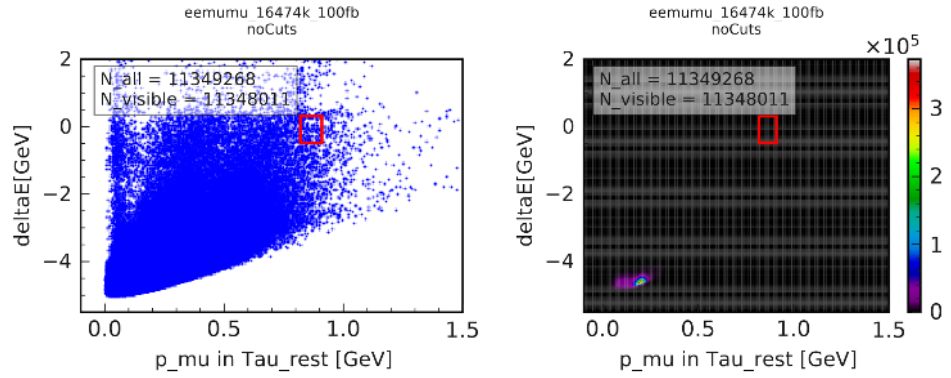
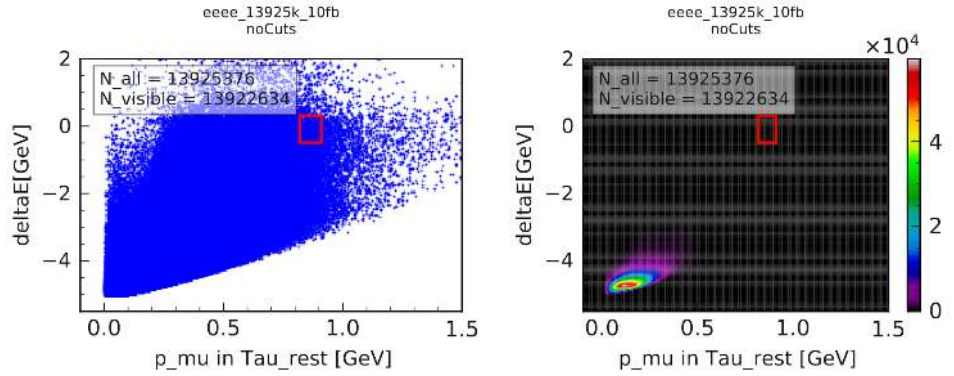
(e) $\mu^+ \mu^- \gamma$ sample(f) $e^+ e^- \mu^+ \mu^-$ sample(g) $e^+ e^- e^+ e^-$ sample

Figure 4.12: 2D correlations of muon momentum $|\vec{p}_{\text{muon}}^{\tau\text{RF}}|$ in the tau restframe and ΔE for all considered background samples. The red square marks the signal region, where 90% of the signal is allocated. The left column shows a scatter plot of the events, the right column shows the distribution density by color.

4.6 2D Cut on ΔE and $|\vec{p}_{\text{muon}}^{\tau RF}|$

For the first cut, we will set for simplicity a trapezoidal cut inside the signal region around the peak, so that still approximately $\sim 68\%$ of the signal pass the preselection. The cut trapezoid is given the abbreviation "1 σ " and is defined through:

- $|\vec{p}_{\text{muon}}^{\tau RF}| > 0.85 \text{ GeV}$
- $|\vec{p}_{\text{muon}}^{\tau RF}| < 0.90 \text{ GeV}$
- $4.4 \cdot |\vec{p}_{\text{muon}}^{\tau RF}| - 3.78 \text{ GeV} < \Delta E \text{ [GeV]}$
- $6.8 \cdot |\vec{p}_{\text{muon}}^{\tau RF}| - 6.08 \text{ GeV} > \Delta E \text{ [GeV]}$

With this cut, our focus is on eliminating BG events, that decay into a final state with more than two particles, when considering the reconstructed π^0 as one final state particle. In these events, even if all final state particles are visible and recorded in the detector, by reconstructing according to $\tau \rightarrow \mu \pi^0$, the reconstructed ' τ ' does then not contain all the energy of the initial signal particle. This results in ΔE being further away from zero and thus most of these events are excluded by the cut. This effect is especially prominent in the case of B -mesons (see fig. 4.13d), which usually decays into a large number of final state particles, and thus ΔE is far away from zero. In addition, this cut excludes most of three-body decay event types, which usually have a broad momentum distribution in the restframe of the mother particles. Since we are cutting on only a small window of this distribution, naturally some events are located inside, but most events are excluded. While the amount of BG events is drastically reduced to 0.01%, about two thirds of the signal events remain. BG types with similar kinematics to $\tau \rightarrow \mu \pi^0$, such as $\mu^+ \mu^- \gamma$, $e^+ e^- \gamma$ or $q\bar{q}$ still remain in significantly higher numbers than the other event types.

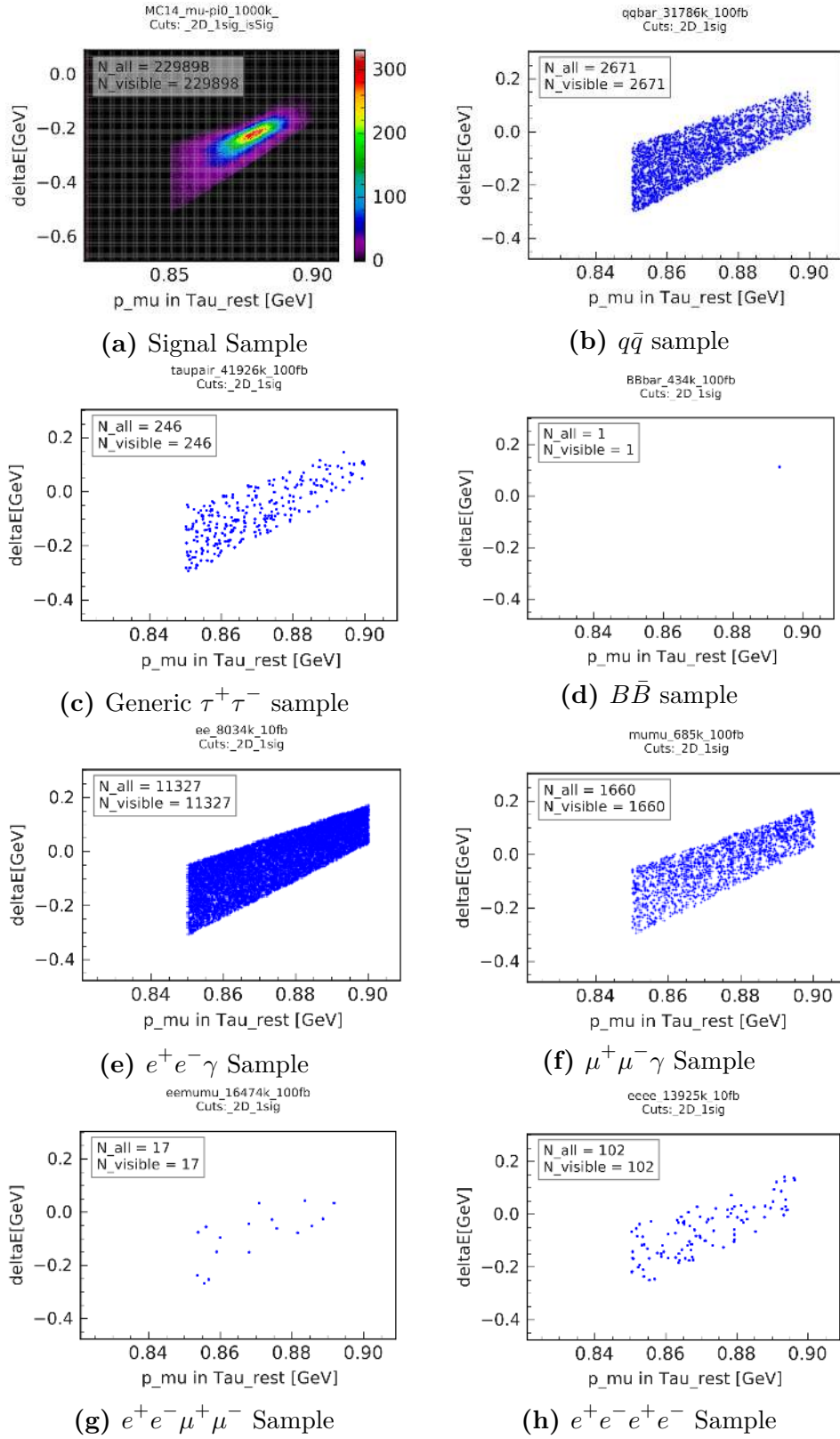


Figure 4.13: 2D Distributions of signal and BG samples after cutting on 1σ area around signal peak in the signal area.

4.7 Cut on Muon ID

Until now, we only required our μ in the reconstruction to be a charged track within certain momentum range, while it could be still an electron, charged pion, or kaon instead. For this issue, Belle II has implemented a Particle Identification (PID), which assigns an identity probability to each charged particle. The PID is a high-level variable, where information from the ECL, KLM, CDC and the cherenkov detectors is combined into a likelihood for each possible particle type. This likelihood is expressed in a variable, such as 'muonID' or 'electronID', which is a number between 0 and 1. The closer to 1, the more likely the measured particles is in fact a muon or electron. Since we want to make sure, we use a muon for our reconstruction, we cut on the variable 'muID', whose distribution for each event type can be found in Appendix A. The physics performance group at Belle II regularly tests and improves the performance of the PID on real data with certain ID-thresholds. We will use these thresholds of 0.50, 0.90, 0.95 and in addition 0.99 to test, how signal and background are influenced through these cuts. Tab. 4.5 lists the number of candidates remaining in each event type depending on the threshold for the PID cut. As we expected, already a low muID requirement results in a major decrease in events without any muons in the final state, such as $e^+e^-\gamma$ or $e^+e^-e^+e^-$ events. The backgrounds $q\bar{q}$, generic $\tau^+\tau^-$ or $e^+e^-\mu^+\mu^-$, which all allow muons in the final state, are reduced mostly to events containing a real muon. Therefore increasing the muon threshold further only has small impact. The same is true for all events in the $\mu^+\mu^-\gamma$ sample, where the muon-ID has very little impact. For the signal sample, we see a reduction in events with stronger cuts, from losing only 11 000 events at $\text{muID} > 0.5$, up to 28 000 events at $\text{muID} > 0.99$. Since higher threshold values only have a minor impact, we choose a moderate $\text{muID} > 0.9$ cut for the time being, which keeps 91 % of the remaining signal.

	signal	$q\bar{q}$	$\tau^+\tau^-$	$B\bar{B}$	$e^+e^-\gamma$	$\mu^+\mu^-\gamma$	$e^+e^-\mu^+\mu^-$	$e^+e^-e^+e^-$
no cuts	341078	20181648	34106885	301277	8034214	659828	11349268	13925376
2D cut	229898	2671	246	1	11328	1660	17	102
muID > 0.50	218758	218	32	0	16	1579	4	2
muID > 0.90	208222	119	26	0	2	1547	4	0
muID > 0.95	206202	109	25	0	1	1537	4	0
muID > 0.99	201679	97	22	0	0	1506	4	0

Table 4.5: Number of events in all samples for different muon ID cuts.

4.8 Cut on Visible Energy

A cut on the visible energy exploits the fact, that the other τ , which is pair-produced with our signal, decays according to the SM. This τ , also called tag- τ , always decays into a final state with at least one neutrino. This means, that there is always the undetected energy of the neutrino, which means the total visible energy of the event in average has to be smaller than the initial CM energy. This makes the visible energy a suitable variable to distinguish signal from background events that do not contain a neutrino in the final state. The distribution of the visible energy in the CMS, as seen in fig. 4.14, shows a peak above 10 GeV for the $q\bar{q}$ - and $\mu^+\mu^-\gamma$ samples. For the signal sample (see fig. 4.14a), most events have a visible energy between 5.3 GeV and 11 GeV. We also see the distribution falling off quickly above 10 GeV, so implementing a cut there seems feasible, even if around 28 000 signal events get lost in the process, which is a 14 % loss of the remaining signal. Notice, that here the $100 \text{ fb}^{-1} \mu^+\mu^-\gamma$ sample has been replaced by the 500 fb^{-1} for better statistics. The results of this cut show, that at this stage all background candidates of the $B\bar{B}$, $e^+e^-\gamma$ and $e^+e^-e^+e^-$ are rejected. The two latter samples correspond to a smaller luminosity of 10 fb^{-1} . However, having these backgrounds eliminated at this early stage of non-BG-specific cuts it makes it reasonable to assume, that these event types cause no significant background at larger samples sizes. Furthermore, upcoming cuts would further decrease possible candidates.

	signal	$q\bar{q}$	$\tau^+\tau^-$	$B\bar{B}$	$e^+e^-\gamma$	$\mu^+\mu^-\gamma$	$e^+e^-\mu^+\mu^-$	$e^+e^-e^+e^-$
no cuts	341078	20181648	34106885	301277	8034214	659828	11349268	13925376
2D cut	229898	2671	246	1	11328	1660	17	102
muID >0.90	208222	119	26	0	2	1547	4	0
E_{visible}	179867	30	20	0	0	1031	3	0

Table 4.6: Cutflow for remaining events in signal and BG samples. In the last cut, the $\mu^+\mu^-\gamma$ sample is replaced by a sample 5 times bigger.

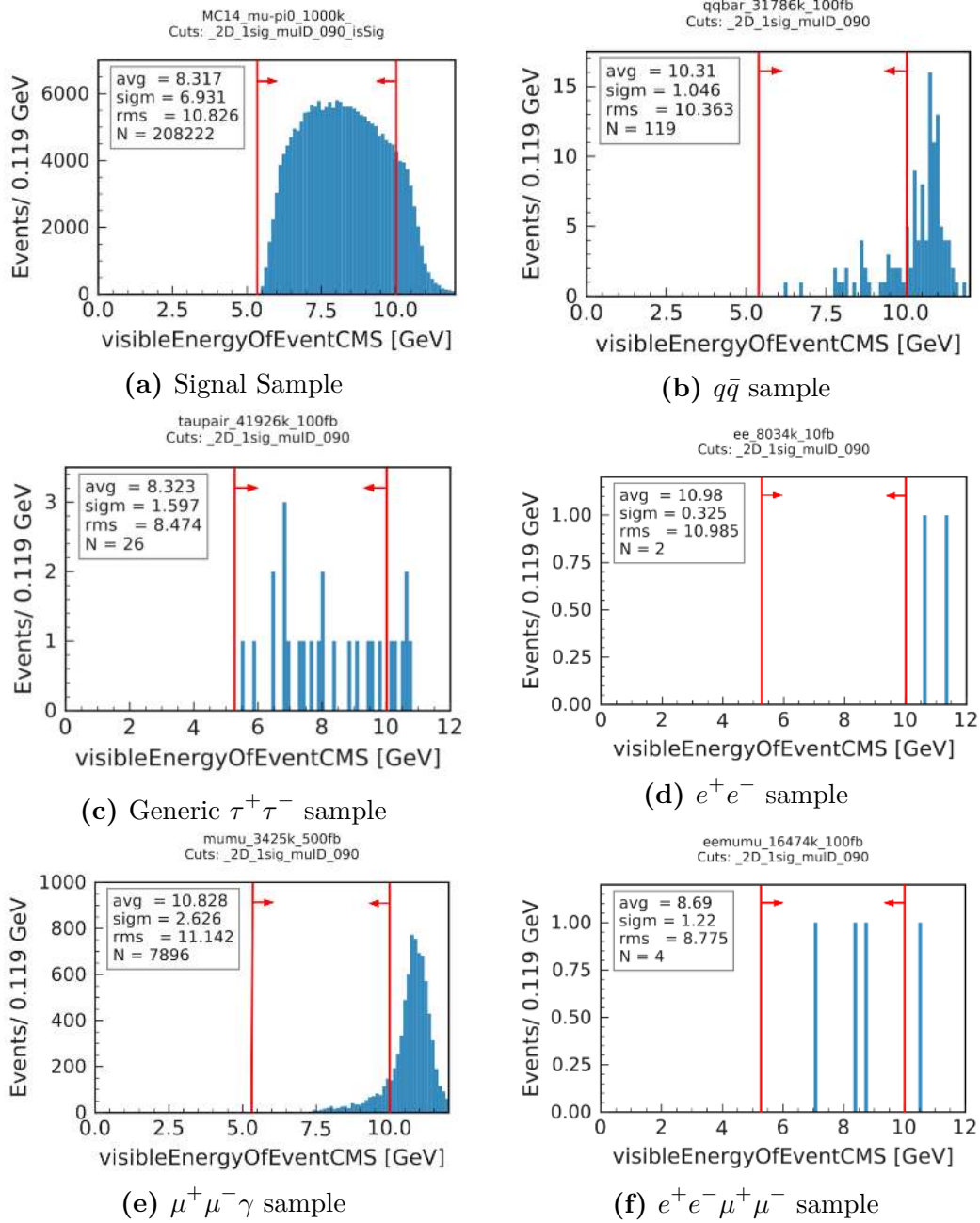


Figure 4.14: Distribution of the visible energy for signal and BG samples. The red vertical lines indicate the applied cuts.

4.9 Cut on Polar Angle of Missing Momentum

This cut aims to reduce the $\mu^+\mu^-\gamma$ background by again utilizing the fact, that we have at least one neutrino in the final state of our signal. By taking the combined momentum of the incoming e^+e^- beams in the laboratory frame and then subtracting the momentum of all detected particles, we acquire the magnitude and direction of the missing momentum in the event. If this missing momentum is caused by an undetectable neutrino, we expect the missing energy to point in its direction, which should be uniformly distributed in all directions. The other possible source for missing momentum is, if one or more particles are emitted in shallow polar angles outside of the CDC acceptance range and thus cannot be detected. In $\mu^+\mu^-\gamma$ events most of the time all final state particles are reconstructed, so the missing momentum is likely to point into the direction of the initial state radiation, which is strongly collimated in the forward-backward directions, i.e disappears undetected in the beam pipe. We observe the difference in distributions of the polar angle in fig. 4.15. The distribution for the signal 4.15a is rather broad, and in contrast the muon-sample shown in fig. 4.15d peaks at large and small angles. Using this information, we eliminate the remaining $e^+e^-\mu^+\mu^-$ and most of the $\mu^+\mu^-\gamma$ BG by requiring the polar angle of the missing momentum to be in the range from 23° to 140° , while only losing about 6% of the remaining signal.

	signal	$q\bar{q}$	$\tau^+\tau^-$	$B\bar{B}$	$e^+e^-\gamma$	$\mu^+\mu^-\gamma$	$e^+e^-\mu^+\mu^-$	$e^+e^-e^+e^-$
no cuts	341078	20181648	34106885	301277	8034214	659828	11349268	13925376
2D cut	229898	2671	246	1	11328	1660	17	102
muID >0.90	208222	119	26	0	2	1547	4	0
E_{visible}	179867	30	20	0	0	1031	3	0
$\theta_{\text{missing } \vec{p}}$	168372	26	19	0	0	41	0	0

Table 4.7: Cutflow for remaining events in signal and BG samples.

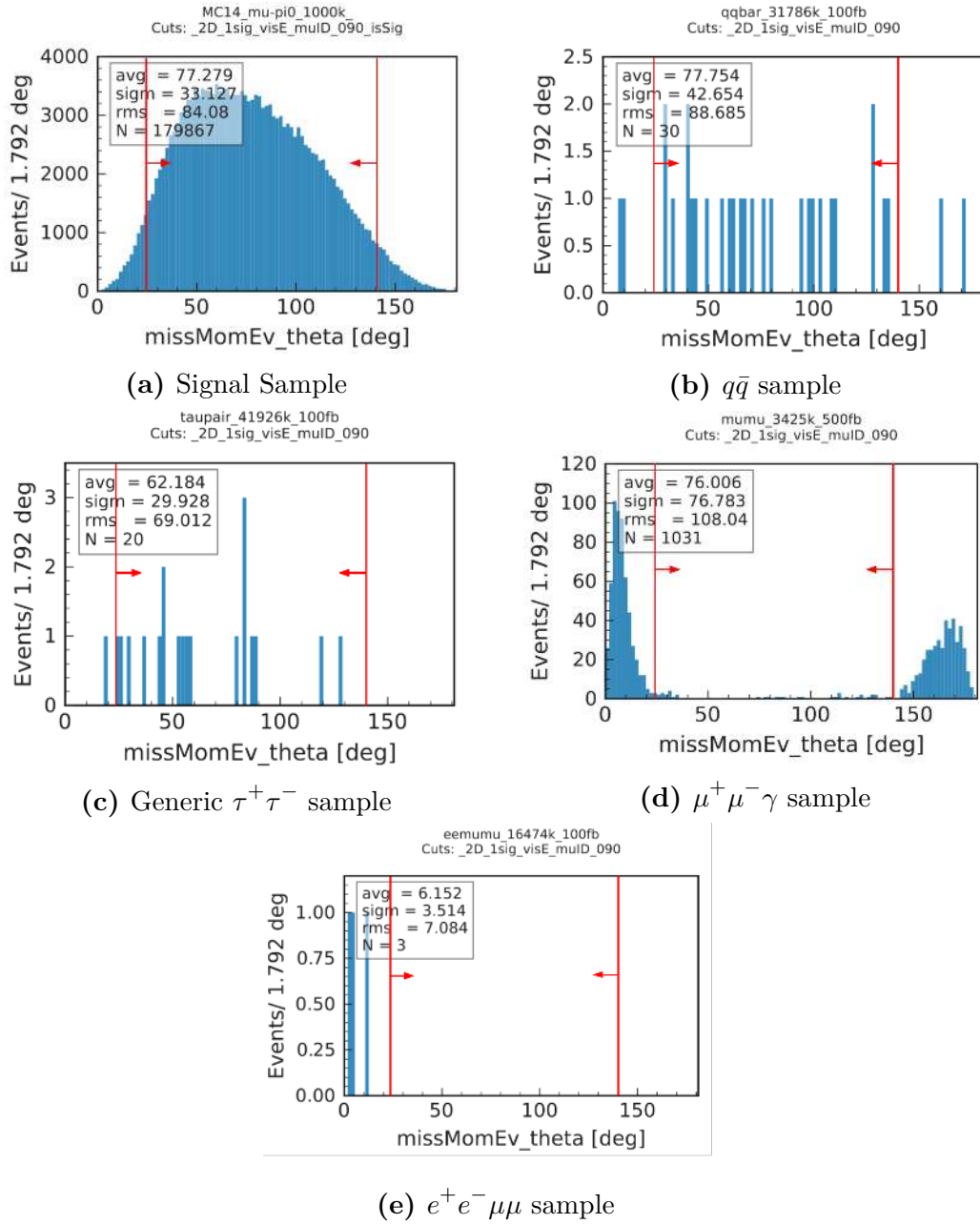


Figure 4.15: Distribution of the polar angle θ of the direction of the missing momentum of an event for signal and BG samples. The red vertical lines indicate the applied cuts.

4.10 Cut on Opening Angle between μ and π^0 in CMS

This cut focuses on the opening angle between the two daughter particles of the reconstructed τ in the CMS. It is not focusing on a specific background, but just uses the signal kinematics to further reduce BG in general. For our signal, the cosine of the opening angle peaks around 0.8 (see fig. 4.16a). Due to the two-body nature of this decay, the events with broader opening angles fall off rather quickly, which makes a cut requiring $\cos\theta$ between 0.5 and 0.8 feasible. With this we only loose 7% of the remaining signal events, while reducing the remaining background by almost 80% to only 19 events.

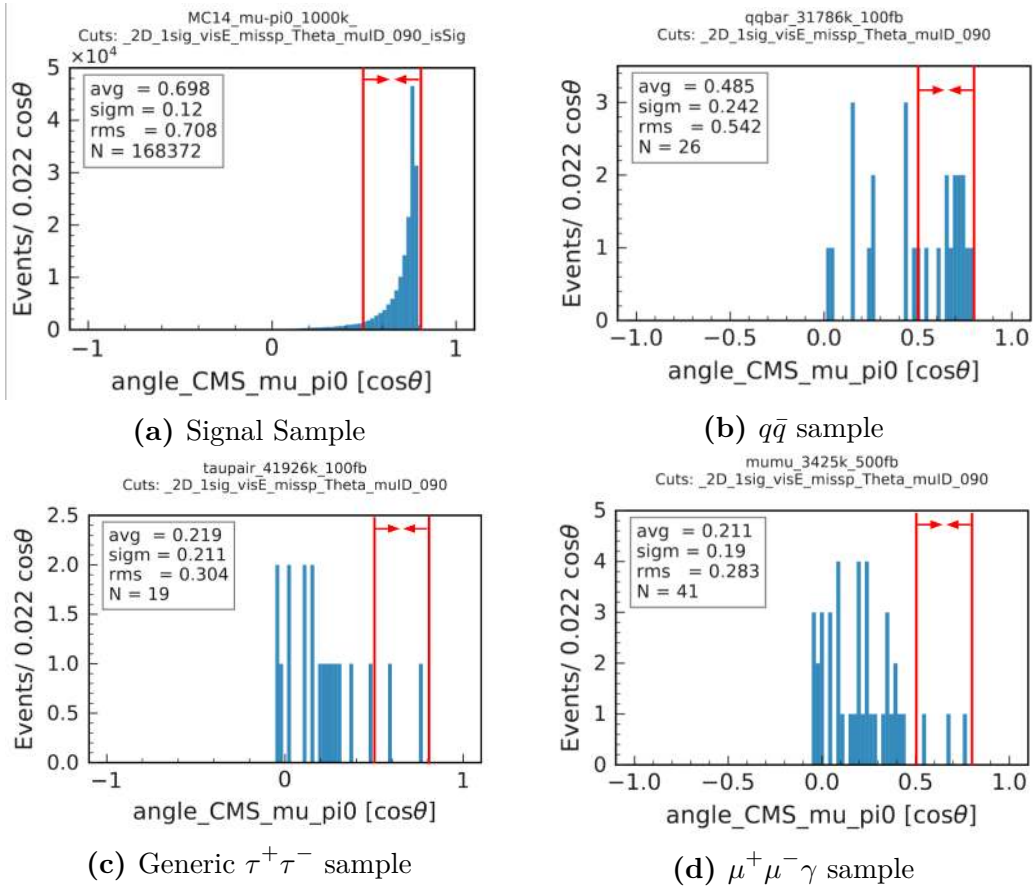


Figure 4.16: Distribution of the opening angle between the muon and the reconstructed π^0 of signal and BG samples. The red vertical lines indicate the applied cuts.

	signal	$q\bar{q}$	$\tau^+\tau^-$	$B\bar{B}$	$e^+e^-\gamma$	$\mu^+\mu^-\gamma$	$e^+e^-\mu^+\mu^-$	$e^+e^-e^+e^-$
no cuts	341078	20181648	34106885	301277	8034214	659828	11349268	13925376
2D cut	229898	2671	246	1	11328	1660	17	102
muID >0.90	208222	119	26	0	2	1547	4	0
E_{visible}	179867	30	20	0	0	1031	3	0
$\theta_{\text{missing } \vec{p}}$	168372	26	19	0	0	41	0	0
$\mathcal{L}(\mu\pi^0)_{\text{CMS}}$	156615	14	2	0	0	3	0	0

Table 4.8: Cutflow for remaining events in signal and BG samples.

4.11 Cut on Tighter Signal Region

The goal of the final cut is to remove all of the remaining background to zero. This is achieved by tightening the trapezoidal cut (see sect. 4.6) on the signal region around the peak even further:

- $|\vec{p}_{\text{muon}}^{\tau\text{RF}}| > 0.872 \text{ GeV}$
- $|\vec{p}_{\text{muon}}^{\tau\text{RF}}| < 0.886 \text{ GeV}$
- $5.5 \cdot |\vec{p}_{\text{muon}}^{\tau\text{RF}}| - 4.86 \text{ GeV} < \Delta E \text{ [GeV]}$
- $4.4 \cdot |\vec{p}_{\text{muon}}^{\tau\text{RF}}| - 3.85 \text{ GeV} > \Delta E \text{ [GeV]}$

As shown in fig. 4.17, all the remaining BG events lie located outside of this cut. We notice, that in the qqbar sample events are located closely around the cut region, so it would be likely, that with a larger sample eventually some of the events would still remain. Tab. 4.9 shows, how much events of the signal and the BG remain after each step, until the BG is fully suppressed. With this cut we reduce the remaining signal by roughly two thirds to 5.35% of the initially generated signal. This number is our final sensitivity on the signal. The value is similar to the ones reached by the Belle (4.5%) and BaBar (4.8%) experiments.

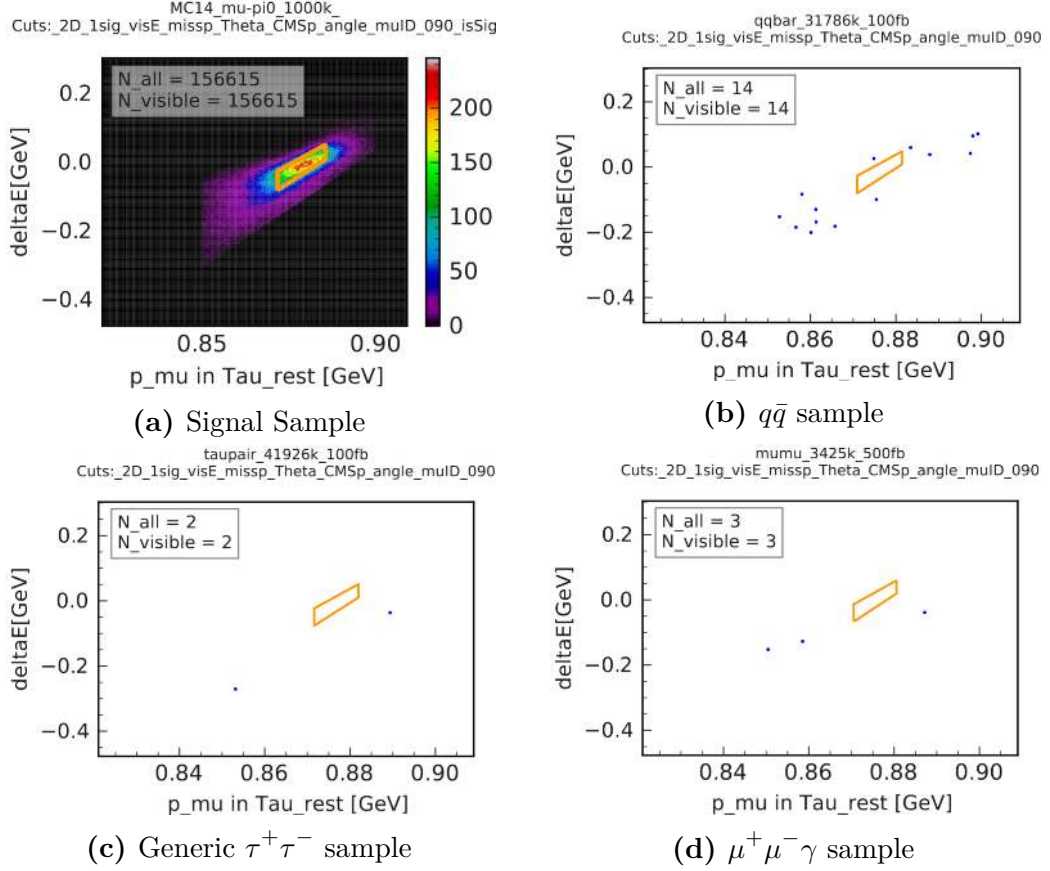


Figure 4.17: Distribution of signal and BG samples in the 2D signal area before the final cut marked by the red region.

	signal	$q\bar{q}$	$\tau^+\tau^-$	$B\bar{B}$	$e^+e^-\gamma$	$\mu^+\mu^-\gamma$	$e^+e^-\mu^+\mu^-$	$e^+e^-e^+e^-$
no cuts	341078	20181648	34106885	301277	8034214	659828	11349268	13925376
2D cut	229898	2671	246	1	11328	1660	17	102
muID > 0.90	208222	119	26	0	2	1547	4	0
E_{visible}	179867	30	20	0	0	1031	3	0
$\theta_{\text{missing } \vec{p}}$	168372	26	19	0	0	41	0	0
$\angle(\mu\pi^0)_{\text{CMS}}$	156615	14	2	0	0	3	0	0
tight 2D cut	53489	0	0	0	0	0	0	0

Table 4.9: Final cutflow for remaining events in signal and BG samples. The first few cuts were to eliminate BG events fundamentally different from our signal. The remaining BG was mainly $q\bar{q}$, generic $\tau^+\tau^-$ and $\mu^+\mu^-\gamma$, on which the cuts after were focusing on. The $\mu^+\mu^-\gamma$ BG could be well suppressed through the cut on the polar angle of the missing momentum and on the missing energy. The few remaining $\tau^+\tau^-$ events could be reduced by cutting on the opening angle, before the last BG events could be fully eliminated by tightening the 2D-cut.

4.12 Summary and Upper Limit Prediction

We have managed to suppress all BG candidates in a sample of equivalent to 100 fb^{-1} , and in the case of the muon-pair sample even 500 fb^{-1} , while still maintaining a sensitivity of 5.35% on the signal. Of the reconstructed particles of the signal sample only 14 events, i.e. 0.03%, did not belong to an actual signal, which is a well manageable error on the sensitivity.

Comparing this with the results of previous experiments, BaBar had an efficiency of $4.75 \pm 0.37\%$ and an expected BG of 1.33 ± 0.15 events, whereas Belle had a signal efficiency of 4.53% and an expected BG of 0.64 ± 0.32 events. Belle holds the current upper limit for the branching fraction of $2.7 \cdot 10^{-8}$ at 90% Confidence Level (CL) as a result of analysing 901 fb^{-1} of data. We can use a Bayesian approach to calculate an estimation for an upper limit according to our results. Appendix B describes the calculation and fig. 4.18 shows the resulting Probability Distribution Function (PDF), when we would assume to find zero events in the actual data. With this distribution, we can deduce an upper limit of $5.7 \cdot 10^{-7}$ in a 90% Credible Interval (CI) and $7.4 \cdot 10^{-7}$ in a 95% CI.

This is still one order of magnitude away to be competitive, but considering the fact, that Belle II will have a higher signal efficiency, less signal will be necessary to reach the results of Belle. If we take the increase in available signal through the STT into account, it is very likely to reach upper limits similar to Belle, as soon as Belle II will have collected data equaling a total luminosity of 500 fb^{-1} until the end of 2022. To further confirm our selection criteria, the upcoming step would be to inspect larger MC samples for all backgrounds types of at least 500 fb^{-1} . This will allow us to adapt the cuts to keep the BG suppressed at increased data size.

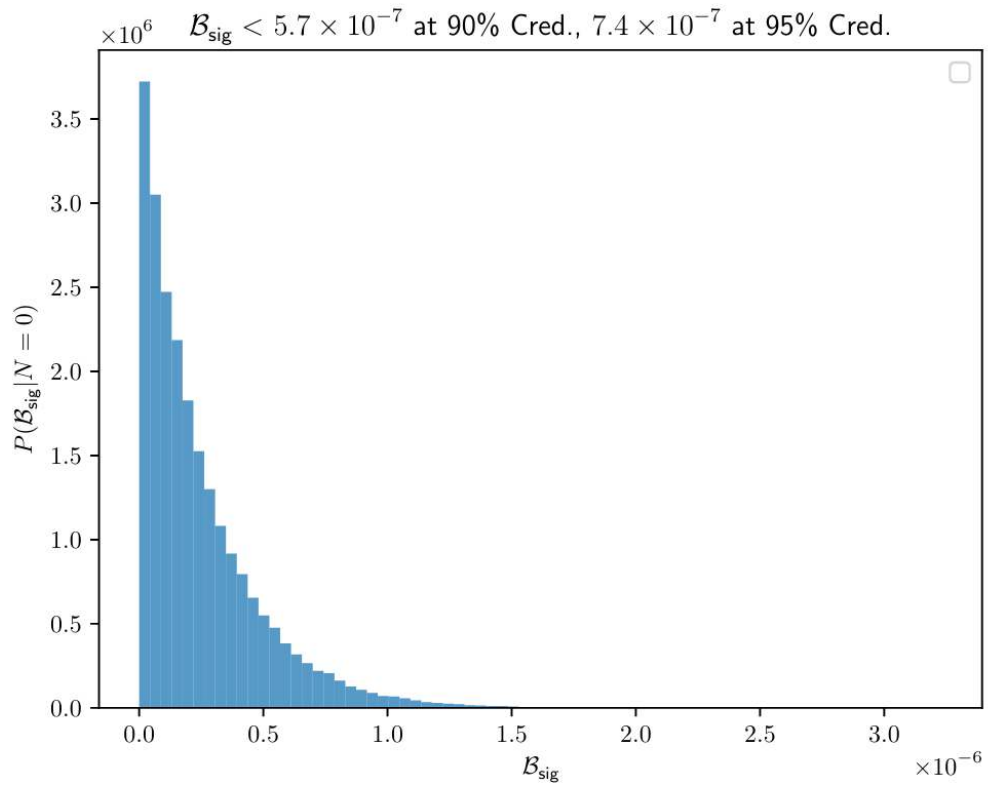


Figure 4.18: Probability Distribution Function for the branching fraction of $\tau \rightarrow \mu \pi^0$, when $N=0$ events in the data are assumed. [31]

5 Conclusion and Outlook

This analysis presented the first approach to the LFV decay $\tau \rightarrow \mu \pi^0$ at Belle II by investigating simulated MC samples.

This final state can occur in various NP models already at tree level, which increases the chances to be detected with a sufficiently large amount of data. Since τ leptons mostly decay into 1-Prongs and we chose to focus on 1-1 topologies first.

Next, looking at all the improvements made for Belle II compared to its predecessor, we got familiar with the different sub-detectors and their characteristics to get a good understanding of detector-specific effects affecting this analysis.

Before going into the analysis, we first checked the reconstruction efficiency of our detector in a smaller signal sample, where one τ decays according to our signal $\tau \rightarrow \mu \pi^0$, while the other τ according to the SM. Here we saw, that 64% of the generated events could be reconstructed by the detector along with many false candidates. Then, with the preselection requirements we reduced the number of false candidates drastically and required to only select two-track events after which we had 34% of the signal remaining.

The goal of our cuts is to suppress BG events, that mimic the signal, while maintaining a high enough sensitivity for actual signal events. The most prominent BG types for this analysis are $\mu^+ \mu^- \gamma$, $q\bar{q}$ and generic $\tau^+ \tau^-$.

In preparation for the set of cuts to eliminate the BG, we defined a signal area by plotting ΔE and the reconstructed charged particle's momentum in the restframe of the τ against each other. Comparing the signal with our 100 fb^{-1} BG samples we observed, that the sample containing $\mu^+ \mu^- \gamma$ events has the highest number of events in this area. After a trapezoid shape cut around our signal, we managed to reduce the amount of remaining events of the BG drastically, for some almost to zero. In the next cuts, we required the charged track to be muon and capped our visible energy in an event to exclude fully reconstructable final states. To further reduce the $\mu^+ \mu^- \gamma$ BG, we exclude all events, where the missing momentum of such points to low polar angles. We also limited the possible opening angle between the reconstructed μ and π^0 in the CMS-frame, after which the only types of BG events

remaining are $\mu^+\mu^-\gamma$, $q\bar{q}$ and the generic $\tau^+\tau^-$. To eliminate the remaining BG, we tightened our cut inside the signal area further, with the final result of a signal efficiency of 5.35% and a fully suppressed BG.

The next steps in the analysis of this decay channel would be to test out these cuts at a larger MC-sample of BG events. This way, we will be able to find out, if the background stays fully suppressed and can if necessary adapt our current cuts or add additional ones.

We can also replace our cut-based approach by a multivariate method, such as a Boosted Decision Tree (BDT) based approach [32]. This more modern methods allows us to exploit correlations between the cut-variables in order to achieve a combined optimum of all cuts, rather applying them separately by hand. By this, we will be able to suppress the BG consistently also at higher luminosities and will minimize losses in the signal, which will further increase the efficiency. This analysis can also be extended to cover similar final states, that can be created through the same NP processes, such as $\tau \rightarrow e\pi^0$, $\tau \rightarrow \ell\eta$ or $\tau \rightarrow \ell\eta'$.

By further increasing the efficiency of this decay, Belle II could be already competitive with the results of Belle with a significantly smaller dataset available. Belle II could collect as much as 500 fb^{-1} before the end of 2022, which is still far from the 901 fb^{-1} of its predecessor. But the results of this thesis show, that for Belle II might most likely be competitive already with half of the luminosity.

Appendix

A Analysis Plots

Detector Efficiency

These plots show different variables of the reconstructed τ lepton. Looking at the momentum distribution, we see a difference in shape, when comparing the generator level with the reconstruction. Peaks of the reconstruction of the momentum are less prominent, which is a consequence of missing photons and muons in the endcap CDC areas (see sect. 4.3).

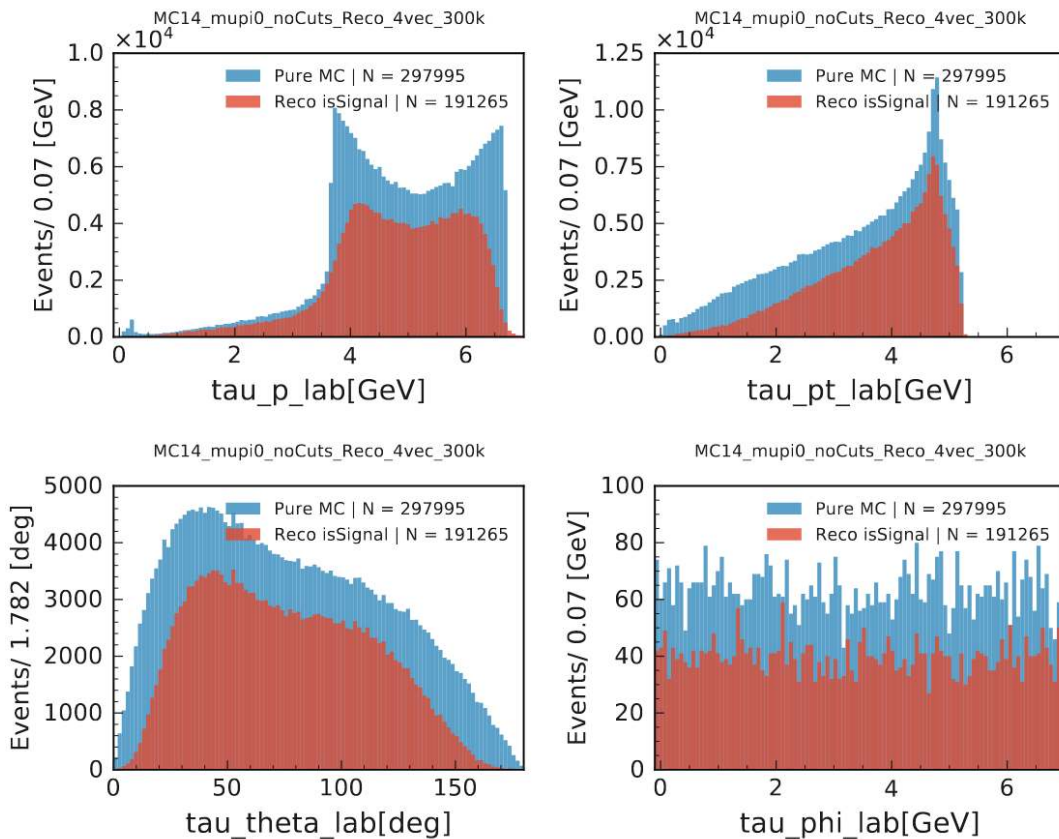


Figure A.1: Comparison of generator level MC distributions (blue) to by the detector correctly reconstructed tauons (red). The upper left plot shows the momentum, next to it is the transverse momentum. On the lower left we see the polar angle distribution and on the right the azimuth angle. All variables are in the laboratory frame.

Reconstructed Variables from Signal Sample (isSignal)

These figures show the distributions of different variables of the signal sample before the first cut with requiring the variable *isSignal* to be true, i.e. excluding wrong candidates for the signal τ . First, we have the cut-variables, followed by event variables and kinematic properties of the signal τ in the CMS and laboratory frame. Then, there are the same kinematic properties, but for the ROE, the μ and the π^0 . Finally, we see some miscellaneous variables, such as the difference in polar and azimuth angle between the signal τ and the ROE.

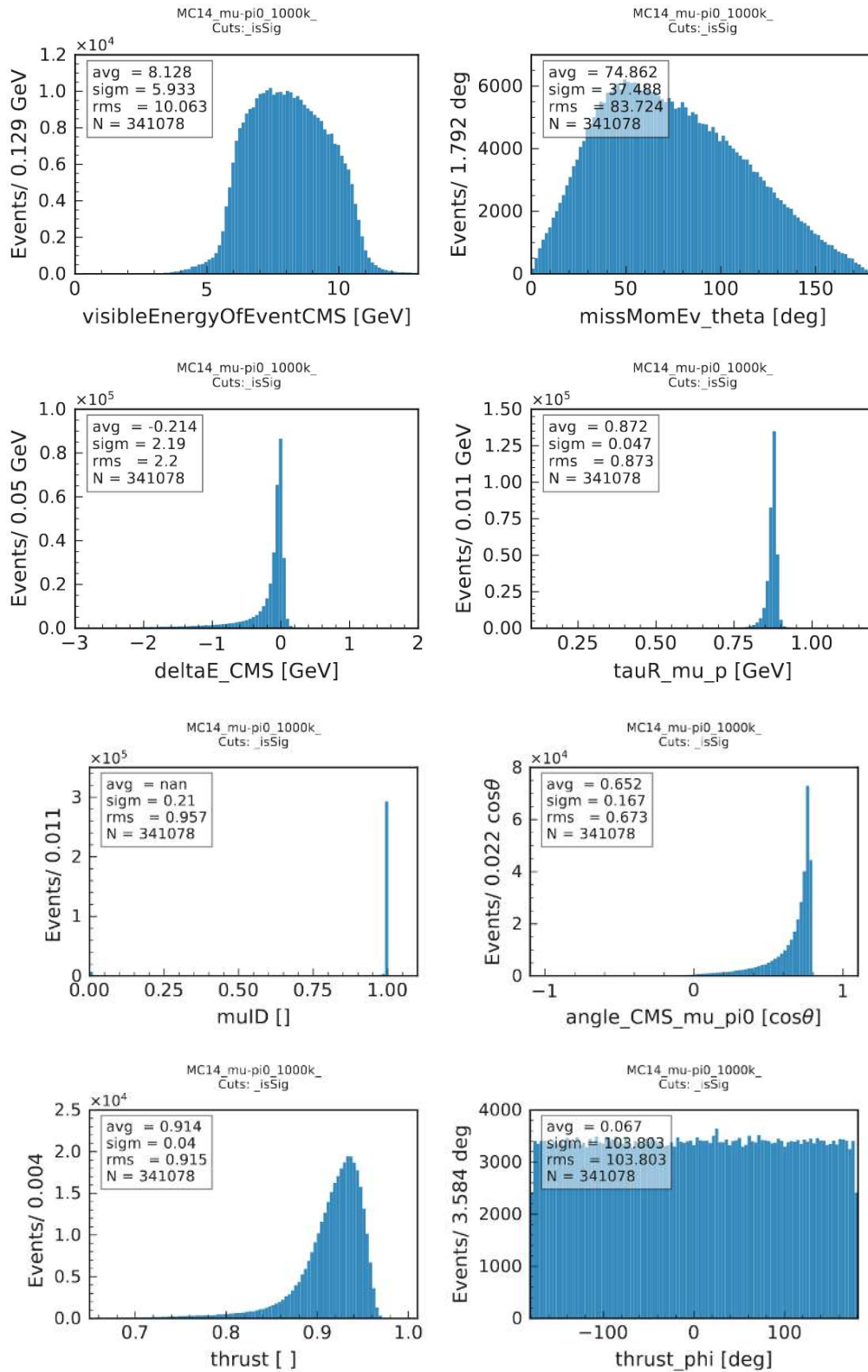


Figure A.2: Reconstructed variables from signal sample, isSignal.

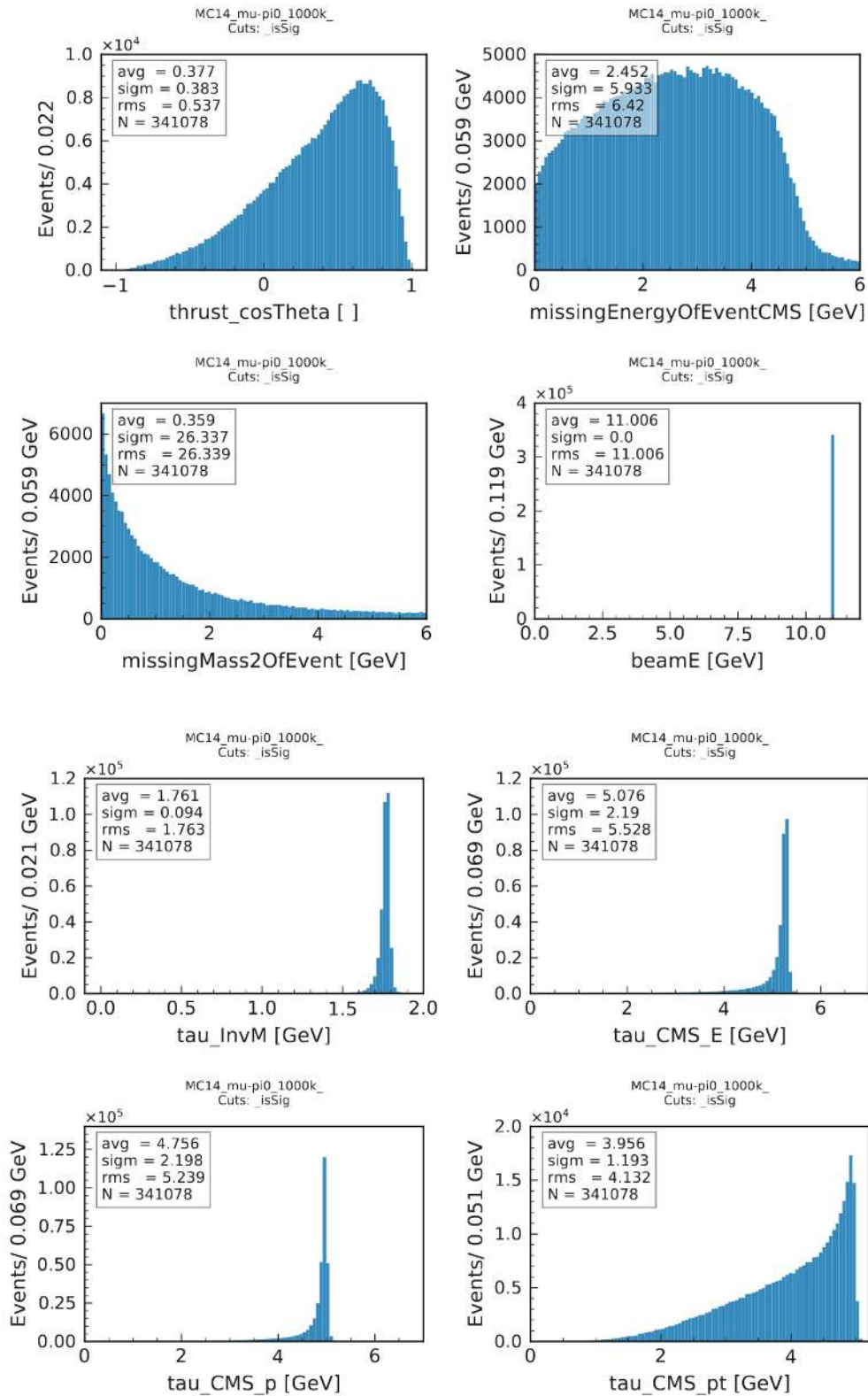


Figure A.2: Reconstructed variables from signal sample, isSignal.(cont.)

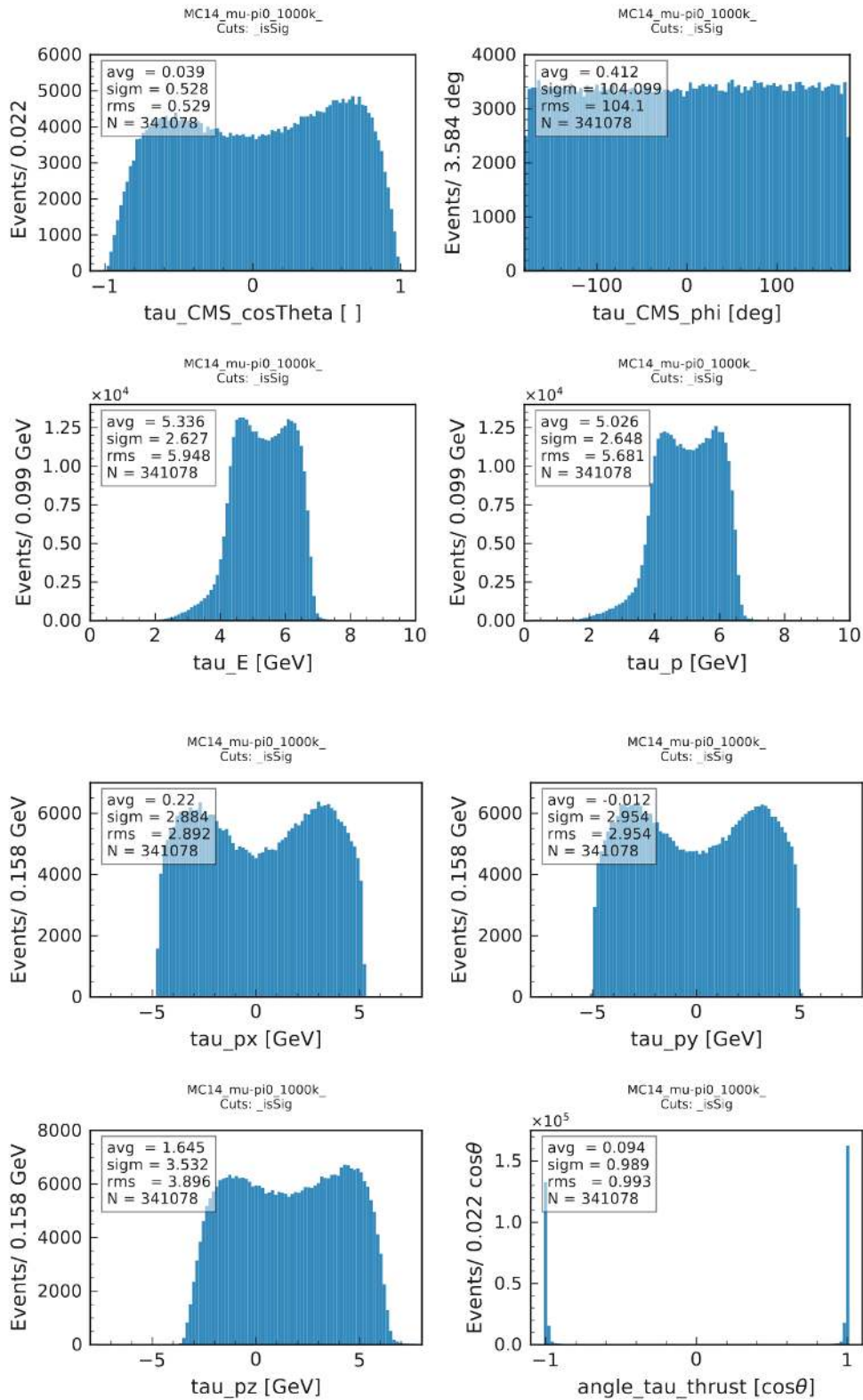


Figure A.2: Reconstructed variables from signal sample, isSignal.(cont.)

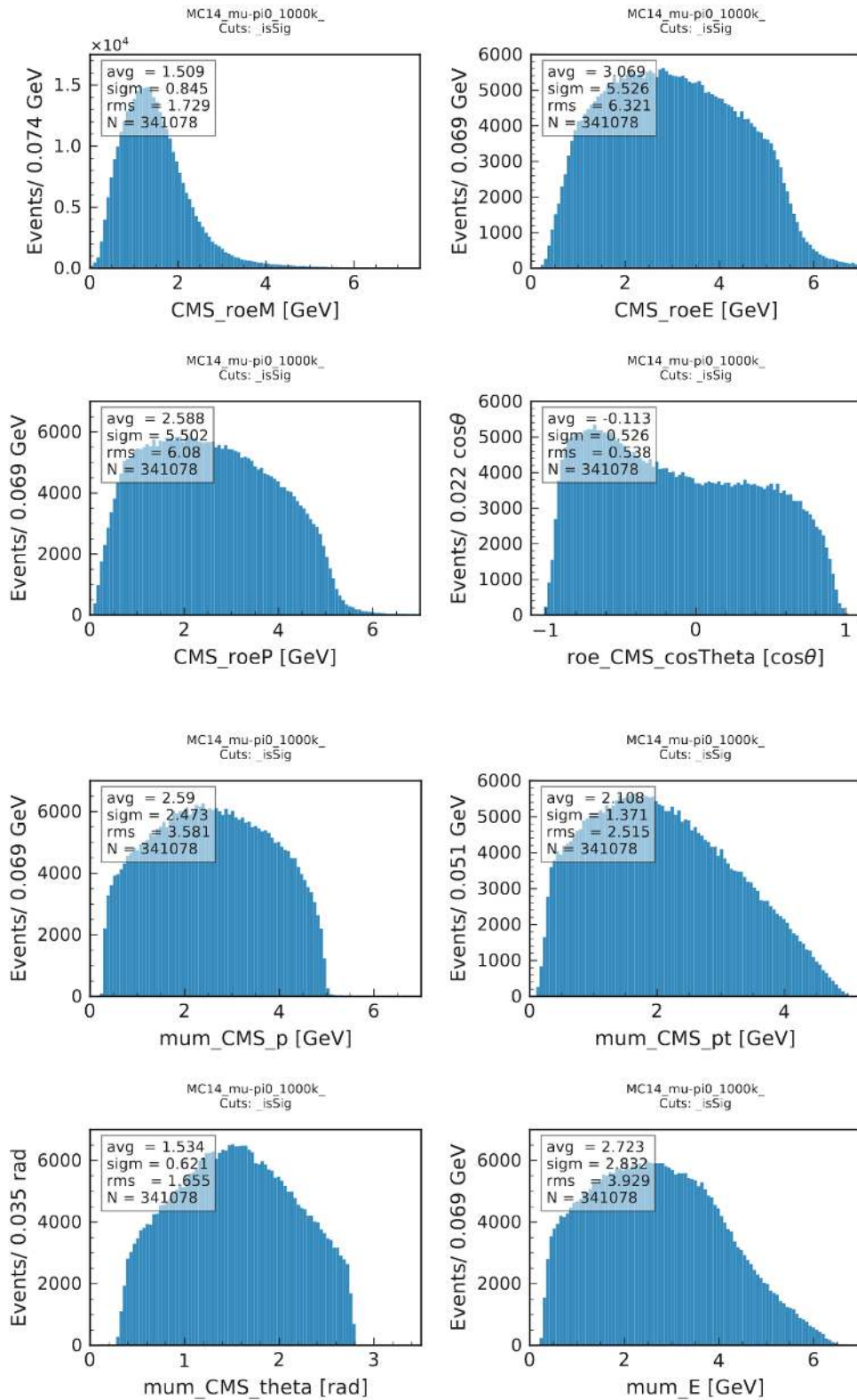


Figure A.2: Reconstructed variables from signal sample, isSignal.(cont.)

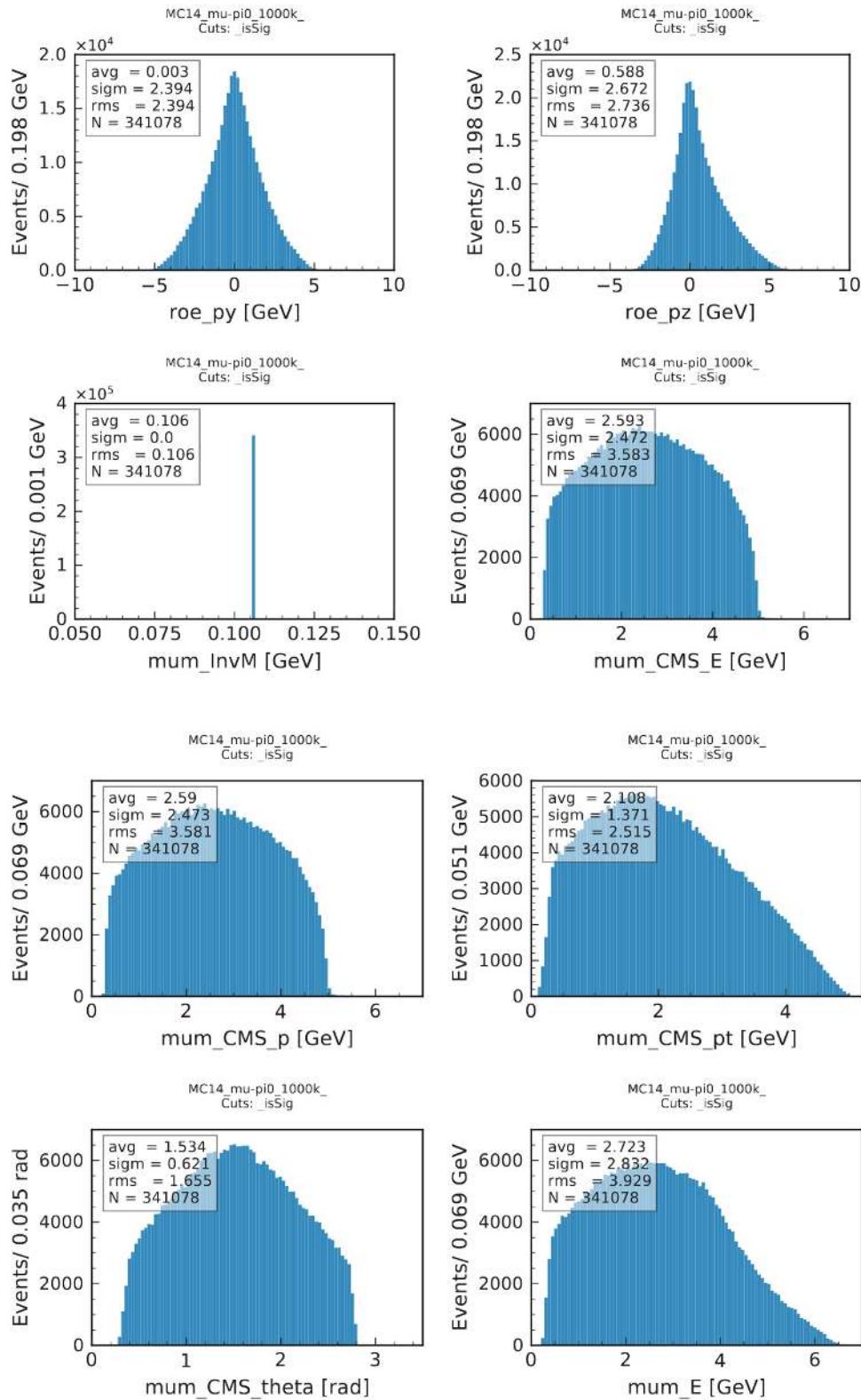


Figure A.2: Reconstructed variables from signal sample, isSignal.(cont.)

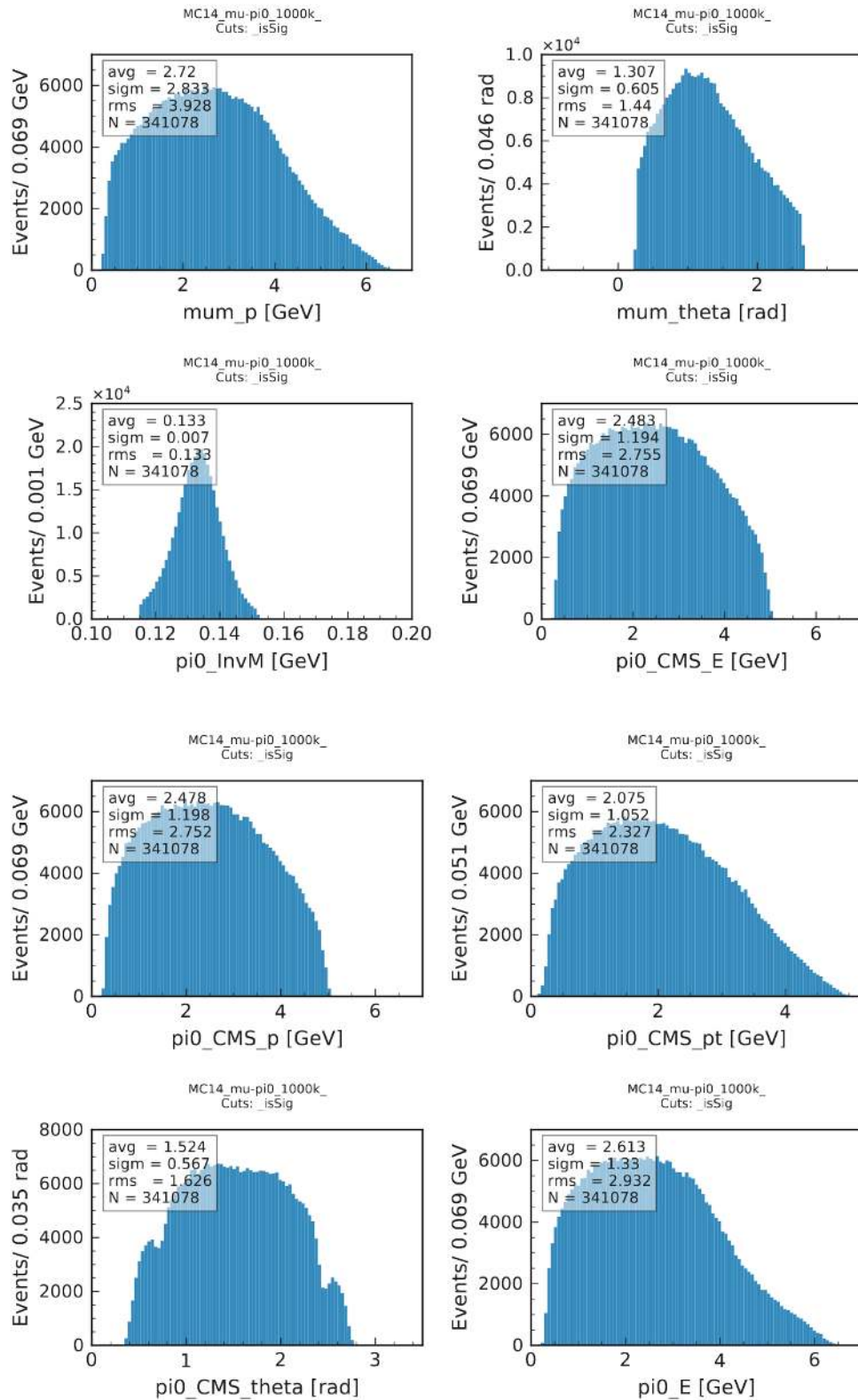


Figure A.2: Reconstructed variables from signal sample, isSignal.(cont.)

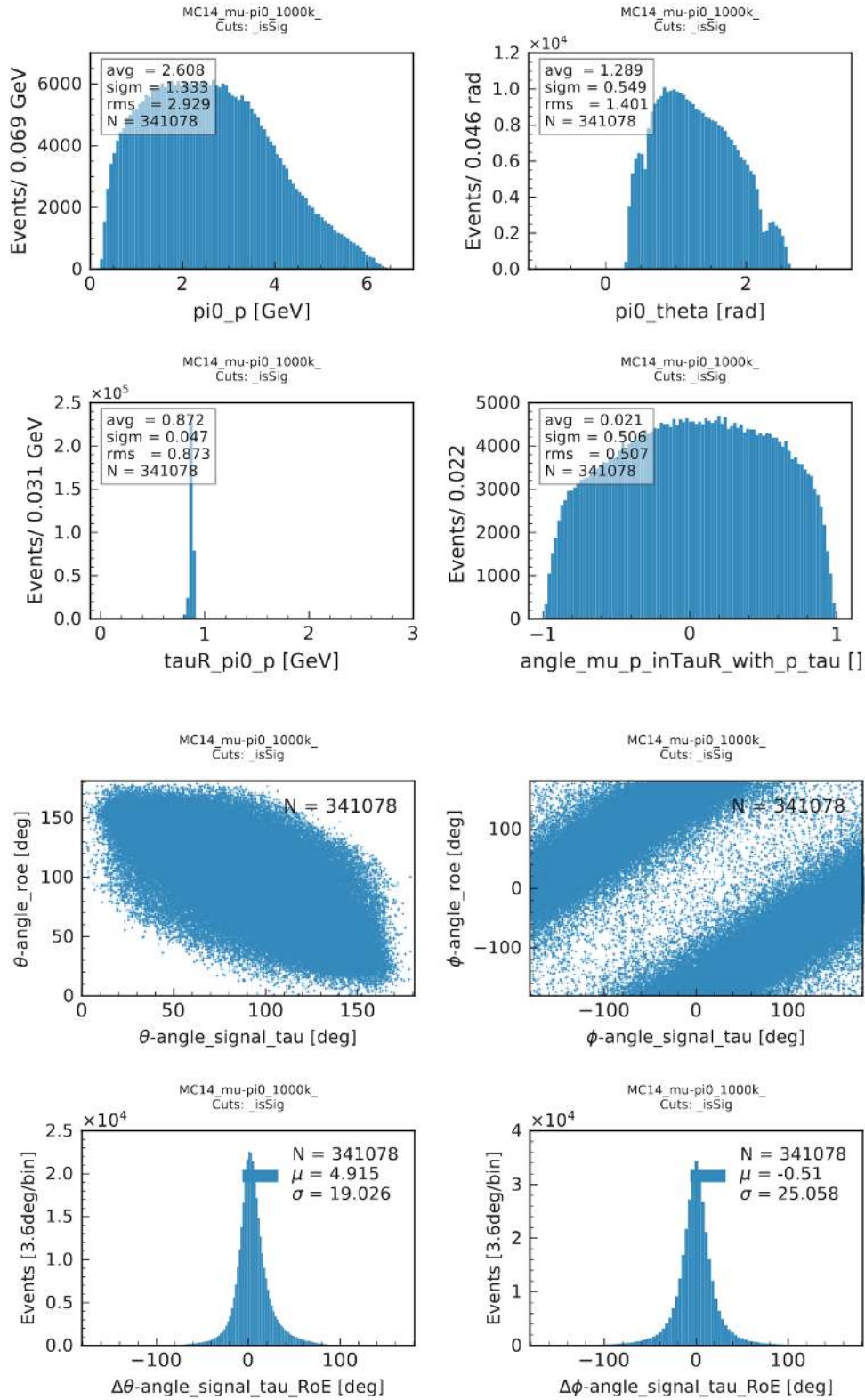


Figure A.2: Reconstructed variables from signal sample, isSignal.(cont.)

Reconstructed Variables from Signal Sample (All Candidates)

These figures show the distributions of different variables of the signal sample before the first cut without requiring the variable *isSignal* to be true, i.e. also including wrong candidates for the signal τ . First, we have the cut-variables, followed by event variables and kinematic properties of the signal τ in the CMS and laboratory frame. Then, there are the same kinematic properties, but for the ROE, the μ and the π^0 . Finally, we see some miscellaneous variables, such as the difference in polar and azimuth angle between the signal τ and the ROE.

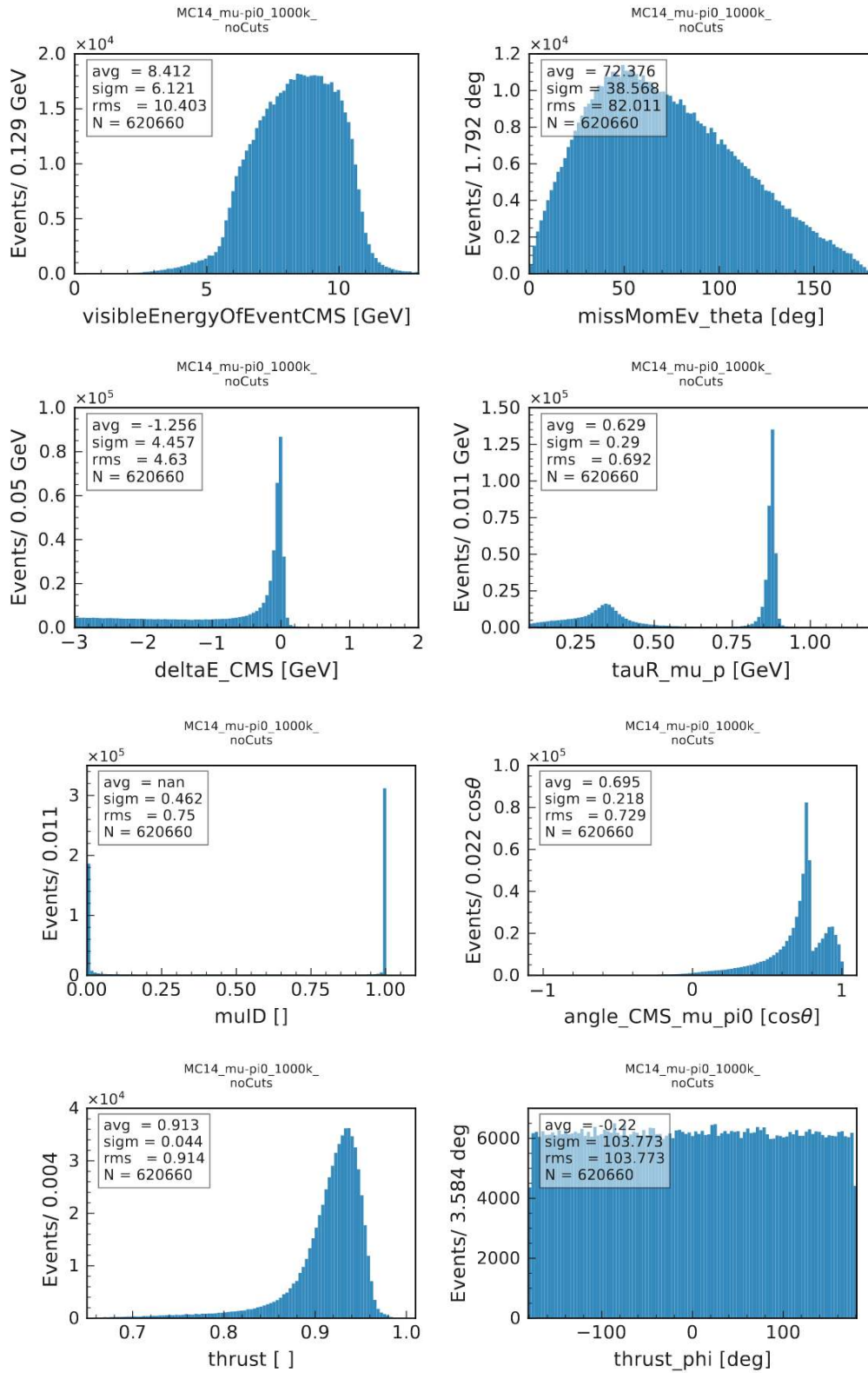


Figure A.3: Reconstructed variables from signal sample, all candidates.

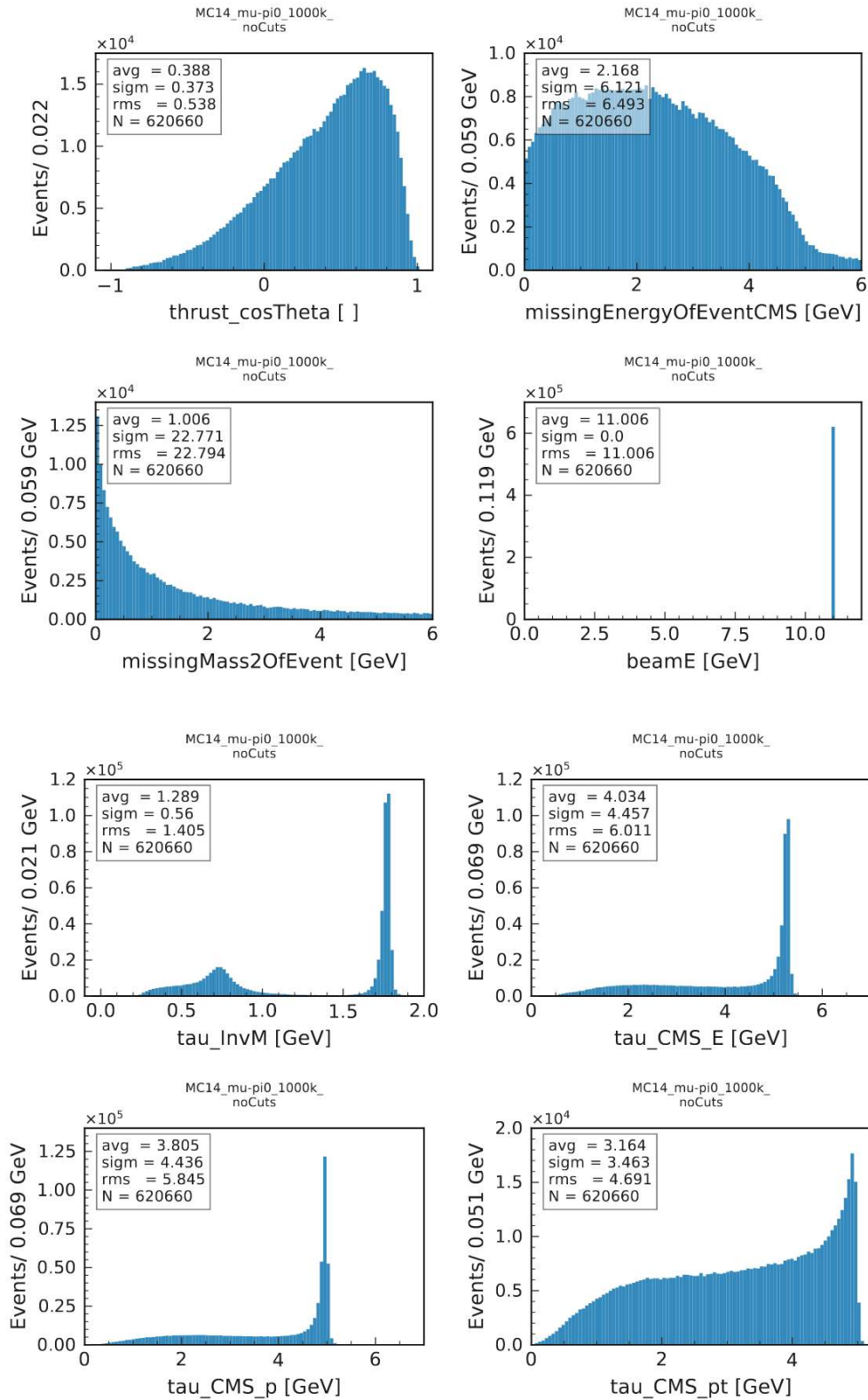


Figure A.3: Reconstructed variables from signal sample, all candidates.(cont.)

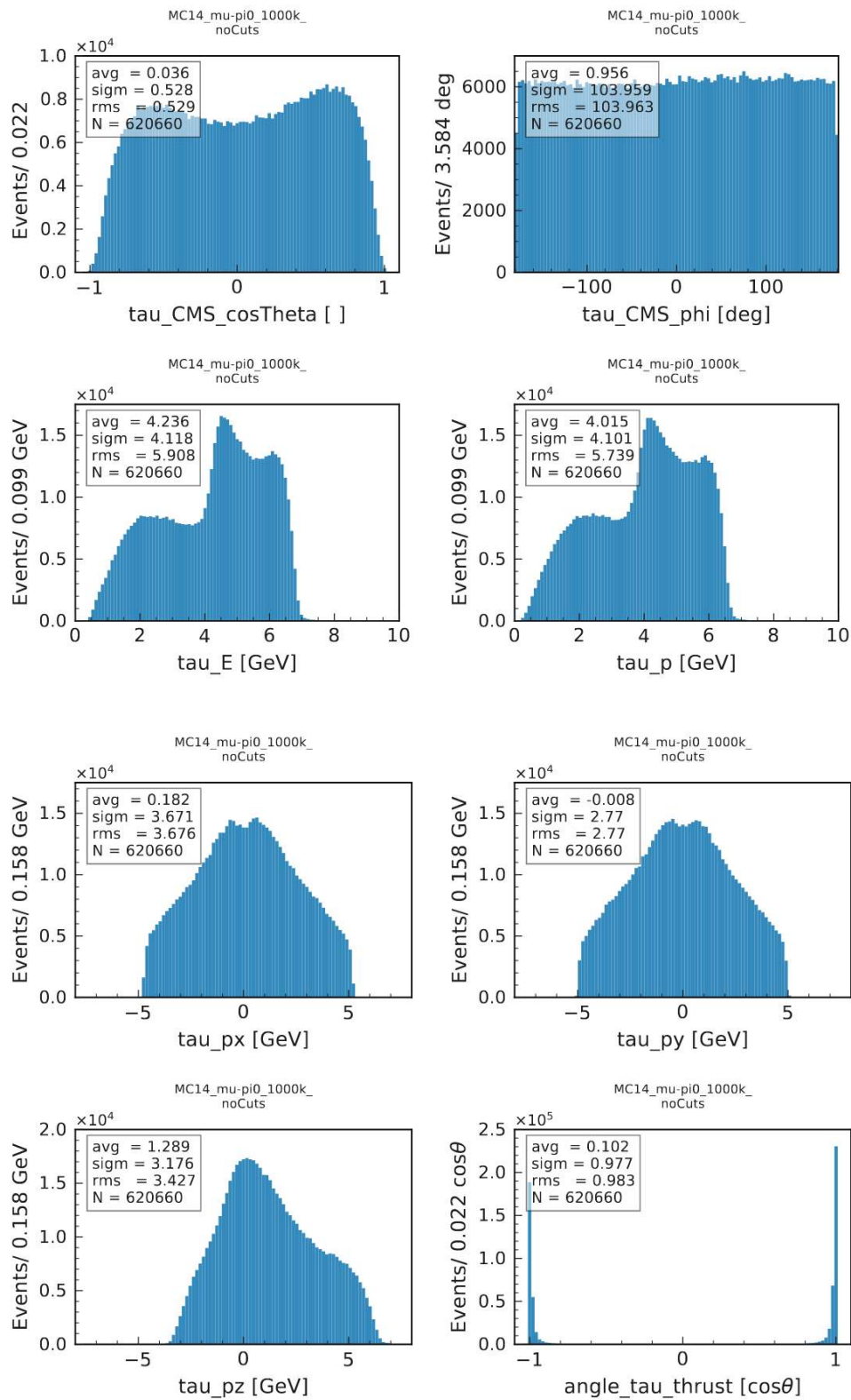


Figure A.3: Reconstructed variables from signal sample, all candidates.(cont.)

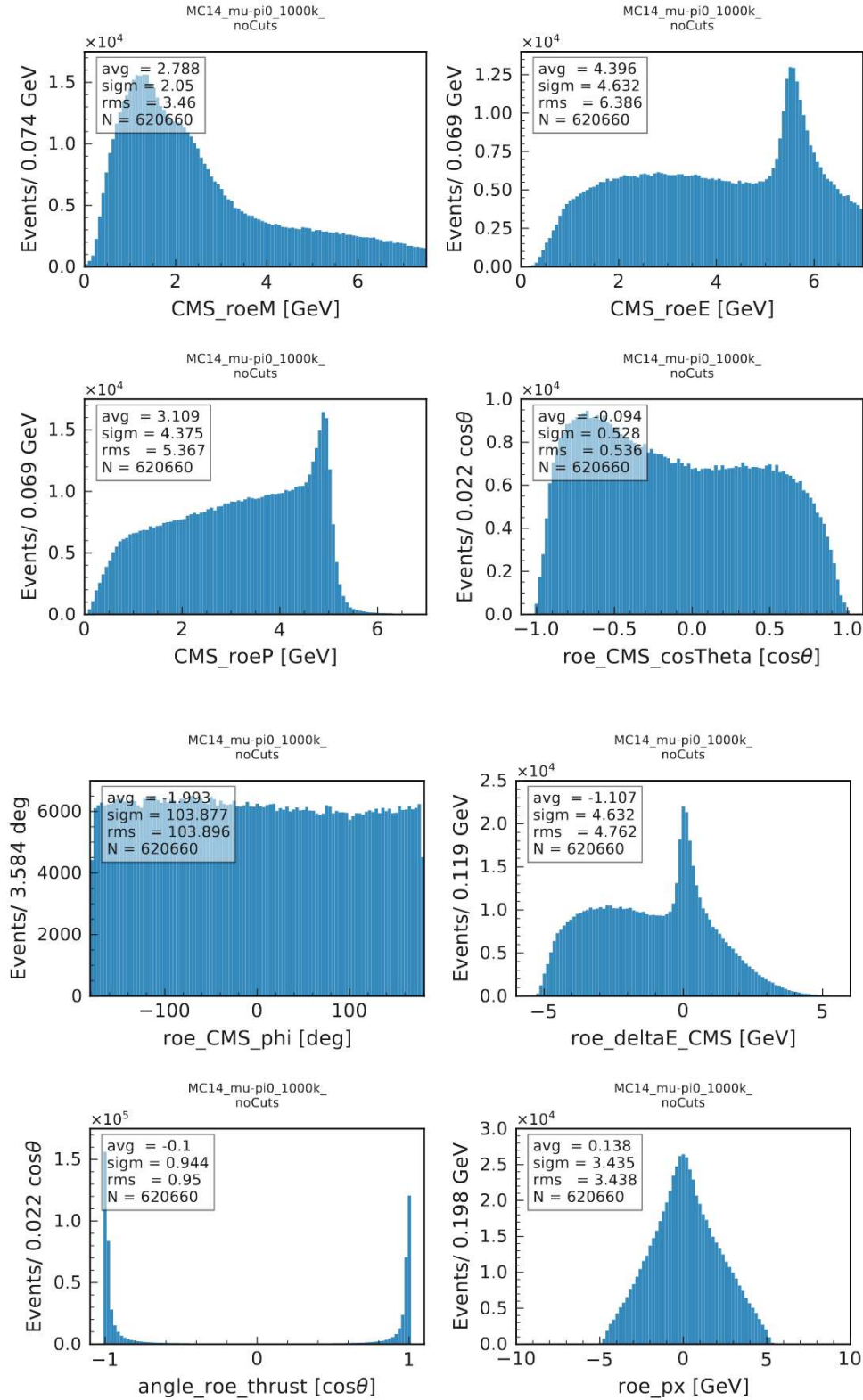


Figure A.3: Reconstructed variables from signal sample, all candidates.(cont.)

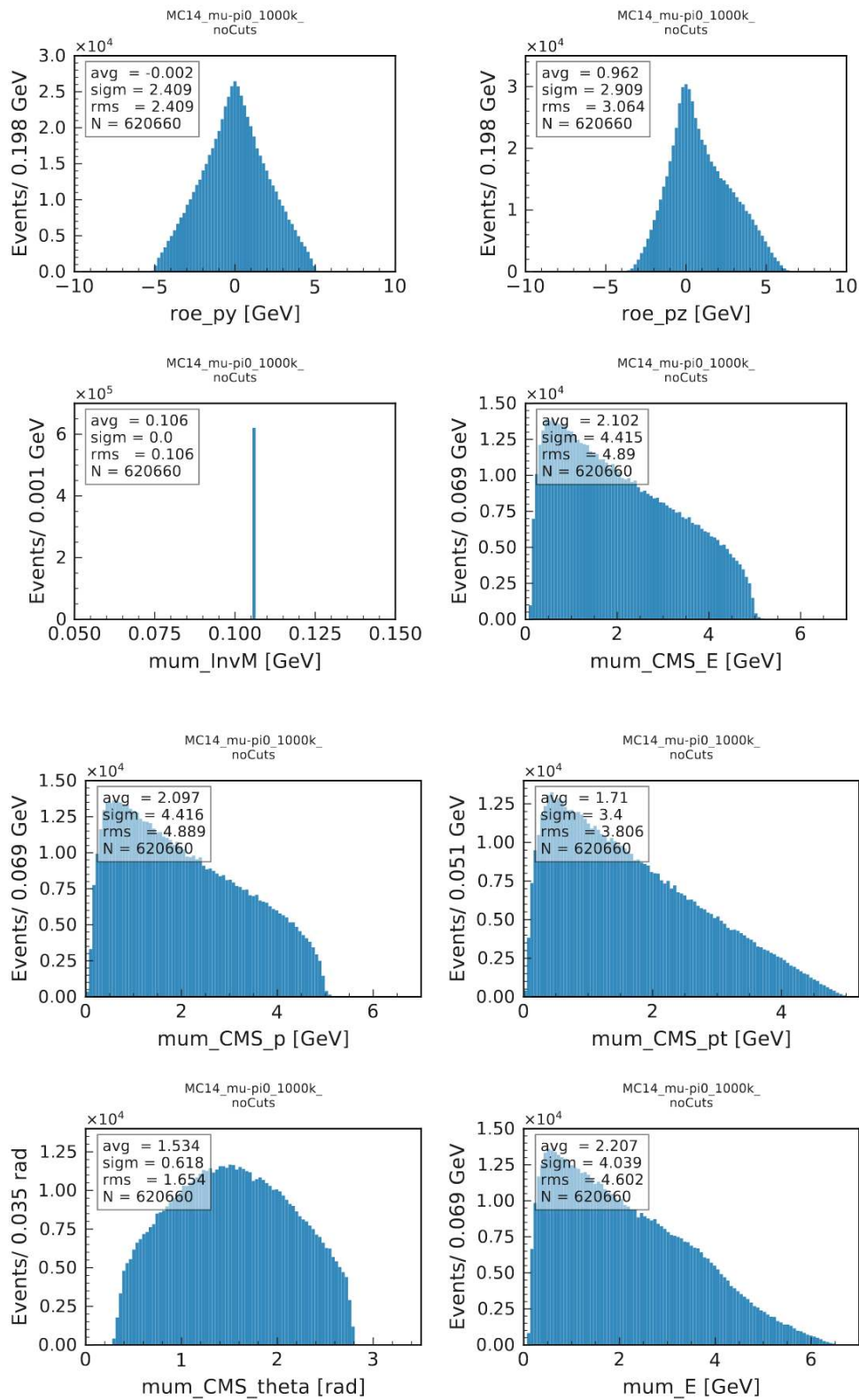


Figure A.3: Reconstructed variables from signal sample, all candidates.(cont.)

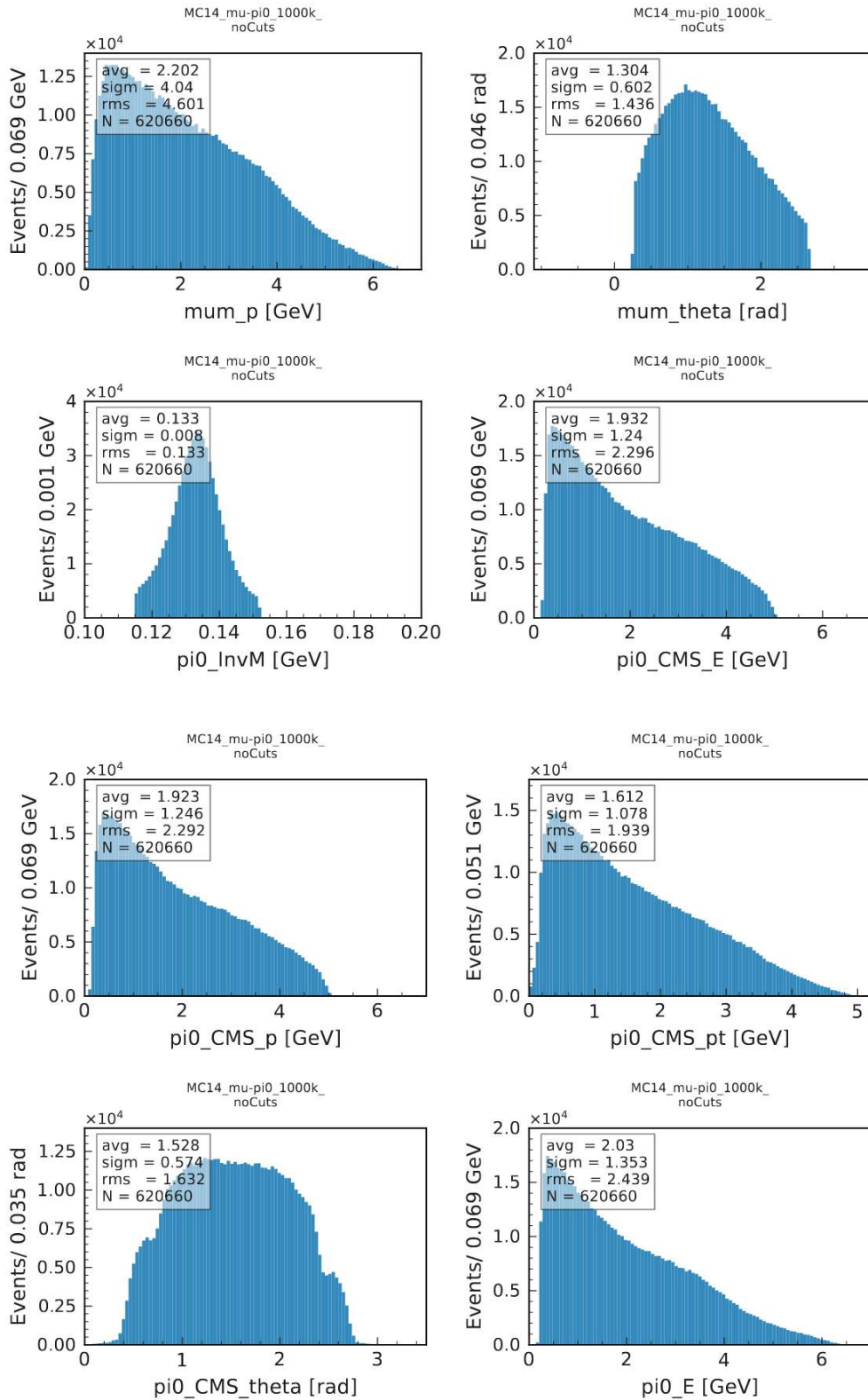


Figure A.3: Reconstructed variables from signal sample, all candidates.(cont.)

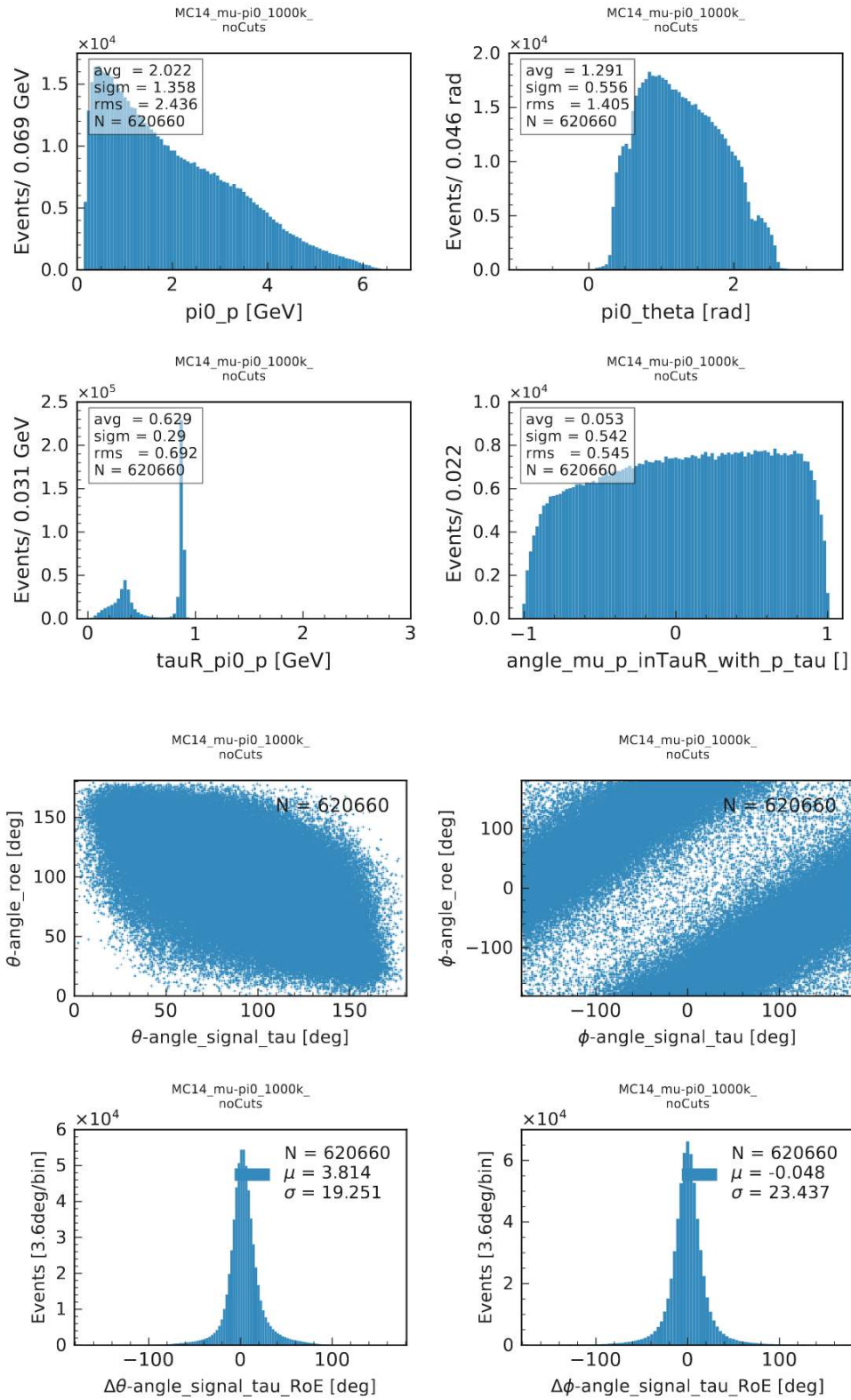


Figure A.3: Reconstructed variables from signal sample, all candidates.(cont.)

Distributions of Cut-Variables of BG without Cuts

These figures show the distribution of all cut variables for each background after passing the preselection and before applying the first cut.

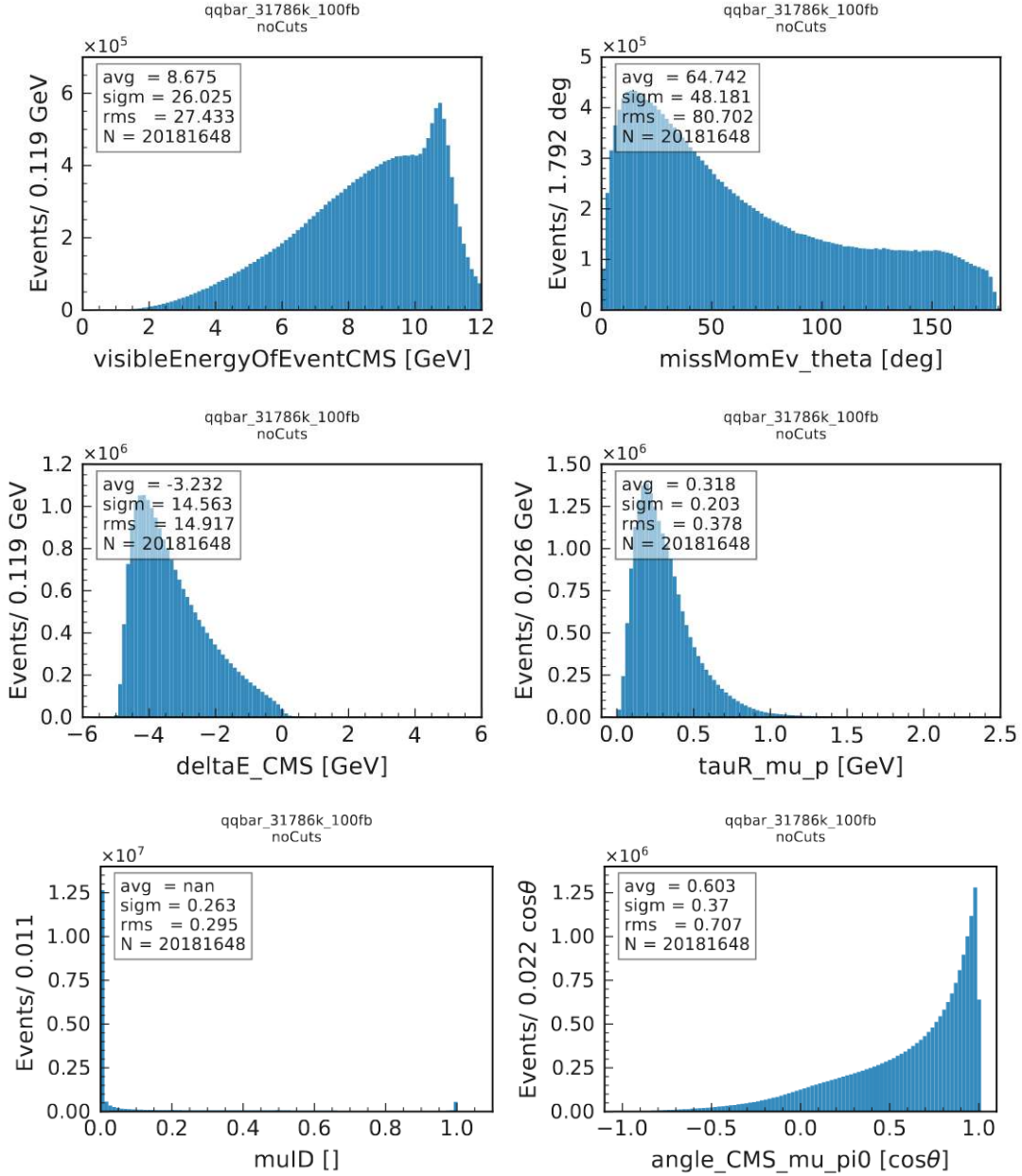


Figure A.4: Distribution of Cut-variables of $q\bar{q}$ sample without cuts.

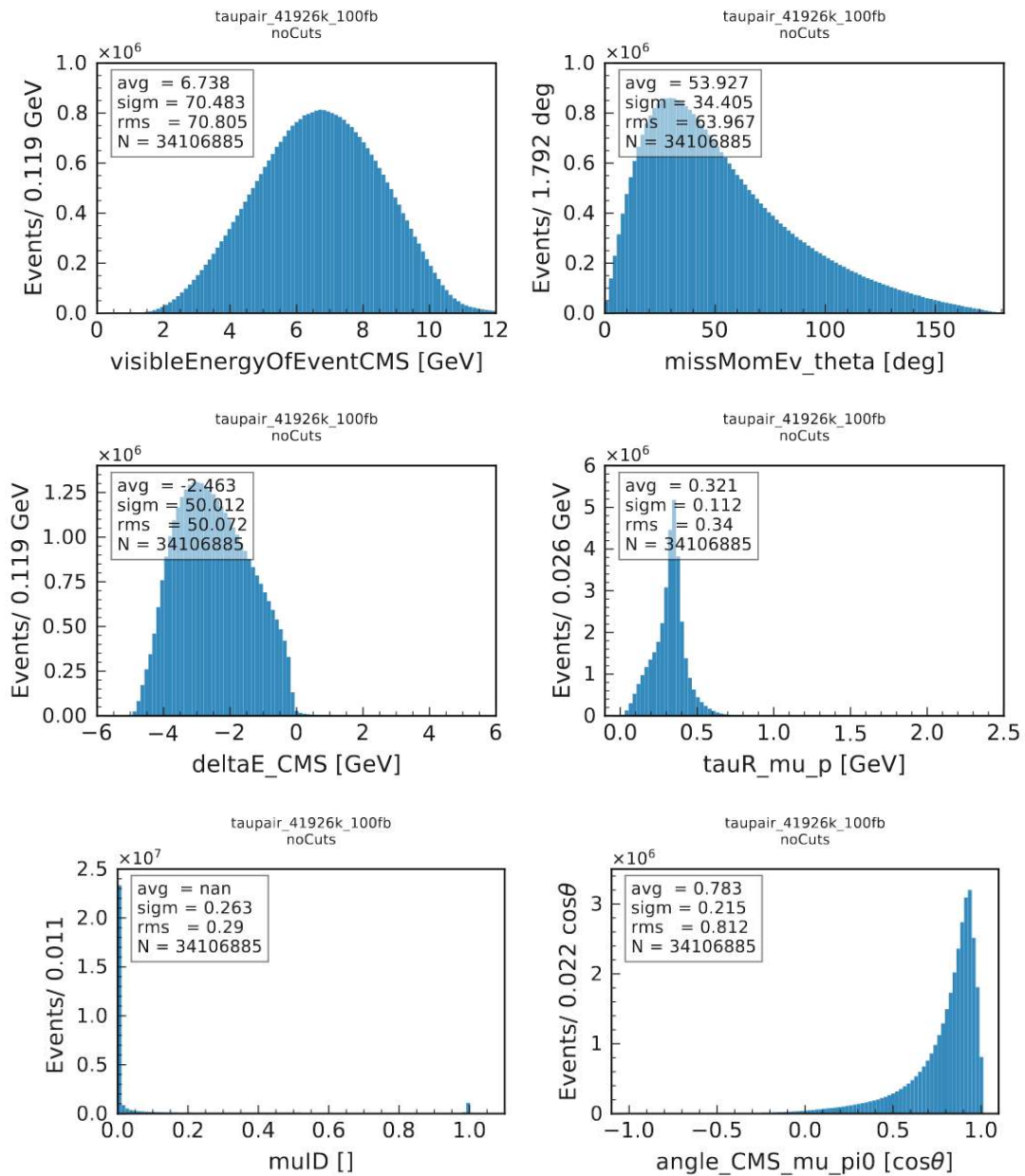


Figure A.5: Distribution of Cut-variables of generic $\tau^+\tau^-$ sample without cuts.

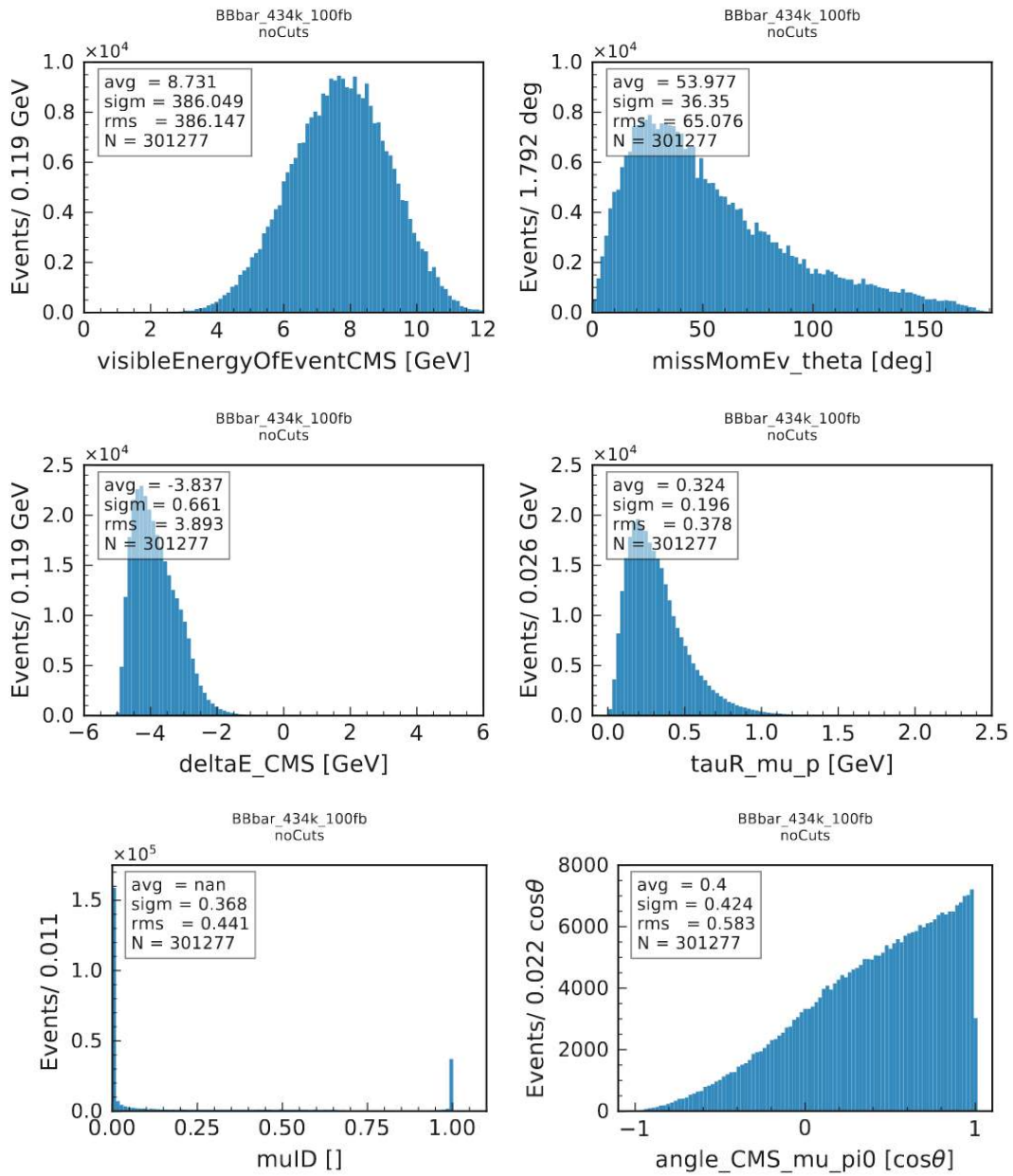


Figure A.6: Distribution of Cut-variables of $B\bar{B}$ sample without cuts.

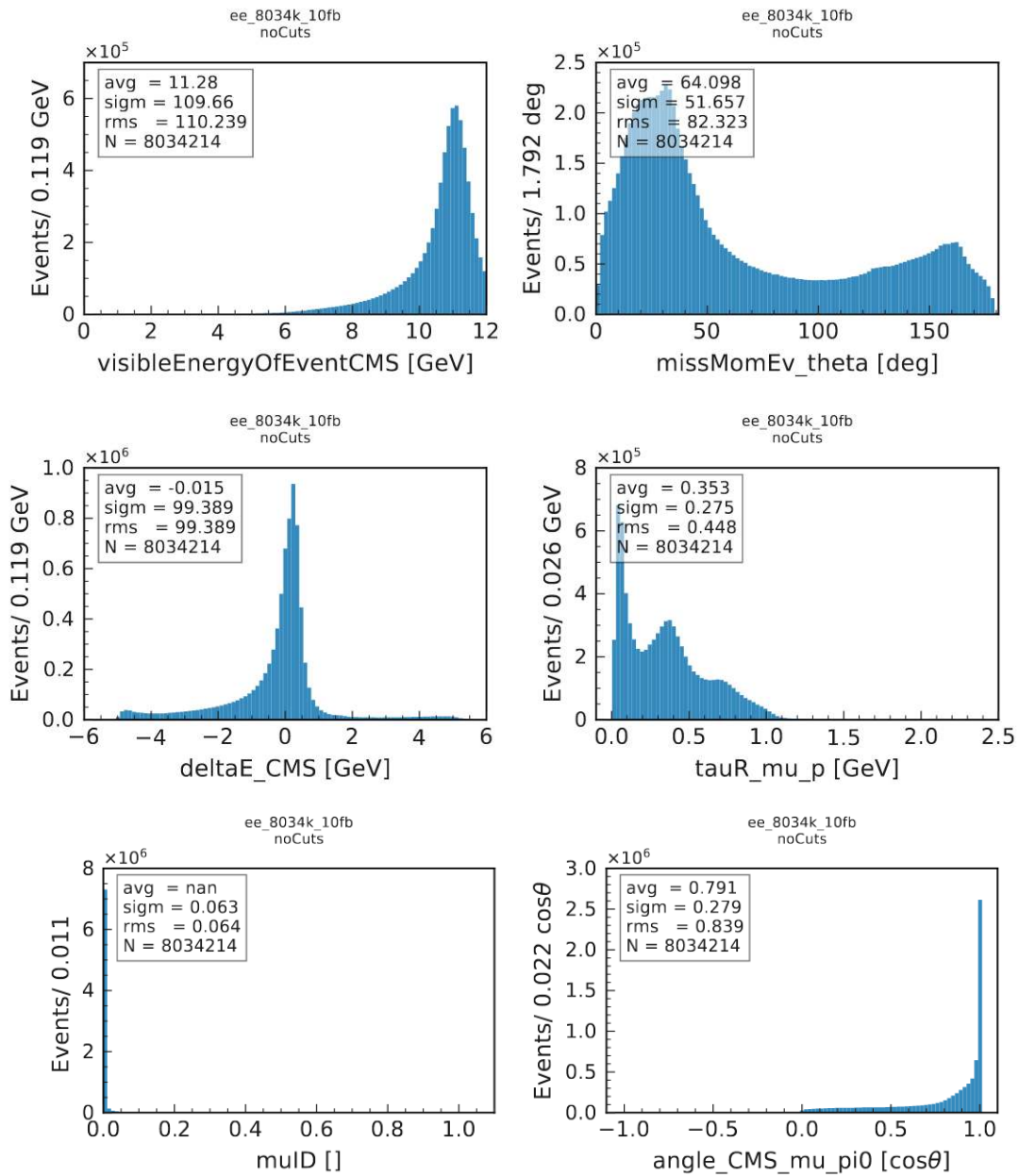


Figure A.7: Distribution of Cut-variables of $e^+e^- \gamma$ sample without cuts.

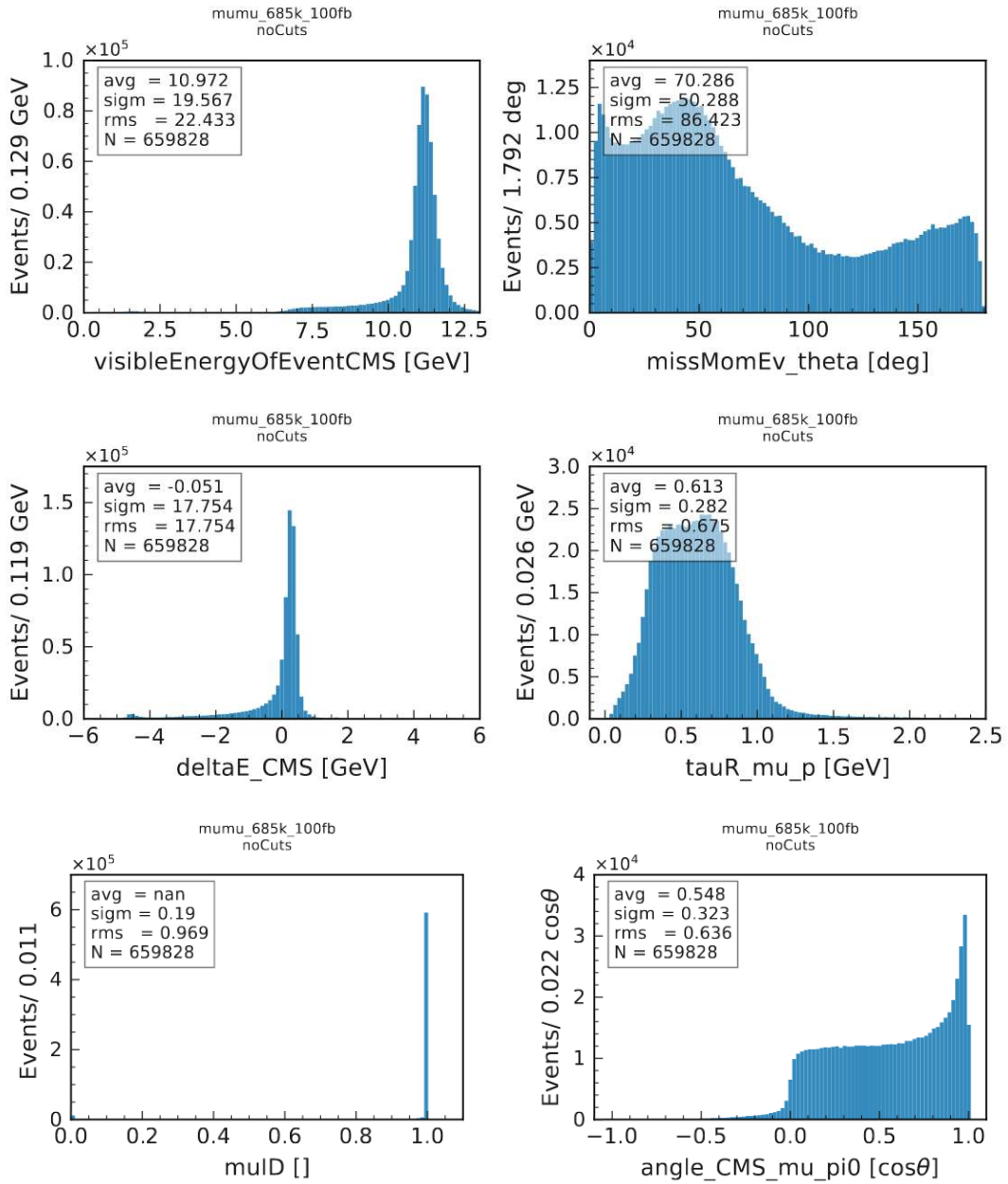


Figure A.8: Distribution of Cut-variables of $\mu^+ \mu^- \gamma$ sample without cuts.

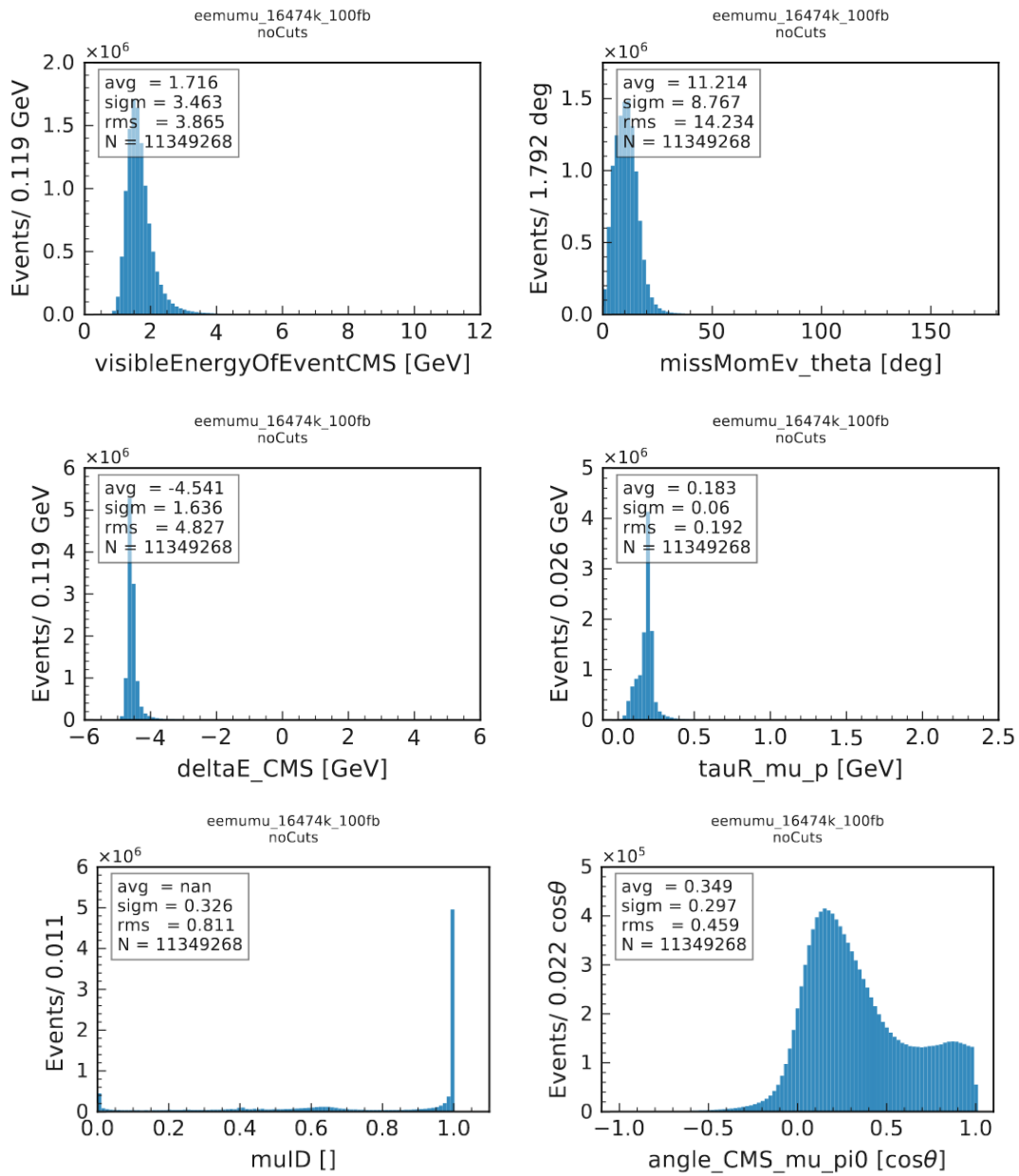


Figure A.9: Distribution of Cut-variables of $e^+e^- \mu^+ \mu^-$ sample without cuts

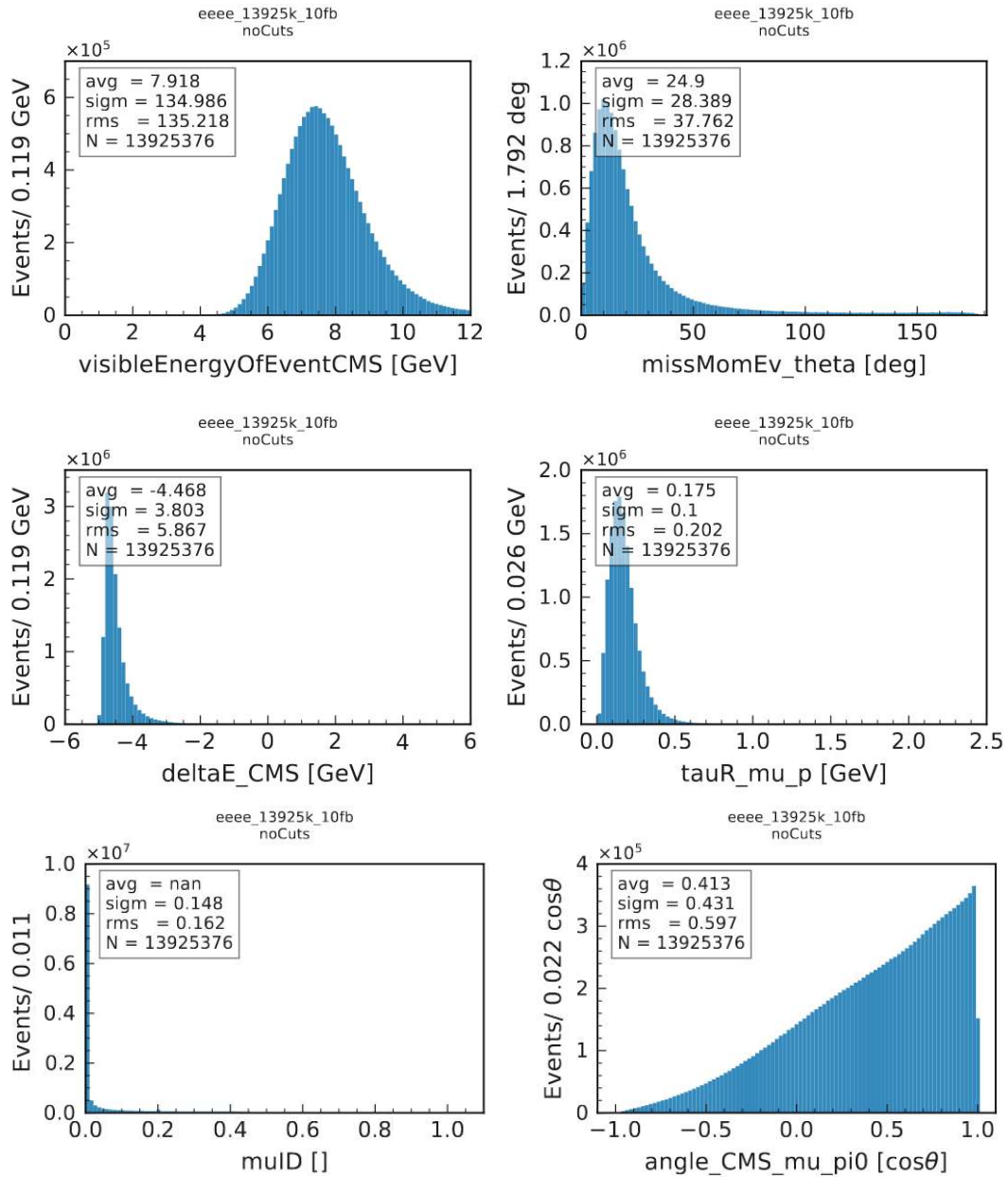


Figure A.10: Distribution of Cut-variables of $e^+e^-e^+e^-$ sample without cuts

Muon-ID Distribution of Signal and Background

These figures show the distribution of the muon-ID for the signal and all BG types before applying the muID cut in sect. 4.7.

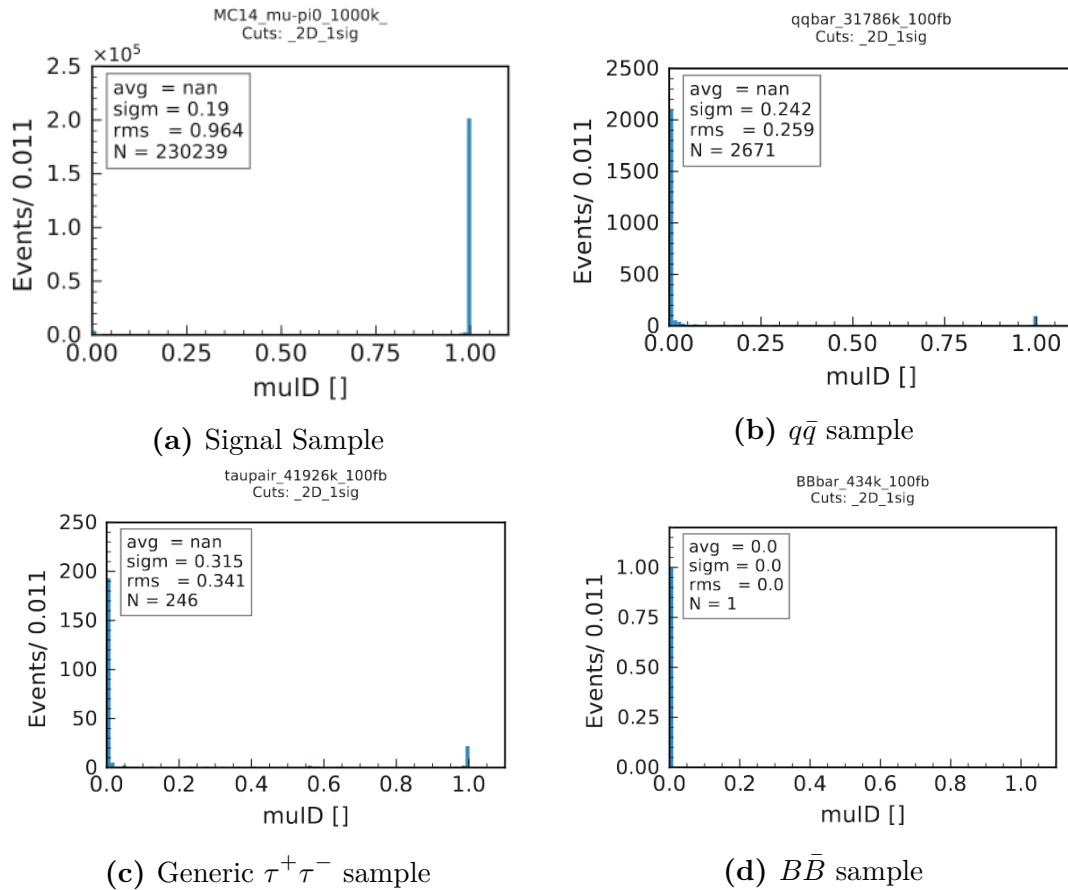


Figure A.11: Distribution of muon-ID for different event types. A higher value corresponds to a higher probability for the detected particle to be a muon.

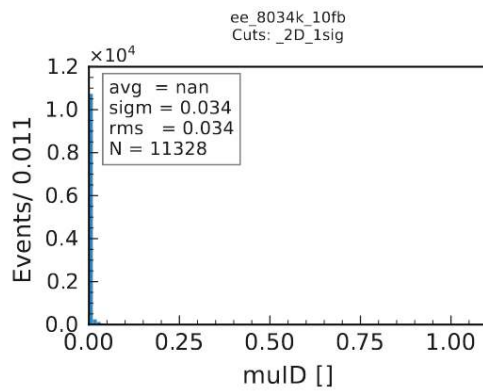
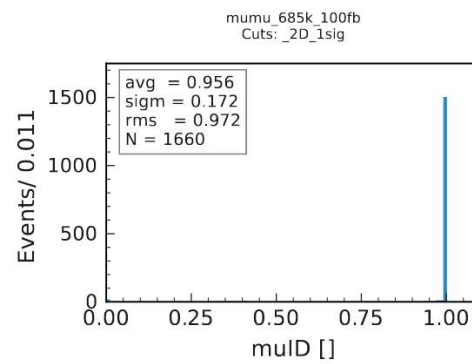
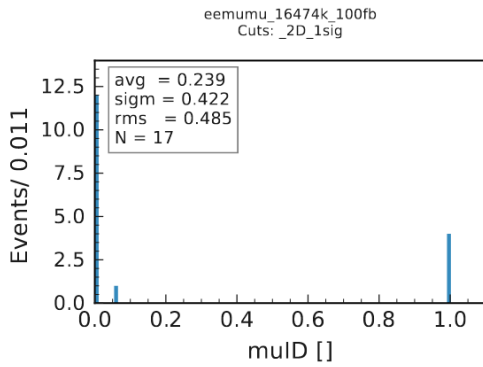
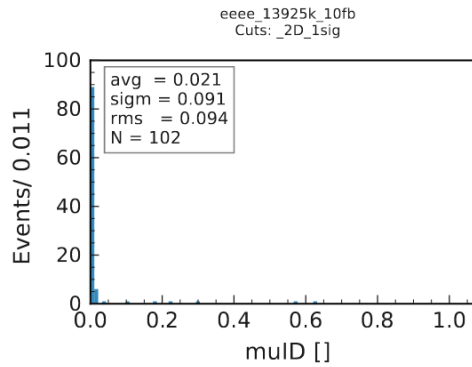
(e) $e^+e^-\gamma$ sample(f) $\mu^+\mu^-\gamma$ sample(g) $e^+e^-\mu^+\mu^-$ sample(h) $e^+e^-e^+e^-$ sample

Figure A.11: Distribution of muon-ID for different event types. A higher value corresponds to a higher probability for the detected particle to be a muon.

B Calculation of the Upper Limit

The following part describes, how the upper limit was calculated by using the results of the selection criteria on MC data and assuming finding N events in the real data [31].

We are interested in the probability distribution of our parameters given the data we measure (and simulate). Using Bayes's theorem, we can write this in terms of the likelihood of the data given our parameters:

$$P(\text{parameters}|\text{data}) = \mathcal{L}(\text{data}|\text{parameters}) P_0(\text{parameters}). \quad (\text{B.1})$$

The left-hand side is the probability density function of our parameters *after* including knowledge of the data—it is therefore called the posterior probability. The second factor on the right-hand side is the probability density function of our parameters *before* including knowledge of the data—it is therefore called the prior probability.

Our data is the number of events observed in the real data and in the simulated data. We need to write down the likelihoods for each of these.

The number of events observed in the data, N , is a statistical fluctuation around the expected number of events, ν . The likelihood for the observed number of events given this expectation is a Poisson distribution:

$$\mathcal{L}(N|\nu) = \frac{\nu^N e^{-\nu}}{N!}. \quad (\text{B.2})$$

The expectation has a contribution from signal and from each of the background sources,

$$\nu = \nu_s + \sum_i \nu_{b,i} \quad (\text{B.3})$$

where

$$\nu_s = \epsilon_s \mathcal{B}_s \mathcal{B}_t \sigma L, \quad \text{and} \quad \nu_{b,i} = \epsilon_{b,i} \sigma_{b,i} L, \quad (\text{B.4})$$

and ϵ_X and σ are the detection efficiency and production cross section for component X , L is the integrated luminosity of the data set, and \mathcal{B}_s and \mathcal{B}_t are the signal and tag branching fractions.

For each MC sample, the likelihood for m events passing the selection criteria, when we simulate M events, is given by the binomial distribution,

$$L(m|M, \epsilon) = \frac{M!}{m!(M-m)!} \epsilon^m (1-\epsilon)^{M-m}, \quad (\text{B.5})$$

with one parameter: the efficiency, ϵ , for observing such an event. Alternatively, we could write it in terms of a suppression factor for such events, $\rho \equiv 1 - \epsilon$:

$$L(m|M, \rho) = \frac{M!}{m!(M-m)!} (1-\rho)^m \rho^{M-m}. \quad (\text{B.6})$$

In summary, our data is

- N , the number of events observed in real data and
- M_i, m_i , the numbers of events generated and observed in each simulated data set

and our parameters are

- ϵ_i , the efficiency for detecting each component,
- σ_i , the cross section for producing each component,
- L , the integrated luminosity of the real data set,
- \mathcal{B}_t , the branching fraction for the tag-side decay, and
- \mathcal{B}_s , the branching fraction for our signal decay.

It is that last one we are most interested in. The other parameters are “nuisance” parameters.

The prior probability density function in equation (B.1) can be factorized:

$$P_0(\text{parameters}) = \prod_i P_0(\text{parameter } i). \quad (\text{B.7})$$

We don’t have any prior information for the efficiency parameters and choose a uniform distribution (within the allowed range) for each:

$$P_0(\epsilon_i) = \begin{cases} 1, & \text{if } \epsilon_i \in [0, 1], \\ 0, & \text{else.} \end{cases} \quad (\text{B.8})$$

The cross sections, integrated luminosity, and tag-side branching fraction have prior probability distributions given by the knowledge of each parameter from external information—most likely normal (“Gaussian”) distributions. For the cross sections, this knowledge is the measured (or theoretically calculated) values and their uncertainties. For the integrated luminosity, it’s the known luminosity and its uncertainty from Belle II. For the branching fraction, it’s the value (or values) in the PDG.

We also need a prior distribution for the parameter of interest, \mathcal{B}_s . Here we have some choices and the analysis should be checked with several priors. Two good choices are the a prior flat in the value of \mathcal{B}_s and a prior flat in the scale (order of magnitude) of \mathcal{B}_s . The former is

$$P_0(\mathcal{B}_s) = \begin{cases} 1, & \text{if } \epsilon_i \in [0, 1], \\ 0, & \text{else.} \end{cases} \quad (\text{B.9})$$

The latter is

$$P_0(\mathcal{B}_s) = \frac{1}{c \ln 10} \begin{cases} \frac{1}{\mathcal{B}_s}, & \text{if } \mathcal{B}_s \in [10^{-c}, 1], \\ 0, & \text{else,} \end{cases} \quad (\text{B.10})$$

where the cutoff 10^{-c} allows us to define a proper prior (one that is normalized). An improper prior over the range $[0, 1]$ can also be tested.

Putting all the above pieces together, we get the posterior probability distribution

$$\begin{aligned} P(\mathcal{B}_s, \mathcal{B}_t, L, \vec{\sigma}, \vec{\epsilon} | N, m, M) &= \mathcal{L}\left(N | [\epsilon_s \mathcal{B}_s \mathcal{B}_t \sigma + \sum_i \epsilon_{b,i} \sigma_{b,i}] L\right) \prod_i \mathcal{L}(m_i | M_i, \epsilon_i) \\ &\times P_0(\mathcal{B}_s) P_0(\mathcal{B}_t) P_0(L) \prod_i P_0(\sigma_i) \prod_i P_0(\epsilon_i). \end{aligned} \quad (\text{B.11})$$

But we only want the Probability Distribution Function (PDF) for \mathcal{B}_s , so we integrate out the other parameters:

$$P(\mathcal{B}_s) = \int P(\mathcal{B}_s, \mathcal{B}_t, L, \vec{\sigma}, \vec{\epsilon} | N, m, M) d\mathcal{B}_t dL \prod_i d\sigma_i \prod_i d\epsilon_i. \quad (\text{B.12})$$

Assuming a value for N and inserting the results of this analysis together with the required cross-sections the integral can be solved numerically. Fig. B.1 shows the different PDF with the respective upper limit in a 95% CI.

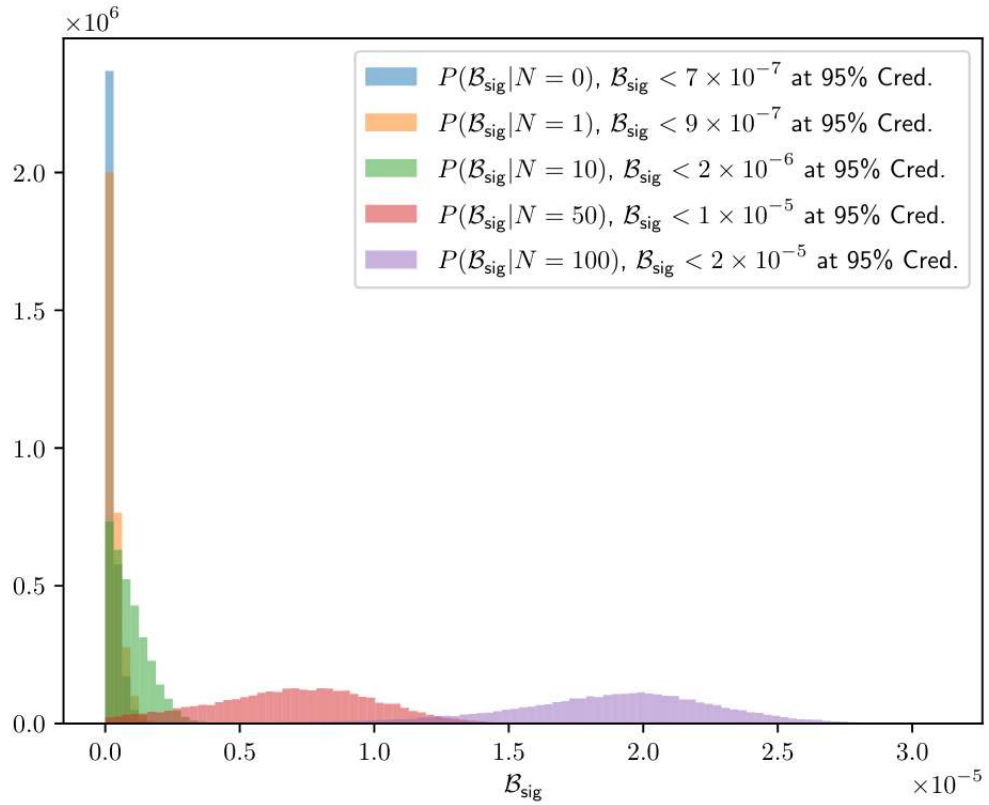


Figure B.1: Probability Distribution Function for the branching fraction of $\tau \rightarrow \mu \pi^0$ assuming N events are found in the data.

List of Figures

2.1	All particles of the Standard Model [4]	9
2.2	Examples for conservation of lepton flavor in the SM	12
2.3	Decay modes of τ depending on the number of charged particles (Prongs) in the final state.	14
2.4	Diagrams of NP-tree-level decays for $\tau \rightarrow \mu \pi^0$	16
2.5	Examples of possible LFV loop diagrams in SUSY models using charginos χ^\pm , sneutrinos $\tilde{\nu}$ and leptoquarks.	16
3.1	Schedule for the luminosity reached by SuperKEKB.	18
3.2	Schematics of the SuperKEKB storage ring structure.	19
3.3	Coordinate system of Belle II [21].	21
3.4	Belle II detector and its components [22].	21
3.5	Schematic view of the Belle II vertex detector with a Be beam pipe, two pixelated layers and four layers of silicon strip sensors [19].	22
3.6	Longitudinal view of the CDC. Borders of the 50 cylindrical layers wrapped symmetrically around the beam are depicted in black [23].	23
3.7	View in beam direction of a two-track event recorded in the Central Drift Chamber (CDC).	23
3.8	Working principle of the two Cherenkov detectors.	25
4.1	Current 90% C.L. upper limits for the branching fraction of τ LFV decays in the CLEO, BaBar and Belle experiments [19].	30
4.2	Comparison of generator level MC distributions (blue) to the by the detector correctly reconstructed muons (red).	35
4.3	Comparison of generator level MC distributions (blue) to the by the detector correctly reconstructed photons (red)	35
4.4	Reconstructed invariant mass of the π^0 .	37
4.5	Distribution of the thrust observable for different event types.	38

4.6	Number of correctly reconstructed signal events depending on what cuts are made and compared with amount of false candidates on the left and right plot respectively.	39
4.7	Invariant mass, energy, momentum and transverse momentum in the CMS of the reconstructed signal τ in the signal sample.	40
4.8	Polar and azimuth angle distribution in the CMS and the energy and momentum in the laboratory frame	41
4.9	Distribution of the three momentum components in the laboratory frame of the reconstructed signal τ in the signal sample.	42
4.10	Distribution ΔE and muon momentum in the τ restframe in the signal sample.	43
4.11	2D distributions of ΔE versus muon momentum in the τ restframe.	43
4.13	2D Distributions of signal and BG samples after cutting on 1σ area around signal peak in the signal area.	48
4.14	Distribution of the visible energy for signal and BG samples. The red vertical lines indicate the applied cuts.	51
4.15	Distribution of the polar angle θ of the direction of the missing momentum of an event for signal and BG samples. The red vertical lines indicate the applied cuts.	53
4.16	Distribution of the opening angle between the muon and the reconstructed π^0 of signal and BG samples. The red vertical lines indicate the applied cuts.	54
4.17	Distribution of signal and BG samples in the 2D signal area before the final cut marked by the red region.	56
4.18	Probability Distribution Function for the branching fraction of $\tau \rightarrow \mu \pi^0$, when N=0 events in the data are assumed. [31]	58
A.1	Comparison of generator and reconstruction level of tauons	63
A.2	Reconstructed variables from signal sample, isSignal.	65
A.2	Reconstructed variables from signal sample, isSignal.(cont.)	66
A.2	Reconstructed variables from signal sample, isSignal.(cont.)	67
A.2	Reconstructed variables from signal sample, isSignal.(cont.)	68
A.2	Reconstructed variables from signal sample, isSignal.(cont.)	69
A.2	Reconstructed variables from signal sample, isSignal.(cont.)	70
A.2	Reconstructed variables from signal sample, isSignal.(cont.)	71
A.3	Reconstructed variables from signal sample, all candidates.	73
A.3	Reconstructed variables from signal sample, all candidates.(cont.)	74
A.3	Reconstructed variables from signal sample, all candidates.(cont.)	75
A.3	Reconstructed variables from signal sample, all candidates.(cont.)	76

A.3	Reconstructed variables from signal sample, all candidates.(cont.) .	77
A.3	Reconstructed variables from signal sample, all candidates.(cont.) .	78
A.3	Reconstructed variables from signal sample, all candidates.(cont.) .	79
A.4	Distribution of Cut-variables of $q\bar{q}$ sample without cuts.	80
A.5	Distribution of Cut-variables of generic $\tau^+\tau^-$ sample without cuts. .	81
A.6	Distribution of Cut-variables of $B\bar{B}$ sample without cuts.	82
A.7	Distribution of Cut-variables of $e^+e^-\gamma$ sample without cuts.	83
A.8	Distribution of Cut-variables of $\mu^+\mu^-\gamma$ sample without cuts.	84
A.9	Distribution of Cut-variables of $e^+e^-\mu^+\mu^-$ sample without cuts . .	85
A.10	Distribution of Cut-variables of $e^+e^-e^+e^-$ sample without cuts . . .	86
A.11	Distribution of muon-ID for different event types. A higher value corresponds to a higher probability for the detected particle to be a muon.	87
A.11	Distribution of muon-ID for different event types. A higher value corresponds to a higher probability for the detected particle to be a muon.	88
B.1	Probability Distribution Function for the branching fraction of $\tau \rightarrow$ $\mu\pi^0$ assuming N events are found in the data.	92

List of Tables

2.1	Overview over Conservation of Quantum Numbers	11
2.2	Most common τ decay modes	14
4.1	Cuts and performance at BaBar at 339 fb^{-1} [25].	31
4.2	Cuts and performance of the at Belle at 401 fb^{-1} [26].	32
4.3	Preselection Cuts	36
4.4	MC14 samples with corresponding cross section and luminosity. . .	44
4.5	Number of events in all samples for different muon ID cuts.	49
4.6	Cutflow for remaining events in signal and BG samples. In the last cut, the $\mu^+\mu^-\gamma$ sample is replaced by a sample 5 times bigger. . . .	50
4.7	Cutflow for remaining events in signal and BG samples.	52
4.8	Cutflow for remaining events in signal and BG samples.	55
4.9	Final cutflow for remaining events in signal and BG samples.	56

Abbreviations

LFV	Lepton Flavor Violation
SM	Standard Model
NP	New Physics
SLAC	Stanford Linear Accelerator Center
LER	low energy ring
HER	high energy ring
IP	interaction point
SUSY	Supersymmetry
MC	Monte Carlo
CM	center of mass
CMS	center of mass system
PXD	Pixel Vertex Detector
VXD	Vertex Detector
SVD	Silicon Vertex Detector
DEPFET	Depleted P-channel Field Effect Transistor
ARICH	Aerogel Ring-Imaging CHerenkov
TOP	Time of Propagation
CDC	Central Drift Chamber
ECL	Electromagnetic Calorimeter
KLM	K_L^0 and μ Detector
RPC	resistive plate chamber
CI	Credible Interval
CL	Confidence Level
PDF	Probability Distribution Function
SiPM	silicon photo multiplier
STT	Single Track Trigger
PID	Particle Identification
SNO	Sudbury Neutrino Observatory

BDT	Boosted Decision Tree
BG	Background
LQ	leptoquarks
DAQ	Data Acquisition
GDL	Global Decision Logic
ROE	Rest of Event
basf2	Belle II Analysis Software Tool

Bibliography

- [1] Makoto Kobayashi. Unraveling the origins of the universe, 2009. URL https://global.jaxa.jp/article/interview/vol43/p3_e.html.
- [2] G. Aad, T. Abajyan, B. Abbott, J. Abdallah, S. Abdel Khalek, A.A. Abdelalim, O. Abdinov, R. Aben, B. Abi, M. Abolins, and et al. Observation of a new particle in the search for the Standard Model Higgs boson with the ATLAS detector at the LHC. *Physics Letters B*, 716(1):1–29, Sep 2012. ISSN 0370-2693. doi: 10.1016/j.physletb.2012.08.020. URL <http://dx.doi.org/10.1016/j.physletb.2012.08.020>.
- [3] Fermilab. First results from Fermilab’s Muon g-2 experiment strengthen evidence of new physics, Apr 2021. URL <https://t1p.de/1f7n>.
- [4] Particles of the standard model, Oct 2021. URL https://en.wikipedia.org/wiki/File:Standard_Model_of_Elementary_Particles.svg#/media/File:Standard_Model_of_Elementary_Particles_modified_version.svg.
- [5] Authors own work, 2021.
- [6] Q. R. et al. Ahmad. Measurement of the Rate of ν - e+d \rightarrow p+p+e Interactions

- Produced by B8Solar Neutrinos at the Sudbury Neutrino Observatory. *Physical Review Letters*, 87(7), Jul 2001. ISSN 1079-7114. doi: 10.1103/physrevlett.87.071301. URL <http://dx.doi.org/10.1103/PhysRevLett.87.071301>.
- [7] Peter Fisher, Boris Kayser, and Kevin S. McFarland. Neutrino mass and oscillation. *Annual Review of Nuclear and Particle Science*, 49(1):481–527, 1999. doi: 10.1146/annurev.nucl.49.1.481. URL <https://doi.org/10.1146/annurev.nucl.49.1.481>.
- [8] S. Bilenky. Neutrino oscillations: From a historical perspective to the present status. *Nuclear Physics B*, 908:2–13, Jul 2016. ISSN 0550-3213. doi: 10.1016/j.nuclphysb.2016.01.025. URL <http://dx.doi.org/10.1016/j.nuclphysb.2016.01.025>.
- [9] Evgeny Kh Akhmedov. Do charged leptons oscillate? *Journal of High Energy Physics*, 2007(09):116–116, Sep 2007. ISSN 1029-8479. doi: 10.1088/1126-6708/2007/09/116. URL <http://dx.doi.org/10.1088/1126-6708/2007/09/116>.
- [10] P.A. Zyla et al. Review of Particle Physics. *PTEP*, 2020(8):083C01, 2020. doi: 10.1093/ptep/ptaa104.
- [11] Deirdre Black, Tao Han, Hong-Jian He, and Marc Sher. $\tau - \mu$ flavor violation as a probe of the scale of new physics. *Phys. Rev. D*, 66:053002, Sep 2002. doi: 10.1103/PhysRevD.66.053002. URL <https://link.aps.org/doi/10.1103/PhysRevD.66.053002>.
- [12] Wenjun Li, Yadong Yang, and Xiangdan Zhang. $\tau^- \rightarrow \mu^- \pi^0(\eta, \eta')$ decays in new physics scenarios beyond the standard model. *Phys. Rev. D*, 73:073005,

- Apr 2006. doi: 10.1103/PhysRevD.73.073005. URL <https://link.aps.org/doi/10.1103/PhysRevD.73.073005>.
- [13] Paul Langacker and Michael Plümacher. Flavor changing effects in theories with a heavy Z' boson with family nonuniversal couplings. *Physical Review D*, 62(1), Jun 2000. ISSN 1089-4918. doi: 10.1103/physrevd.62.013006. URL <http://dx.doi.org/10.1103/PhysRevD.62.013006>.
- [14] Ke-Sheng Sun, Tao Guo, Wei Li, Xiu-Yi Yang, and Shu-Min Zhao. Searching for lepton flavor violating decays $\tau \rightarrow Pl$ in the minimal R-symmetric supersymmetric standard model. *The European Physical Journal C*, 80(12), Dec 2020. ISSN 1434-6052. doi: 10.1140/epjc/s10052-020-08750-w. URL <http://dx.doi.org/10.1140/epjc/s10052-020-08750-w>.
- [15] Jin-Huan Sheng, Ru-Min Wang, and Ya-Dong Yang. Scalar Leptoquark Effects in the Lepton Flavor Violating Exclusive $b \rightarrow s\ell_i^- \ell_j^+$ Decays. *International Journal of Theoretical Physics*, 58(2):480–492, Nov 2018. ISSN 1572-9575. doi: 10.1007/s10773-018-3948-3. URL <http://dx.doi.org/10.1007/s10773-018-3948-3>.
- [16] Jolanta Brodzicka and for the Belle Collaboration. Physics achievements from the Belle experiment. *Progress of Theoretical and Experimental Physics*, 2012(1), 12 2012. ISSN 2050-3911. doi: 10.1093/ptep/pts072. URL <https://doi.org/10.1093/ptep/pts072>. 04D001.
- [17] High Energy Accelerator Research Organization KEK. Luminosity Projection, Oct 2021. URL https://www-superkekb.kek.jp/Luminosity_projection.html.

- [18] T. Abe, I. Adachi, K. Adamczyk, et al. Belle II Technical Design Report, 2010.
- [19] E Kou, P Urquijo, W Altmannshofer, F Beaujean, G Bell, M Beneke, I I Bigi, F Bishara, M Blanke, C Bobeth, and et al. The Belle II Physics Book. *Progress of Theoretical and Experimental Physics*, 2019(12), Dec 2019. ISSN 2050-3911. doi: 10.1093/ptep/ptz106. URL <http://dx.doi.org/10.1093/ptep/ptz106>.
- [20] Sara Pohl and Christian Kiesling. *Track Reconstruction at the First Level Trigger of the Belle II Experiment*. PhD thesis, Ludwig-Maximilians-Universität Munich, Apr 2018. URL <https://docs.belle2.org/record/823/files/BELLE2-PTHESIS-2018-001.pdf>.
- [21] Zuzana Gruberova. Study of the τ lepton decays at the Belle II experiment. Master's thesis, Charles University of Prague, 2021. URL <https://docs.belle2.org/record/2419/files/BELLE2-MTHESIS-2021-007.pdf>.
- [22] KEK. Electrons and Positrons Collide for the first time in the SuperKEKB Accelerator, Apr. 2018. URL <https://www.kek.jp/en/newsroom/2018/04/26/0700/>.
- [23] Dong Van Thanh, Shoji Uno, Makoto Uchida, Hitoshi Ozaki, and Nanae Taniguchi. Calibration for Belle II Central Drift Chamber. *2017 IEEE Nuclear Science Symposium and Medical Imaging Conference (NSS/MIC)*, pages 1–6, 2017.
- [24] Yuki Yoshi Ohnishi et al. Accelerator design at SuperKEKB. *PTEP*, 2013: 03A011, 2013. doi: 10.1093/ptep/pts083.
- [25] Bernard Aubert et al. Search for Lepton Flavor Violating Decays $\tau^\pm \rightarrow \ell^\pm \pi^0$,

- $\ell^\pm\eta$, $\ell^\pm\eta'$. *Phys. Rev. Lett.*, 98:061803, 2007. doi: 10.1103/PhysRevLett.98.061803.
- [26] Y. Miyazaki et al. Search for lepton flavor violating tau- decays into l- eta, l- eta-prime and l- pi0. *Phys. Lett. B*, 648:341–350, 2007. doi: 10.1016/j.physletb.2007.03.027.
- [27] S. Jadach, B.F.L. Ward, and Z. Was. The precision Monte Carlo event generator for two-fermion final states in collisions. *Computer Physics Communications*, 130(3):260–325, Aug 2000. ISSN 0010-4655. doi: 10.1016/s0010-4655(00)00048-5. URL [http://dx.doi.org/10.1016/S0010-4655\(00\)00048-5](http://dx.doi.org/10.1016/S0010-4655(00)00048-5).
- [28] S. Jadach, B. F. L. Ward, and Z. Was. Coherent exclusive exponentiation for precision Monte Carlo calculations. *Physical Review D*, 63(11), May 2001. ISSN 1089-4918. doi: 10.1103/physrevd.63.113009. URL <http://dx.doi.org/10.1103/PhysRevD.63.113009>.
- [29] N. Davidson, G. Nanava, T. Przedzinski, E. Richter-Was, and Z. Was. Universal Interface of TAUOLA Technical and Physics Documentation. *Comput. Phys. Commun.*, 183:821–843, 2012. doi: 10.1016/j.cpc.2011.12.009.
- [30] T. Kuhr, C. Pulvermacher, M. Ritter, T. Hauth, and N. Braun. The Belle II Core Software. *Computing and Software for Big Science*, 3(1), Nov 2018. ISSN 2510-2044. doi: 10.1007/s41781-018-0017-9. URL <http://dx.doi.org/10.1007/s41781-018-0017-9>.
- [31] Daniel Greenwald. What have we measured? Private communication, November 2021.

- [32] Yann Coadou. Boosted Decision Trees and Applications. *EPJ Web of Conferences*, 55:02004–, 07 2013. doi: 10.1051/epjconf/20135502004.

Erklärung

Hiermit erkläre ich, die vorliegende Arbeit selbständig verfasst zu haben und keine anderen als die in der Arbeit angegebenen Quellen und Hilfsmittel benutzt zu haben.

München, den 26.11.2021